School of Physics and Astronomy
Cardiff University

PhD Thesis

Design Considerations for Weak Links Made of Boron Doped Diamond & Simulations for the Interaction Between a dc SQUID and an Integrated Micromechanical Doubly Clamped Cantilever

By

Majdi Salman

Supervisors:

Professor Oliver A Williams
Professor Sean Giblin

Cardiff, January 21, 2021

"As far as the laws of mathematics refer to reality, they are not certain; and as far as they are certain, they do not refer to reality."

Albert Einstein

Abstract

As a part of a wide and term project, where quantum micro and nano-electromechanical (MEMS NEMS) implemented in a superconducting quantum interference device (SQUID) made of boron doped diamond (BDD) to be explored, experimental and theoretical investigations, and solutions for related technical issues linked to these investigations, are presented in this thesis. Experimentally, current-voltage, $I(V)$, characteristics and the differential resistance measurements have been performed for SIS tunnel junctions, and nanobridge devices made of BDD. On the basis of analyses of these measurements, temperature dependence of the critical current, $I_c(T)$ of a nanobridge device with bridge dimensions of $L = 118$ nm, and $W = 109$ nm, shows an exponential like behaviour, $I_c(T) \propto \exp(-L\sqrt{T})$. Such dependence was attributed to the proximity effect described by Likharev's theory of SNS weak-link junctions. Furthermore, temperature dependence of $I(V)$ characteristics between 20 and 700 mK for another device with $W = 108$ nm, and $L = 78$ nm, shows resistive steps in the transition region of the $I(V)$ curves around I_c. As phase slip events may arise due to vortex kinematics and the granularity of the superconducting films, the observed steps have been attributed to vortex kinematics, and granularity of BDD films from which the device have been fabricated. On the other side, for SIS junctions, fitting for $I(V)$ characteristics measured for a typical SIS junction of a 6 nm vacuum gap, shows good agreement with the RSCJ model. An SIS junction with a wide vacuum gap of 76 nm, have been also investigated, where the measured temperature dependence of the $I(V)$ characteristics of the junction, shows two transitions, the first transition, $I_{c1}(T)$ was observed in the superconducting region, while the second one, $I_c(T)$, occurs just before the normal state. The transition $I_c(T)$ was attributed to Ambegaokar and Baratoff formula and BCS theory. Other measurements for $I(V)$, and $R(T)$ curves of superconducting strips of different strictures, have been performed. The measurements show resistive steps around transition regions of the $I(V)$ curves, and corresponding spikes have been observed in the $R(T)$ curves. Such behaviour is attributed to a collective effect that involves kinematic vortices, thermal fluctuations and/or quasiparticles diffusion (SBT model), and the granularity of BDD films from which the strips have been made. Technically, as superconducting devices are being influenced by a considerable amount of noise such as radio frequency (RF) noise, high performance RF filters were developed and fabricated. As results, the fabricated filters have shown that they are quite competitive to the earlier RF filters, efficient tools to attenuate the RF noise, and appropriate to be used for simultaneous measurements that take place in a cryogenic system where the temperatures down to few mK. In terms of theoretical aspect, simulations to quantitatively describe the interaction between a dc SQUID and an integrated doubly clamped cantilever were performed, where the unscaled dc SQUID equations coupled to the equations of motion of an integrated cantilever, have been numerically solved. In these simulations, an existing experimental configuration was selected to explore the motion of the integrated cantilever, and the voltage-displacement traces of a displacement detector were determined. Furthermore, the effect of the back-action between the SQUID and the doubly clamped cantilever have been analysed via the shift in the cantilever frequency, the line width, intensity, and shift in the position of the normal state. The simulations show how a sharp transition state drives the system into a nonlinear-like regime, and modulates the cantilever displacement amplitude, by tuning the bias current I_b, and the external flux Φ_{ext}, which set the system in different regions of $V(\Phi)$ curve.

To my mother, the best lady I know...
To my father, the best gentleman I know...

Acknowledgements

This thesis would not been performed without a great deal of support and assistance of many people. First, I would like to deeply thank my advisors prof. Sean Giblin, and prof. Oliver Williams, due to their diverse background, passion for physics, the useful discussions and opinions, and the experimental and computational facilities they provide throughout the four years of my PhD project. Next, I am grateful for Dr. Georgina Klemencic and Scott Manifold for working with me in our collaborative efforts with experimental work achieved in the dilution fridge laboratory. I would like to acknowledge Dr. Soumen Mandal for preparation the samples measured during my PhD project. Definitely, I thank Rob Tucker and Andrew Harrison from the electronic workshop for technical support. I would like to thank my colleges and officemates, Dr. Edward Riordan, Dr. Jerome Cuenca, Dr. Evan Thomas, Dr. Jess Hop-along Werrell, Dr. Laia Ginés, and Yehya Megmmi. Thanks for my friend Dr. Luqman Mustfa who I shared with him nice discussions. Thanks for my previous advisers, prof. Torsten Meier, and prof. Bernhard Keimer, who supported me to get the PhD position in Cardiff University.
Thanks for my family members, Ahmad, Isra'a, Moad, Maher, Naser, Suzan, Hussein, Manal, Isam Salman, and specially, my brother prof. Mahmoud Salman, and my sister, the brilliant mathematician, Rania Salman. Thanks to my housemates in Cardiff and various friends, specially mention, Emma, Heather, and Katie Honan and their family. Also, Tom Harrison, Andrew Nutbourne, and Tanya McGeever. Thanks to my all friends in Jordan, Germany and Australia, specially, who always keep in contact with me, Asem Afanah, Mohammad Khatib, Mosaddaq Dweikat, and Dr. Omar Zuaiter. I am also indebted to my friend Ahmad Ramadan who has taught me physics in the high school in Jordan.
I am very grateful for the National Health Service (NHS) in UK, I am grateful for all nurses and doctors, who works in the Velindre Cancer Centre in Cardiff, and supported me during my health crises over the last eighteen months of my PhD course.

Contents

1 Introduction

1.1 General overview, the long term project & motivations

1.1.1 General overview

The detection of linear and nonlinear micro and nanomechanical resonators have been a theme [1, 2, 3, 4, 5, 6, 7, 8] of great interest in recent years, as they provide an extensive knowledge for quantum phenomena associated with the macroscopic scale. In terms of technology they can be exploited as superconducting quantum circuits and superconducting quantum bits (qubits). Such systems work at extreme conditions i.e., at ultra low temperature, and in very well isolated environments, at which the systems enter the quantum state, such as nanomechanical resonators implemented in superconducting quantum interference devices (SQUIDs), that can be manipulated using an external current, magnetic flux, or/and a gate voltage, and enable the system to be controlled within the framework of a two level system (TLS). A qubit implementation allows the information science to be expressed in terms of quantum effects by considering a two level, or multilevel quantum systems that can be successfully and efficiently employed for implementations of qubits. Several physical implementations of qubits are being investigated such as electron spins in semiconductor where quantum dots are used as qubits for quantum information processing [9], nuclear magnetic resonance quantum computing (NMRQC) [10]. In terms of superconducting circuits, Josephson junctions, micro or nano-electromechanical systems (MEMS & NEMS) and quantum phase slip junctions are involved to manipulate quantum systems.

To simplify the idea behind the quantum circuits, one may consider, e.g. an inductance-capacitance (LC) circuit such that shown in Fig. 1.1(a), and looks over the possibility of bringing this circuit into a quantum region, where the system can be manipulated between the ground and the first exited states. In classical region, the circuit follows $di(t)/dt + \omega_0^2 i(t) + \frac{1}{L} i(t) = 0$, where $\omega_0^2 = \frac{1}{LC}$ in which ω is the resonance frequency of the LC circuit, with a maximum quality factor $Q_{max} = (2EC)^{1/2}$ as given in Fig. 1.1(b). To enable such circuit to enter the quantum regime, three main conditions must be satisfied: (i) the resistance of the circuit components must vanish, (ii) the circuit must be sufficiently isolated from the surrounding environment, and (iii) the thermal energy of the circuit environment must be lower than the resonance energy of its first excited state. On the basis of the first condition, the circuit must be made of a superconducting material, where the resistance becomes negligible, which results in much lower dissipation. The second condition is mainly related to the radio frequency (RF) noise that causes a quantum dissipation and decoherence. To achieve the second condition, the need for an efficient RF

filter becomes important. Ultra low temperature measurements system, such as a dilution refrigerator is required to satisfy the third condition. If these conditions are satisfied, the system can be considered as an open quantum system such that demonstrated in Fig. 1.1(c), in which the energy spectrum becomes quantized. As Josephson effect provides a highly conserved energy, Josephson junctions, as shown in Fig. 1.1(d), are used for most technological purposes, as they allow the standard representation of the Josephson voltage.

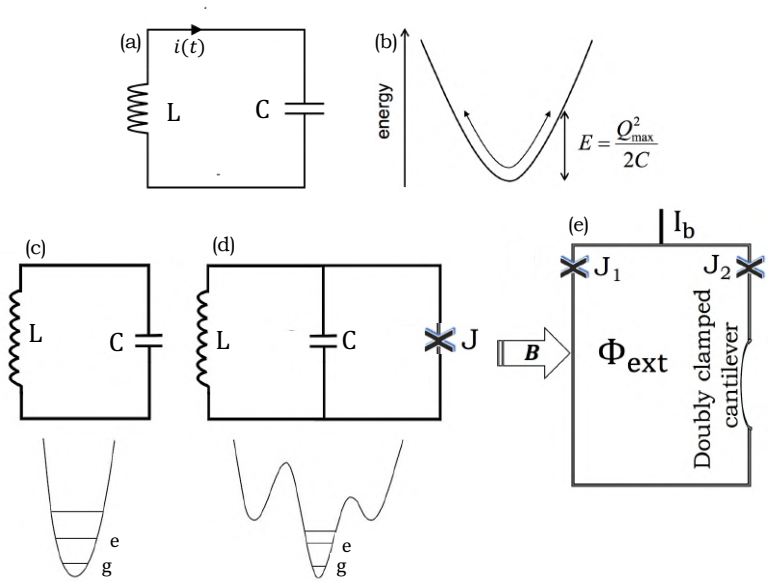

Figure 1.1: (a) and (b) Classical LC circuit with a quality factor $Q = \frac{1}{R}\sqrt{\frac{L}{C}}$, and $Q_{max} = (2EC)^{1/2}$, (b) quantum LC circuit in which three conditions to be satisfied: (i) dissipation vanishes as the resistance $R \to 0$, (ii) the energy difference between the ground state g and the first exited state e is $\omega \gg k_B T$, and (iii) the circuit is well isolated from the environment. (d) An extension of the the circuit that involves a Josephson junction J, and (e) scheme for the dc SQUID displacement detector in which the two Josephson junctions are labelled by J_1 and J_1. The cantilever displacement is out-of-plane, and the applied magnetic field, B, is in-plane.

1.1.2 The long term project & motivations

This thesis is a part of a wide and long term project that aims to study quantum micro and nano-electromechanical systems implemented in a superconducting quantum interference device (SQUID) made of boron doped diamond (BDD). To achieve such goal several processes, techniques, and experimental and theoretical investigations, are required starting from fabricating and characterising Josephson junctions (JJs), or weak links, from which a SQUID is developed, to finally, implementing a micro or nano-mechanical cantilever in the fabricated SQUID loop such that shown in Fig. 1.1(e). Etaki, *et al* [2] have demonstrated that a dc. SQUID made of Niobium (Nb), could be utilised to detect the motion of a 2 MHz mechanical resonator. However, the measured position resolution was about 133 fm. Though such value, 36 times the quantum limit, was still far from the quantum regime, subsequent experimental progress in the detection of resonators that enter the quantum ground state, has been achieved by capacitive coupling to superconducting flux

qubits [11], and quantum state control of a mechanical drum resonator in a superconducting resonant circuit has been achieved by phonon-photon coupling [12, 13]. In the framework of a quantum two level system, to detect the motion of a quantum macroscopic mechanical resonator at $T = 50$ mK, the frequency of the resonator must be higher than 1 GHz. As the fundamental frequency of a mechanical resonator is determined [15] by, $f_0 = 1.028\sqrt{\frac{E}{\rho}}\frac{d}{L^2}$, in which, E is the Young's modulus, ρ is the density, and L and d are the length and thickness of the cantilever respectively, BDD has been selected in this project as it has the highest Young's modulus [14], and that enables the system to enter a macroscopic quantum ground state at such temperatures, where a single phonon mode is occupied. Consequently, BDD will allow the quantum limit to be approached and measured in a simple integrated single circuit. Moreover, BDD based system can be easily scalable and inserted into a SQUID loop, which may create multiple entangled macroscopic quantum states through the coupling of the superconducting qubits and the area change dominated by the resonator positions.

1.1.3 Challenges

The main challenges in this project arise from two issues: (i) the short coherence length (ξ) of the BDD films, and (ii) the granular superconducting properties in the films. Since SQUID devices with typical Josephson junctions, i.e., a sinusoidal current phase relationship (CPR) can be only satisfied when a SQUID having dimensions (length L and/or width W) are shorter than ξ of the superconducting film, a challenge arises due to the fact that $\xi \approx 15$ nm [17] for the BDD films. Technically, this makes the fabrication of typical Josephson junctions, with such short weak links, extremely difficult. RF noise was another technical challenge that has been overcome through the course of this work, where a competitive RF filter has been developed and successfully fabricated. In terms of the theoretical aspect, junctions with $L > \xi$ requires to calculate CPRs such as that analytically described in [16] or those obtained [18, 19, 20] by numerically solving Ginzburg Landau equations for nanobridges with dimensions greater than ξ of the film. Due to the granular superconducting properties of BDD films, complex calculations are required in terms of Ginzburg Landau theory, where multiple and irregular boundaries conditions must be applied, and that is quite challenging. Furthermore, a full description of the SQUID-cantilever interaction requires a comprehensive model to provide information about the effects associated with this system, such as the influence of back-action of the system, and its responsivity, which must be calculated by linking the cantilever displacement to the SQUID voltage. Thus, the need for quantitative treatments of the unscaled SQUID equations coupled explicitly to the equation of motion for the implemented cantilever becomes important. Though, such treatments are complicated and challenging [25], they have been performed numerically during the course of this thesis. Moreover, during the course of this work, $I(V)$ curves and differential resistance measurements for junctions with different structures, have been performed. Measurements of, e.g, superconductor-insulator-superconductor (SIS) junction with a vacuum gap of 76 nm which is quite large relative to the coherent length of BDD films, require more theoretical work to provide a deeper understanding for the features observed in these measurements.

1.2 The thesis scope

The work presented here includes theoretical and experimental studies, simulations, and technical solutions for the issues associated with this project. Apart of the conclusions presented in Ch. 8, this thesis involves seven chapters, which are distributed as the following:

- In Ch. 2, fundamental concepts and theories of superconductivity, have been presented. The chapter also includes numerical solution of the time dependent Ginzburg Landau (TDGL) equations for a square sample. Langer, Ambegaokar, McCumber and Halperin (LAMH) theory, Skocpol, Beasley and Tinkham (SBT) model, and theoretical and earlier experimental investigations for superconducting strips, are reviewed.

- Several types of weak link devices are presented in Ch. 3, where the junctions were classified depending on the their dimensions relative to coherence length. The device properties were discussed in terms of previous theoretical studies such as Aslamazov-Larkin model, Kulik-Omelyanchuk model, dirty limit (KO-1), Kulik-Omelyanchuk model, clean limit (KO-2), and the quasiparticle theory. The operation principle of SQUIDs is based on the Josephson effect, and the flux quantization of a superconducting ring, that makes SQUIDs highly sensitive to detect extremely small magnetic field. On this basis, the operation principle of SQUIDs is quantitatively demonstrated in this chapter. As a phase slip event emerges due to highly disorder systems such as granular superconducting films that can be treated as an array of Josephson junctions (JJs), a brief overview for the later topic is presented.

- As the RF noise significantly influences the quantum state of quantum circuits, and micro and nanomechanical resonators implemented in SQUID loops, filtering out the RF noise is a critical issue. Thus, an efficient microwave powder filter was developed to considerably attenuate such noise. The functioning principles, prototype, basic materials and components, implementation, construction of the developed filter, and measurements performed on the filter are presented in Ch. 4.

- As BDD is the material from which JJs, SQUIDs, micro and nanomechanical resonators to be made, Ch. 5 goes over the properties and fabrication process of superconducting diamond, and briefly reviews the related earlier experimental and theoretical studies, as well as, the earlier junctions, SQUIDs, and mechanical resonators, made from superconducting diamond.

- Several junctions and nanobridges devices made of BDD with different structures, fabricated by a research partner in Cradiff University, and measured at ultra low temperatures, and up to the critical temperature of the superconducting diamond. $I(V)$ characterises, differential resistance, and magnetic field dependence measurements, were performed for devices with two types of weak links: (i) nanobridges of different lengths and widths, and (ii) vacuum gaps of different widths. The mea-

surements are dissuaded in terms of the theoretical criteria, presented in the earlier chapters, are discussed in Ch. 6. The last section of this chapter is specified to discuss the measurements performed to investigate the transport properties of superconducting strips.

- Simulations to quantitatively describe the interaction between a dc SQUID and an integrated doubly clamped cantilever, have been performed using the SQUID equations described by resistivity and capacitively shunted junction (RCSJ) model coupled to the equation of motion of a damped harmonic oscillator. These Simulations are presented in Ch. 7, and led to a scientific paper published in Journal of Applied Physics [1].

Bibliography

[1] Salman, Majdi, *et al.* "Quantitative analysis of the interaction between a dc SQUID and an integrated micromechanical doubly clamped cantilever." JAP **125**.22 (2019): 224503.

[2] Etaki, S., *et al.* "Motion detection of a micromechanical resonator embedded in a dc SQUID." Nature Physics **4**.10 (2008): 785-788.

[3] Blencowe, M. P., and E. Buks. "Quantum analysis of a linear dc SQUID mechanical displacement detector." Physical Review B **76**.1 (2007): 014511.

[4] Naik, A., et al. "Cooling a nanomechanical resonator with quantum back-action." Nature **443**.7108 (2006): 193-196.

[5] Kirton, Peter George, and A. D. Armour. "Nonlinear dynamics of a driven nanomechanical single-electron transistor." Physical Review B **87**.15 (2013): 155407.

[6] Cohen, Guy Z., and Massimiliano Di Ventra. "Reading, writing, and squeezing the entangled states of two nanomechanical resonators coupled to a SQUID." Physical Review B **87**.1 (2013) 014513.

[7] Ella, Lior, *et al.* "Tunable strong nonlinearity of a micromechanical beam embedded in a dc-superconducting quantum interference device." Journal of Applied Physics **117**.1 (2015): 014309.

[8] Pugnetti, Stefano, *et al.* "Dynamics of a SQUID ratchet coupled to a nanomechanical resonator." Physical Review B **79**.17 (2009): 174516.

[9] Struck, Philipp R., and Guido Burkard. "Spin Quantum Computing." (2015): 1-27.

[10] Chuang, Isaac L., *et al.* "SBulk quantum computation with nuclear magnetic resonance: theory and experiment." Proceedings of the Royal Society of London. Series A: Mathematical, Physical and Engineering Sciences **454**.1969 (1998): 447-467.

[11] O'Connell, Aaron D., *et al.* "Quantum ground state and single-phonon control of a mechanical resonator." Nature **464**.7289 (2010): 697-703.

[12] Teufel, John D., *et al.* "Circuit cavity electromechanics in the strong-coupling regime." Nature **471**.7337 (2011): 204-208.

[13] Rocheleau, T., *et al.* "Preparation and detection of a mechanical resonator near the ground state of motion." Nature **463**.7277 (2010): 72-75.

[14] K. E. Spear & J. P. Dismukes. Synthetic diamond: emerging CVD science and technology. John Wiley & Sons, **25**, (1994).

[15] Imboden, Matthias, and Pritiraj Mohanty. "Dissipation in nanoelectromechanical systems." Physics Reports **534**.3 (2014): 89-146.

[16] Golubov, Alexandre Avraamovitch, M. Yu Kupriyanov, and E. Il'Ichev. "The current-phase relation in Josephson junctions." Reviews of modern physics **76**.2 (2004): 411.

[17] Bustarret, Etienne, *et al.* "Dependence of the superconducting transition temperature on the doping level in single-crystalline diamond films." Physical review letters **93**.23 (2004): 237005.

[18] Granata, Carmine, and Antonio Vettoliere. "Nano superconducting quantum interference device: A powerful tool for nanoscale investigations." Physics Reports 614 (2016): 1-69.

[19] Hasselbach, K., D. Mailly, and J. R. Kirtley. "Micro-superconducting quantum interference device characteristics." Journal of applied physics **91**.7 (2002): 4432-4437.

[20] Granata, C., *et al.* "Noise theory of dc nano-SQUIDs based on Dayem nanobridges." Physical Review B **84**.22 (2011): 224516.

[21] The supplementary Information: S. Etaki, F. Konschelle, Ya. M. Blanter, H. Yamaguchi, and H. S. J. van der Zant, Nat. Commun. **4** 1803 (2013).

2 Fundamental Theories of Superconductivity

2.1 Superconductivity

2.1.1 Zero-resistivity and perfect diamagnetism

In 1911, three years after liquefying Helium, superconductivity was discovered by Heike Kamerlingh Onnes where the resistance of a solid mercury wire immersed in liquid Helium suddenly vanished at 4.2 K. Onnes has called [1] this new phenomenon the "superconductive state". Besides zero-resistivity, a new and separate physical property for superconductors was discovered in 1933 by W. Meissner and R. Ochsenfeld. In this discovery [3] it was shown that a magnetic field is expelled from a superconductor upon cooling to below the superconducting transition, T_c. The second phenomenon becomes known as the Meissner-Ochsenfeld effect. As the total magnetic field inside the superconductor must be zero upon applying an external field, an internal field arises to leave the total field zero. This is satisfied only if the internal field is opposite in the direction and equal in the magnitude to the external field. Obviously the emergence of the internal magnetic field requires screening currents flowing around the edges of the superconductor. Maxwell's equations can be used to describe [4, 5] the screening currents $\mathbf{j}_{\text{int}}$ in a magnetic medium with $\mathbf{j}_{\text{tot}} = \mathbf{j}_{\text{ext}} + \mathbf{j}_{\text{int}}$, where $\mathbf{j}_{\text{ext}}$ is the external currents related to the external field $\mathbf{H}$ as $\mathbf{j}_{\text{ext}} = \nabla \times \mathbf{H}$, and $\mathbf{j}_{\text{tot}}$ is the total currents that defined in terms of the total field $\mathbf{B}$ by $\mathbf{j}_{\text{tot}} = \nabla \times \mathbf{B}$. Inside the superconductor a magnetization $\mathbf{M}$ emerges due to $\mathbf{j}_{\text{int}}$ and the magnetization per unit volume reads: $\mathbf{j}_{\text{int}} = \nabla \times \mathbf{M}$. Now the total field $\mathbf{B}$ is related to the external field $\mathbf{H}$ and magnetization $\mathbf{M}$ by:

$$\mathbf{B} = \mu_0(\mathbf{H} + \mathbf{M}), \tag{2.1}$$

where μ_0 is the permeability of free space. Since $\nabla \cdot \mathbf{B} = 0$, and $\nabla \times \mathbf{H} = \mathbf{j}_{\text{ext}}$, two boundary conditions are applied: (i) the components of $\mathbf{B}$ perpendicular to the surface must remain constant, i.e, $\Delta\mathbf{B}_{\perp} = 0$, and (ii) the components of $\mathbf{B}$ parallel to the surface remain constant, i.e, $\Delta\mathbf{H}_{\parallel} = 0$. The Meissner-Ochsenfeld condition requires the total field $\mathbf{B} = 0$, thus Eq. 2.1 leads to $\mathbf{H} = -\mathbf{M}$. As the magnetic susceptibility χ is given by $\left.\frac{dM}{dH}\right|_{H=0}$, the susceptibility χ for a superconductor reads

$$\chi = -1, \tag{2.2}$$

Such value for χ implies that the external field in superconductors is completely screened out, and this is usually known as perfect diamagnetism.

2.1.2 Type I and type II superconductivity

So far, the susceptibility χ is defined in presence of a weak external field $\mathbf{H}$. However, in presence of a strong external field one of two phase transitions occur depending on the material from which the superconductor is made. Accordingly, superconductors are classified into the two classes shown in Fig. 2.1. In type I, as the external field remains below critical value H_c, the B field remains zero inside the superconductor, and the magnetization subjects to $\mathbf{M} = -\mathbf{H}$. However, the superconducting state is destroyed when $H > H_c$. Two different critical fields present in a type II superconductor: the lower critical field H_{c1}, and the upper critical field H_{c2}. Here, when $H < H_{c1}$, the magnetization subjects to $\mathbf{M} = -\mathbf{H}$, and when $H_{c1} < H < H_{c2}$, the magnetic flux density gradually increases by increasing H, until finally $H = H_{c2}$ at which the superconductivity is destroyed and the magnetization becomes zero.

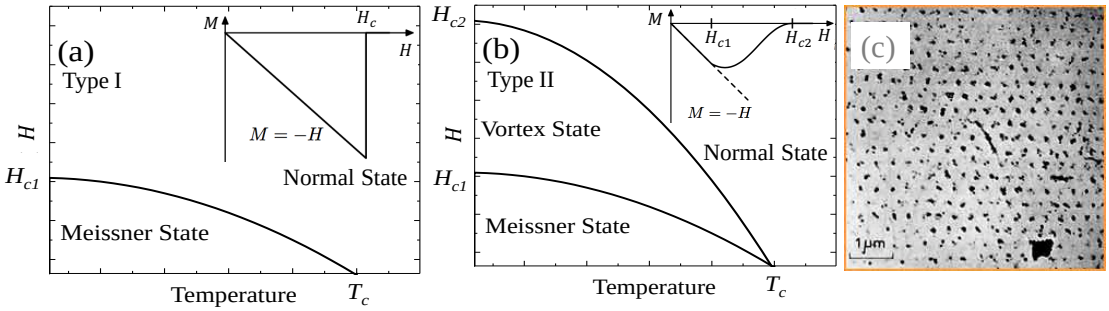

Figure 2.1: The two superconductor classes in which, (a) and the inset(a) shows the H-T and M-H phase diagrams of type I superconductors respectively, while (b) and inset(b) are the diagrams of type II superconductors. (c) The first experimental evidence [6] of Abrikosov vortex lattice as observed on the surface of lead rod at $T = 1.1$ K.

Abrikosov predicted [7] the phase diagram of type II superconductors given in Fig. 2.1 in terms of H_{c1} and H_{c2}. Abrikosov showed that the magnetic field can penetrate the superconductor surface in the form of vortices each of which consists of a region where a supercurrent circulates around a small central core of a normal metal. As the external magnetic field increases, the number of vortices N_v per unit area A increases until the vortices combine together at H point at which the sample is completely turned from a superconducting phase to normal metal phase. Quantitatively, N_v is related to the screening field B according to the following $\frac{N_v}{A} = \frac{2eB}{h}$, where e the electron charge, and h is the Planck's constant.

2.1.3 The London equations

The Meissner-Ochsenfeld effect could be explained by a theory developed [8] by F. London and H. London. In this theory which has been originally suggested for superfluid ^{4}He, the conduction electrons can have two classes: (i) the normal electrons with a finite resistivity, and (ii) the superconducting electrons that can move without dissipation. The number density of superconducting carriers is denoted by n_s, and two London equations expressed

in terms of the electric and magnetic fields $\mathbf{E}$ and $\mathbf{B}$ within the superconductor:

$$\frac{\partial \mathbf{j}_s}{\partial t} = \frac{n_s e^2}{m_e}\mathbf{E}, \tag{2.3}$$

$$\nabla \times \mathbf{j}_s = -\frac{n_s e^2}{m_e}\mathbf{B}, \tag{2.4}$$

where $\mathbf{j}_s$ is the superconducting current density, and m_e is the rest mass of electron. By applying Ampere's law in which $\nabla \times \mathbf{B} = -\mu_0 \mathbf{j}_s$, the second London's equation can be written as $\nabla^2 \mathbf{B} = \frac{1}{\lambda^2}\mathbf{B}$. Here, $\lambda = (\frac{m_e}{\mu_0 n_s e^2})^{\frac{1}{2}}$ which is the London penetration depth that characterizes the distance at which a magnetic field penetrates a superconductor is equal to $\exp(-1)$ times of the magnetic field at the surface. The magnetic field that penetrates a superconductor at depth x from the surface is $B_z(x) = B_0 \exp(-\frac{x}{\lambda})$, where B_0 is the magnetic field at the superconductor surface and z denotes the field direction relative to the boundary.

2.2 Ginzburg–Landau theory

The Ginzburg–Landau theory has been developed on the basis of the Landau's theory of second order phase transitions [9]. Here, the Meissner, vortex, and normal states are quantitatively described in terms of the phase φ as $\psi(\mathbf{r}) = (i\varphi)$, that can be obtained by solving the Ginzburg-Landau equations, from which an order parameter Δ is defined by $\Delta = |\psi(\mathbf{r})|^2$. The order parameter is zero when $T \geq T_c$, one for a pure superconducting state, and it has a nonezero value (below one) for the vortex state.

2.2.1 Thermodynamics of superconducting phase

A transition from a superconducting state to normal state can be described using a Gibbs function in which free energy per unit volume $F(T)$ is defined using a Taylor series for the order parameter $\Delta = |\psi(\mathbf{r})|^2$ around T_c

$$F(T) = F_n + \alpha(T)|\psi(\mathbf{r})|^2 + \frac{1}{2}\beta|\psi(\mathbf{r})|^4 + \gamma|\psi(\mathbf{r})|^6, \tag{2.5}$$

where F_n is the free energy in the normal phase, $\alpha(T)$, $\beta(T)$, and γ are in the initial argument treated as phenomenological parameters. Since the energy is more appropriate to be in the normal state when $T > T_c$, the Gibbs function must have a minima at $\psi = 0$, thus

$$\left.\frac{\partial F}{\partial \psi}\right|_{\psi=0} = 0. \tag{2.6}$$

When $T \to T_c$, the last term in above equation is negligible, and the Gibbs function becomes

$$F(T) = F_n + \alpha(T)|\psi(\mathbf{r})|^2 + \frac{1}{2}\beta|\psi(\mathbf{r})|^4, \tag{2.7}$$

and the combination of the last two equations gives $\alpha\psi + \beta\psi^3 = 0$ which results in two solutions: $\psi_0 = 0$ which accounts for $T > T_c$ region, or $\psi_\infty = \pm\sqrt{\frac{\alpha}{\beta}}$ for $T < T_c$ region. Since F must not decrease for large ψ values, β must be always positive, while α must be positive for $T > T_c$, and negative for $T < T_c$. Thus an expression for α can be written in terms of temperature as: $\alpha = \alpha_0(T - T_c)$. The free energy dependence on ψ is illustrated in Fig. 2.2.

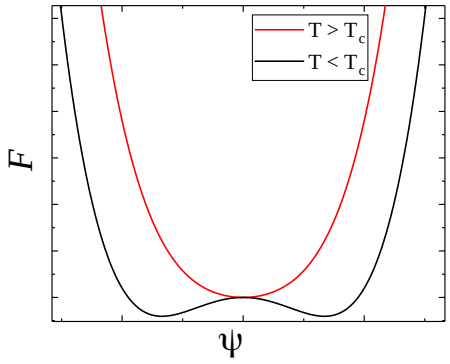

Figure 2.2: The free energy for the normal (red) and superconducting (black) state.

In presence of an external of magnetic field $\mathbf{B}_{ext}$, the free energy reads

$$F(T) = F_n + \frac{1}{2m}\left|\left(\frac{\hbar}{i}\nabla - q\mathbf{A}\right)\psi\right|^2 - \alpha|\psi|^2 + \frac{\beta}{2}|\psi|^4 + \frac{1}{\mu_0}|\mathbf{B}_{ext} - \mathbf{B}_i|^2, \tag{2.8}$$

where $\mathbf{A}$ is the vector potential, $\mathbf{B}_i = \nabla \times \mathbf{A}$ is the magnetic filed inside the superconductor, and $q = 2e$ is the cooper pair charge. The last term in Eq. 2.8 is the energy density $u_B = \frac{1}{\mu_0}|\mathbf{B}_{ext} - \mathbf{B}_i|^2$.

2.2.2 Time independent Ginzburg–Landau equations

The equilibrium states are determined by minimizing the free energy with respect to variations in the order parameter and the vector potential. Obtaining the minima of the free energy results in the time independent Ginzburg–Landau (TIGL) equations. The derivation of TIGL equations can be found in [10, 11]. The final form of the TIGL equations leads to the expressions given by Eqs. 2.9 and 2.10

$$\frac{1}{2m}\left(\frac{\hbar}{i}\nabla - q\mathbf{A}\right)^2\psi - \alpha\psi + \frac{\beta}{2}|\psi|^2\psi = 0, \tag{2.9}$$

and the supercurrent $\mathbf{J}_s$ is given by

$$\mathbf{J}_s = \frac{q\hbar}{2mi}(\psi^*\nabla\psi - \psi\nabla\psi^*) - \frac{q^2}{m}\psi^*\psi\mathbf{A} + \frac{1}{\mu_0}\nabla \times \mathbf{B}_{ext}. \tag{2.10}$$

If the applied magnetic field is uniform, the current does not flow out of the superconducting surface, or in other words, $\nabla \times \mathbf{B}_{ext} = 0$. This statement leads to the first boundary condition:

$$\left(\frac{\hbar}{i}\nabla\psi - q\mathbf{A}\psi\right) \cdot \mathbf{n} = 0. \tag{2.11}$$

As the magnetic field must be continuous, another boundary condition is given by

$$\mathbf{B}_{ext} = \mathbf{B}_i \tag{2.12}$$

The second London equation given earlier in Eq. 2.4 can be obtained from the second time independent Ginzburg–Landau equation by considering the following: in the Meissner phase the vector potential $\mathbf{A}$ can be neglected. This leads to the earlier result for ψ_∞ that can be obtained by $\frac{\partial F}{\partial \psi} = 0$ in Eq. 2.8 with $|\psi_\infty|^2 = \frac{\alpha}{\partial \beta}$. The expression for ψ_∞ is then inserted into Eq. 2.10 to get the supercurrent $\mathbf{J}_s = -\frac{q^2\alpha}{m\beta}\mathbf{A}$ which leads to the second London equation by taking the curl of both sides. This finally leads again to the London penetration depth λ obtained in Sec. 2.1.3. Coherence length ξ is another characteristic parameter for superconductors that can be obtained from the TIGL equations by normalizing Eq. 2.9 with $\psi \to \frac{\psi}{\psi_\infty}$. This leads to

$$\frac{\hbar^2}{2m\alpha}\left(\frac{1}{i}\nabla - \frac{q}{\hbar}\mathbf{A}\right)^2\psi - \psi + |\psi|^2\psi = 0. \tag{2.13}$$

In the Meissner phase $\mathbf{A}$ is negligible. Thus Eq. 2.13 becomes

$$-\frac{\hbar^2}{2m\alpha}\nabla^2\psi(\mathbf{r}) - \psi(\mathbf{r}) + |\psi(\mathbf{r})|^2\psi = 0. \tag{2.14}$$

By assuming a model with an interface between a normal metal and superconductor, in which the interface lies in the yz plane with $x < 0$ is the normal metal region and $x > 0$ is the superconductor region. In such model for all $x > 0$, Eq. 2.14 has a real solution

$$\psi(x) = \tanh\left(\frac{x}{\sqrt{2}\xi_{GL}}\right), \tag{2.15}$$

where ξ_{GL} is Ginzburg–Landau coherence length and is given by:

$$\xi_{GL} = \sqrt{\frac{\hbar^2}{2m|\alpha(T)|}}. \tag{2.16}$$

It should be noted here that the Ginzburg-Landau coherence is temperture dependent, where

$$\xi_{GL} = \xi_0\left|1 - \frac{T}{T_c}\right|^{-\frac{1}{2}}. \tag{2.17}$$

In Fig. 2.3, $\psi(x)$ is plotted versus $\frac{x}{\xi_{GL}}$ as obtained from Eq. 2.15. It's obvious from the figure that a superconductors with shorter coherence lengths results in a higher order parameter $|\psi|^2$, which also leads to approaching to Meissner phase at which $|\psi|^2 = 1$.

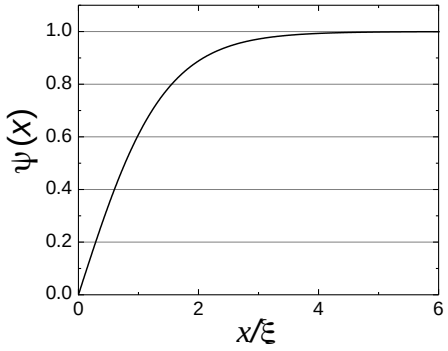

Figure 2.3: Order parameter of a superconductor near a surface for a normal metal-superconductor interface lying in yz plane.

Critical magnetic fields B_c, B_{c1} and B_{c2} discussed in Sec. 2.1.2 and shown in Fig. 2.1 in terms of magnetic field strength H, can be also obtained from the TIGL equations. Here, I only show the final results, and the full details can be found in Ref [7, 12]. For type I superconductor, the critical magnetic fields reads

$$B_c = \left|\mu_0 \frac{\alpha^2}{\beta}\right|^{\frac{1}{2}}, \tag{2.18}$$

and for type II superconductor the lower critical field is [13]

$$B_{c1} = \frac{1}{\kappa}\ln(\kappa + 0.008)B_c, \tag{2.19}$$

and the upper field reads

$$B_{c2} = \sqrt{2}\kappa B_c, \tag{2.20}$$

where κ is called the Ginzburg–Landau parameter that defined by

$$\kappa = \frac{m}{\hbar q}\sqrt{\frac{2\beta}{\mu_0}}. \tag{2.21}$$

The Ginzburg–Landau parameter κ is used to classify superconductors as: (i) for type I superconductors $\kappa < \frac{1}{\sqrt{2}}$, and (ii) for type II $\kappa > \frac{1}{\sqrt{2}}$. Finally, in terms of coherence length and penetration depth, the Ginzburg–Landau parameter can be written as

$$\kappa = \frac{\lambda_L}{\xi_{GL}}. \tag{2.22}$$

2.2.3 Normalized time dependent Ginzburg Landau (TDGL) equations

So far, several superconducting parameters have been defined by time independent Ginzburg Landau equations. This subsection is an extension for the Ginzburg Landau theory where more details about superconductor vortices are simulated by solving TDGL equations numerically. Here, I start directly with the normalized [24] TDGL equations which are coupled with Maxwell equations as

$$\frac{\partial \psi}{\partial \tau} = -\frac{1}{\eta}\left[(-i\nabla - \mathbf{A})^2\psi + (1-\tilde{T})(|\psi|^2 - 1)\psi\right] + \tilde{F}, \tag{2.23}$$

$$\frac{\partial \mathbf{A}}{\partial \tau} = (1-\tilde{T})\Re[\bar{\psi}(-i\nabla - \mathbf{A})\psi] - \kappa^2 \nabla \times \nabla \times \mathbf{A}, \tag{2.24}$$

with

$$\mathbf{J}_n = -\frac{\partial \mathbf{A}}{\partial \tau}, \tag{2.25}$$

and

$$\mathbf{J}_n = (1-\tilde{T})\Re[\bar{\psi}(-i\nabla - \mathbf{A})\psi], \tag{2.26}$$

In these equations the spatial dimensions (x, y) are scaled in units of ξ_0, time τ in unit of $t_0 = \frac{\pi\hbar}{96 k_B T_c}$, temperature in units of T_c, and the vector potential $\mathbf{A}$ in units of $H_{c2}\xi_0$. Here, k_B is the Boltzmann constant, η in Eq. 2.23 is a positive constant (a ratio of characteristic times for ψ and $\mathbf{A}$, and $\Re$ in Eq. 2.24 refers to the real part. Two boundary conditions for ψ and $\mathbf{A}$ are imposed: the applied field H_{ext} in the z direction, can be time-dependent and spatially uniform. Thus the continuity of the field implies

$$B_z = \mathbf{e}_z \cdot \nabla \times \mathbf{A} = H_{ext}. \tag{2.27}$$

This condition is another form for the boundary condition given in Eq. 2.12. The second boundary condition is imposed for ψ where supercurrent density perpendicular to the boundary must be zero. This condition can be expressed as

$$\mathbf{n} \cdot (-i\nabla - \mathbf{A}) = 0, \tag{2.28}$$

As the total current across the superconductor vacuum interface is zero, the condition given in Eq. 2.27 implies the normal current $\mathbf{J}_n$ is also zero. This can be proved by combining Eqs. 2.24 - 2.26 which lead to

$$\mathbf{J}_n + \mathbf{J}_s = \kappa^2 \nabla \times \nabla \times \mathbf{A}. \tag{2.29}$$

The normal $\mathbf{n}$ have components $(n_x, n_y, 0)$, thus

$$\mathbf{n} \cdot (\mathbf{J}_n + \mathbf{J}_s) = \kappa^2 \left(\frac{\partial}{\partial x} - \frac{\partial}{\partial y} \right) B_z. \tag{2.30}$$

Since $\left(\frac{\partial}{\partial x} - \frac{\partial}{\partial y} \right)$ is a tangential derivative, the applied field H_{ext} is uniform, the right-hand side of Eq. 2.30 vanishes implying that the total current across the boundary is zero. Finally, the magnetization M_z is defined [15] as

$$M_z(\tau) = \frac{\int \Big(B_z(x, y, \tau) - H_{ext} \Big) dxdy}{4\pi \int dxdy} \tag{2.31}$$

2.2.4 Numerical treatment of TDGL equations

The TDGL equations can be numerically solved using both finite element [15, 16] and finite difference [17, 18, 19, 20, 21] methods. However, a specific finite difference method that is known [24, 22, 23] as ψU-method is very common procedure in the numerical treatment of TDGL equations. In this method the vector $\mathbf{U}$ is introduced in terms of two auxiliary fields ($\mathcal{U}^x$,$\mathcal{U}^y$) which are given by

$$\mathcal{U}^x(x, y, \tau) = \exp\left(-i \int_{x_0}^{x} A_x(\xi, y, \tau) d\xi \right), \tag{2.32}$$

$$\mathcal{U}^y(x, y, \tau) = \exp\left(-i \int_{y_0}^{y} A_y(x, \eta, \tau) d\eta \right), \tag{2.33}$$

where (x_0, y_0) is an arbitrary point, and the discrete analogs of $\mathcal{U}^x$ and $\mathcal{U}^y$ can be defined [24] at the nodes as

$$\mathcal{U}^x_{i,j} = \prod_{k=1}^{i-1} U^x_{i,j}, \qquad \mathcal{U}^y_{i,j} = \prod_{k=1}^{j-1} U^x_{i,j}. \tag{2.34}$$

This leads to:

$$U^x_{i,j} \equiv \bar{\mathcal{U}}^x_{i,j} \mathcal{U}^x_{i+1,j} = \exp\left(-i \int_{x_i}^{x_{i+1}} A_{x,i,j} dx \right) = \exp(-iA_{x,i,j}\Delta x), \tag{2.35}$$

and

$$U^y_{i,j} \equiv \bar{\mathcal{U}}^y_{i,j} \mathcal{U}^y_{i,j+1} = \exp\left(-i \int_{y_i}^{y_{i+1}} A_{y,i,j} dy \right) = \exp(-iA_{y,i,j}\Delta y), \tag{2.36}$$

where $A_{x,i,j} = A_x(x_i + \frac{\Delta x}{2}, y_j)$, and $A_{y,i,j} = A_y(x_i, y_i + \frac{\Delta y}{2})$. Since $\frac{\partial \mathcal{U}^x}{\partial x} = -i\mathcal{U}_x A_x$, the term $(-\nabla - \mathbf{A})^2$ reads

$$(-\nabla - \mathbf{A})^2\psi = -\bar{\mathcal{U}}^x \frac{\partial^2}{\partial x^2}(\mathcal{U}^x\psi) - \bar{\mathcal{U}}^y \frac{\partial^2}{\partial y^2}(\mathcal{U}^y\psi). \tag{2.37}$$

By combining Eqs. 2.36 and 2.37, and using the second order of the FEM scheme, the second order approximation at (x_i, y_j) reads

$$\begin{aligned}(-\nabla - \mathbf{A})^2\psi\Big|_{(x_i,y_j)} = &-\frac{U^x_{i,j}\psi_{i+1,j} - 2\psi_{i,j} + \bar{U}^x_{i-1,j}\psi_{i-1,j}}{a_x^x} \\ &- \frac{U^y_{i,j}\psi_{i,j+1} - 2\psi_{i,j} + \bar{U}^y_{i-1,j}\psi_{i,j-1}}{a_y^2} + \mathcal{O}(a_x^2 + a_y^2).\end{aligned} \tag{2.38}$$

Another term in Eq. 2. 2.23 is $(|\psi|^2 - 1)\psi$, which can be approximated as

$$(|\psi|^2 - 1)\psi = (\bar{\psi}_{i,j}\psi_{i,j} - 1)\psi_{i,j}. \tag{2.39}$$

The term $\Re[\bar{\psi}(-i\frac{\partial}{\partial x} - \mathbf{A}_x)\psi]$ can be discretized using the identity, $(-i\frac{\partial}{\partial x} - A_x)\psi = i\bar{\mathcal{U}}^x\frac{\partial}{\partial x}(\mathcal{U}\psi)$ which follows

$$\begin{aligned}&\Re\left[\bar{\psi}(-i\frac{\partial}{\partial x} - A_x)\psi\right]\Big|_{x_i+\frac{a_x}{2},y_j} \\ &= \Im\left[\frac{\bar{\mathcal{U}}^x_{i,j}\bar{\psi}_{i,j} + \bar{\mathcal{U}}^x_{i+1,j}\bar{\psi}_{i+1,j}}{2} \cdot \frac{\mathcal{U}^x_{i+1,j}\psi_{i+1,j} - \mathcal{U}^x_{i,j}\psi_{i,j}}{a_x^2}\right] + \mathcal{O}(a_x^2) \\ &\frac{1}{a_x}\Im(\bar{\psi}_{i,j}\bar{\mathcal{U}}^x_{i,j}\psi_{i+1,j}\mathcal{U}^x_{i+1,j}) + \mathcal{O}(a_x^2) \\ &= \frac{1}{a_x}\Im(\bar{\psi}_{i,j}U^x_{i,j}\psi_{i+1,j}) + \mathcal{O}(a_x^2),\end{aligned} \tag{2.40}$$

where $\Im$ refers to the imaginary part. Analogously, the y component the term reads

$$\Re\left[\bar{\psi}(-i\frac{\partial}{\partial y} - A_y)\psi\right]\Big|_{x_i,y_j+\frac{a_y}{2}} = \frac{1}{a_y}\Im(\bar{\psi}_{i,j}U^y_{i,j}\psi_{i,j+1}) + \mathcal{O}(a_y^2). \tag{2.41}$$

To discretize the term $\nabla \times \nabla \times \mathbf{A}(= \nabla \times \mathbf{B})$ given in Eq. 2.24, the following auxiliary variable is introduced

$$L_{i,j} = U^x_{i,j}U^y_{i+1,j}\bar{U}^x_{i,j+1}\bar{U}^y_{i,j}, \tag{2.42}$$

with

$$L_{i,j} = \exp\left(-ia_xa_yB_z(x_i + \frac{a_x}{2}, y_j + \frac{a_y}{2}\right)\left(1 + \mathcal{O}(a_x^2 + a_y^2)\right). \tag{2.43}$$

Here, $\mathbf{B} = (0, 0, B_z)$ with which $\nabla \times \mathbf{B} = \left(\frac{\partial B_z}{\partial y}, \frac{\partial B_z}{\partial x}, 0\right)$, and the components $\left(\frac{\partial B_z}{\partial y}, \frac{\partial B_z}{\partial x}\right)$ follow

$$\frac{\partial B_z}{\partial y}\left(x_i + \frac{a_x}{2}, y_j\right) = \frac{i}{a_x a_y^2}\left(\bar{L}_{i,j-1} L_{i,j} - 1\right) + \mathcal{O}(a_x^2 + a_y^2), \tag{2.44}$$

$$\frac{\partial B_z}{\partial x}\left(x_i, y_j + \frac{a_y}{2}\right) = -\frac{i}{a_x^2 a_y}\left(\bar{L}_{i,j} L_{i-1,j} - 1\right) + \mathcal{O}(a_x^2 + a_y^2), \tag{2.45}$$

The last term in Eq. 2.24 is $\frac{\partial \mathbf{A}}{\partial \tau}$ which can be discretized from

$$\begin{aligned}
&\frac{\partial}{\partial \tau}\left(\bar{\mathcal{U}}^x(x, y, \tau)\mathcal{U}^x(x + \delta, y, \tau)\right) \\
&= -i\bar{\mathcal{U}}^x(x, y, \tau)\mathcal{U}^x(x + \delta, y, \tau)\int_x^{x+\delta} \frac{\partial}{\partial \tau} A_x(\xi, y, \tau) d\xi \\
&= i\delta\bar{\mathcal{U}}^x(x, y, \tau)\mathcal{U}^x(x + \delta, y, \tau)\frac{\partial}{\partial \tau} A_x\left(x + \frac{\delta}{2}, y, \tau\right) + \mathcal{O}(\delta^2).
\end{aligned} \tag{2.46}$$

Thus,

$$\frac{\partial}{\partial \tau} A_x\left(x_i + \frac{a_x}{2}, y_j, \tau\right) = \frac{i}{a_x}\bar{U}^x_{i,j}\frac{\partial}{\partial \tau} U^x_{i,j} + \mathcal{O}(a_x^2). \tag{2.47}$$

Similarly,

$$\frac{\partial}{\partial \tau} A_y\left(x_i, y_j + \frac{a_y}{2}, \tau\right) = \frac{i}{a_y}\bar{U}^y_{i,j}\frac{\partial}{\partial \tau} U^y_{i,j} + \mathcal{O}(a_y^2). \tag{2.48}$$

By substituting Eqs. 2.37 -2.48 in the TDGL equations given by Eqs. 2.23 and 2.24, the discretized TDGL equations follow

$$\begin{aligned}
\frac{\partial \psi_{i,j}}{\partial \tau} &= \frac{U^x_{i,j}\psi_{i+1,j} - 2\psi_{i,j} + \bar{U}^x_{i-1,j}\psi_{i-1,j}}{\eta a_x^2} \\
&+ \frac{U^y_{i,j}\psi_{i,j+1} - 2\psi_{i,j} + \bar{U}^y_{i,j-1}\psi_{i,j-1}}{\eta a_y^2} + \frac{1 - \tilde{T}}{\eta}(\bar{\psi}_{i,j}\psi_{i,j} - 1)\psi_{i,j} + \tilde{F}_{i,j},
\end{aligned} \tag{2.49}$$

$$\frac{\partial^x_{i,j}}{\partial \tau} = -i(1 - \tilde{T})U^x_{i,j}\Im\left[\bar{\psi}_{i,j}U^x_{i,j}\psi_{i+1,j}\right] - \frac{\kappa^2}{a_y^2}U^x_{i,j}(\bar{L}_{i,j-1}L_{i,j} - 1) \tag{2.50}$$

$$\frac{\partial^y_{i,j}}{\partial \tau} = -i(1 - \tilde{T})U^y_{i,j}\Im\left[\bar{\psi}_{i,j}U^y_{i,j}\psi_{i,j+1}\right] - \frac{\kappa^2}{a_x^2}U^y_{i,j}(\bar{L}_{i-1,j}L_{i,j} - 1) \tag{2.51}$$

To discretize the time variable with time step $d\tau$, Euler scheme can be used

$$\frac{\partial \psi_{i,j}}{\partial \tau} = \frac{\psi_{i,j}(\tau + d\tau) - \psi_{i,j}(\tau)}{d\tau}. \tag{2.52}$$

Similarly, the terms $U^x_{i,j}$, and $U^y_{i,j}$ can be discretized. The random force $\tilde{F}_{i,j}$ can be treated [24] as a vortex variable.

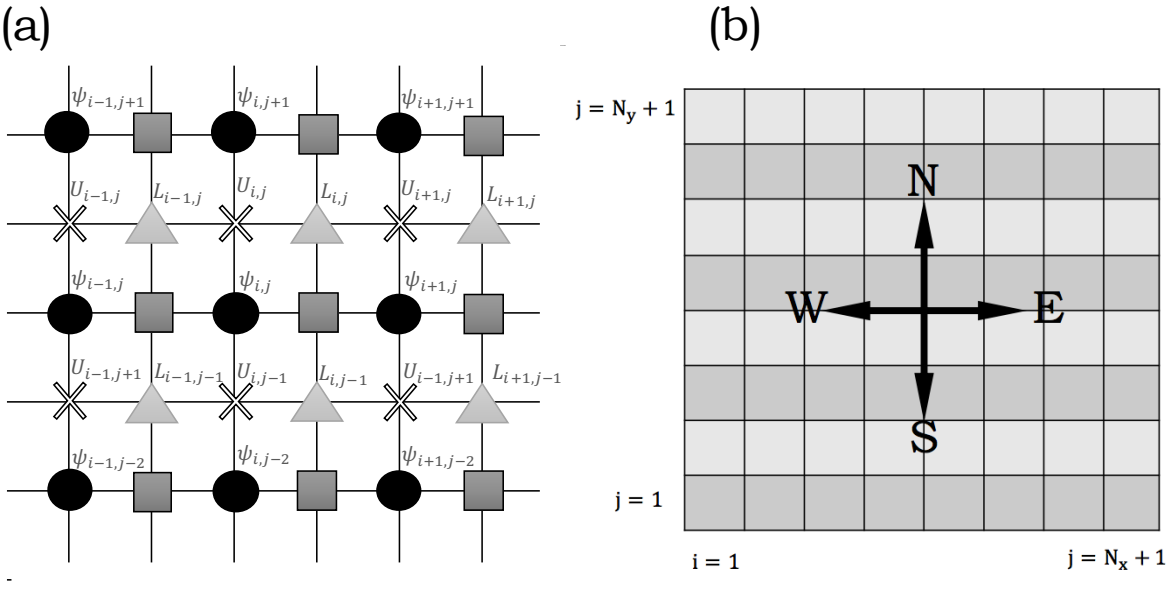

Figure 2.4: (a) The computational cells used for the discretization of the TDGL equations, and (b) scheme of the computational mesh with the boundaries of the square sample used in calculations.

For the aligned boundary in y-axis, the zero-current condition $(-\frac{\partial}{\partial x} - A_x)\psi = 0$ that equivalent to $-i\bar{\mathcal{U}}^x \frac{\partial}{\partial x}(\mathcal{U}^x\psi) = 0$ can be written using first order approximation as:

$$\psi_{1,j} = U^x_{1,j}\psi_{2,j}, \qquad \psi_{N_x+1,j} = \bar{U}^x_{N_x,j}\psi_{N_x,j} \tag{2.53}$$

$$\psi_{i,1} = U^y_{i,1}\psi_{j,2}, \qquad \psi_{i,N_y+1} = \bar{U}^y_{i,N_y}\psi_{i,N_y} \tag{2.54}$$

The west and east boundaries shown in Fig. 2.4(b) are vertically aligned at $i = 1$ and $i = N_x + 1$ respectively, while the south and north boundaries are horizontally aligned at $j = 1$ and $j = N_y + 1$ respectively. To update the link variables values on the boundary, it should be noted that as the total circulation of the vector potential around propagates inside the computational domain, the only product of the two link variables can be numerically obtained for the cells with two edges on the boundary [24]. This issue leaves an unknown link variable for each cell on the boundary, with the other three link variables defined in Eqs. 2.50 and 2.51. However, the unknown link variable can be obtained from

$$L_{i,j} = U^x_{i,j}U^y_{i+1,j}\bar{U}^x_{i,j+1}\bar{U}^y_{i,j} = \exp(-ia_xa_yH_{ext}). \tag{2.55}$$

2.2.5 Example results

A result for the numerical calculations of TDGL equations is finally obtained by considering a square sample with dimensions $64\xi_0 \times 64\xi_0$. The calculations have been performed using Fortran in which the following parameters have been implemented in the code: the mesh spacing along x and y axes are $a_x = a_y = 0.5$, scaled temperature $T = 0.5$, with $\kappa = 2$ and $\eta = 1$. The time step $\Delta\tau$ must satisfy the Euler method so that $\Delta\tau \leq \left(\frac{h^2\eta}{4}, \frac{h^2}{4\kappa^2}\right)$ with $h^2 = \frac{2}{\frac{1}{a_x^2}+\frac{1}{a_x^2}}$. At $\tau = 0$, a perfect Meissner state is initialized with $\psi|_{\tau=0} = 0$, and $\mathbf{A}|_{\tau=0} = 0$. Thus $\Delta\tau$ is selected to be 0.010. The external field is increased linearly within 2500 steps from $H_{ext} = 0$ at $\tau = 0$ to $H_{ext} = H_{c2}$ and along 10^6 time steps. With these parameters, the magnetization Mz defined in Eq. 2.31 is numerically calculated and plotted in Fig. 2.5. It's quite obvious from the figure that when $H_{ext} \leq 0.214$ the sample remains in a Meissner state and the sample enters in the vortex state as the field is increased above H_{c1} until the sample becomes completely normal at H_{c2}. It should be noted here that the numerical noise associated with solving TDGL equations results in the oscillations appear in the mixed state region ($H > H_{c1}$) of the figure.

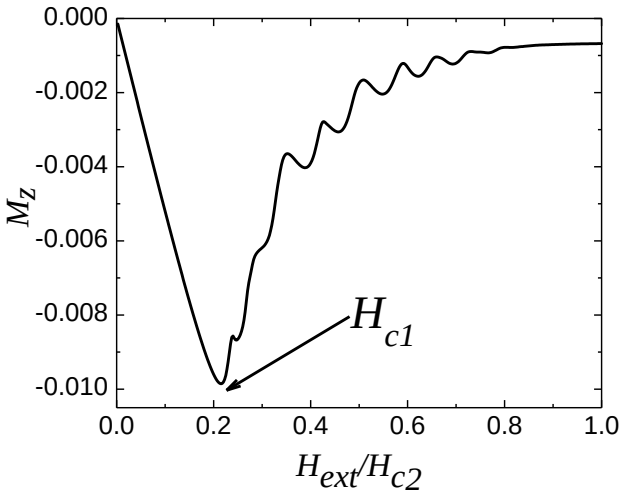

Figure 2.5: The magnetization curve versus the normalised applied field H_{ext}/H_{c2}. When the field $H_{ext}/H_{c2} < 0.203$, the sample remains in a Meissner state. As the field is increased above H_{c1} vortices emerge [see Fig. 2.6] and $|M_z|$ decreases and the vortices density increases gradually until the sample enters the normal state at H_{c2}. The results agrees with these obtained in [24]. The oscillations appear in the mixed state region of the figure is due to the numerical noise associated with solving TDGL equations.

The spacial distribution of order parameter $|\psi|^2$ of the sample is calculated at several values of the external field between $0.0 \leq H_{ext} \leq H_{c2}$ and presented in the density plot shown in Fig. 2.6. The figures show that the superconducting state is consistent with magnetization curve given in Fig. 2.5, where sample enters the normal state when $H_{ext} > H_{c2}$ and the superconducting state start significantly depressed when $H_{ext} = 0.40$ where the number of vortices increases gradually until their density becomes large enough which finally makes the sample entirely normal at $H_{ext} = H_{c2}$. However, the superconducting state remains preserved at the edges of the sample when the applied field is lower the H_{c2}.

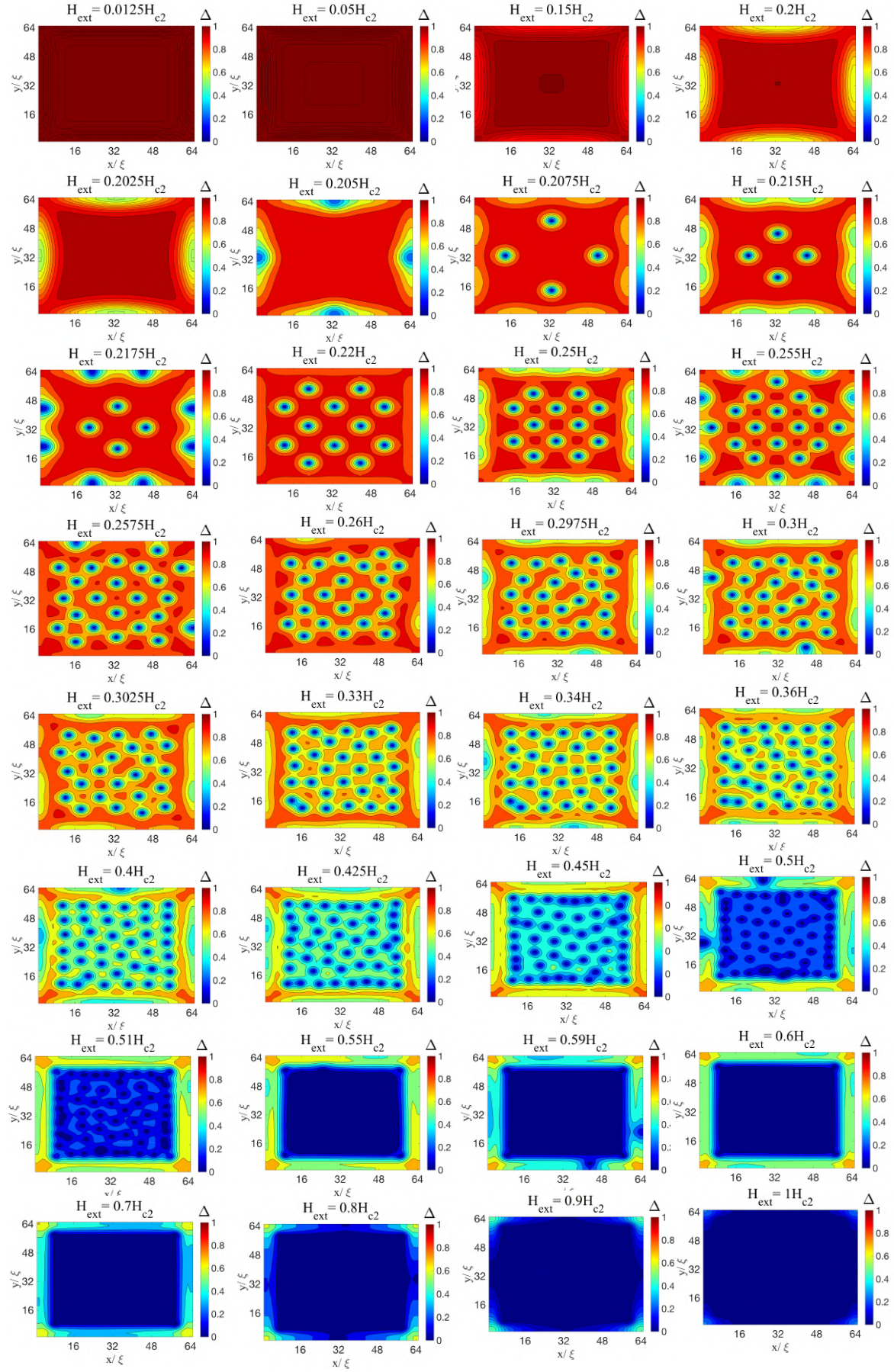

Figure 2.6: Density plots of the order parameter $\triangle = |\psi|^2$ for different external fields between $0.0 \leq H_{ext} \leq H_{c2}$

2.3 Bardeen–Cooper–Schrieffer (BSC) theory

2.3.1 General overview

A prominent microscopic theory of superconductivity is Bardeen-Cooper-Schrieffer (BCS) theory [25, 26, 27, 28]. Electrons classified as fermions in the normal conductor are considered as Bosons (Cooper pairs) in the BCS theory where they can coherently condensate into a single quantum state. Several experimental observations discussed in the previous sections, as zero electrical resistance, perfect diamagnetism and the phase transition below or at T_c, are formulated and tackled whiten the frame of the BCS theory. BCS theory is essentially based on three views: (i) the interaction between electrons can be an attractive potential mediated by the phonons, (ii) for a system of two electrons (single Cooper pairs) outside an occupied Fermi surface, Cooper found that, from solution of the Schrodinger equation of the system, electrons form a stable pair bound state, no matter how weak the attractive force is. And (iii) finally, Schrieffer constructed a many-body wave function from which he showed that all the electrons near to the Fermi surface are paired up, which leads to a coherent state wave function. As consequence, BCS energy gap emerges, that is defined as the energy required for breaking up a pair into two free electrons.

2.3.2 Single Cooper pair

BCS theory is based on three different views. Regarding to the first and the second ones, two electrons with and attractive potential are considered. Thus, the Schrödinger equation for these electrons is given [29] by

$$\left(-\frac{\hbar^2}{2m}\nabla^2_{\mathbf{r_1}} - \frac{\hbar^2}{2m}\nabla^2_{\mathbf{r_2}} + V(\mathbf{r_1}-\mathbf{r_2})\right)\psi(\mathbf{r_1},\mathbf{r_2}) = \ E\psi(\mathbf{r_1},\mathbf{r_2}), \tag{2.56}$$

where $\psi(\mathbf{r}_1,\mathbf{r}_2)$ is the wave-function, E is the energy, m the electron mass, and $V(\mathbf{r_1}-\mathbf{r_2})$ is the attractive potential. By changing the variables to the relative displacement $\mathbf{r} = \mathbf{r_1}-\mathbf{r_2}$, and to the center of mass coordinates $\mathbf{R} = \frac{1}{2}(\mathbf{r_2}+\mathbf{r_2})$, the Schrödinger equation becomes

$$\left(-\frac{\hbar^2}{2m^*}\nabla^2_{\mathbf{r}} - \frac{\hbar^2}{2\mu}\nabla^2_{\mathbf{R}} + V(\mathbf{r})\right)\psi(\mathbf{r},\mathbf{R}) = \ E\psi(\mathbf{r},\mathbf{R}), \tag{2.57}$$

where $m^* = 2m$ is the total mass and $\mu = \frac{m}{2}$ is the reduced mass. The potential is independent of coordinate of the center of mass coordinate $\mathbf{R}$, therefore the solution can be written as $\Psi(\mathbf{r},\mathbf{R}) = \psi(\mathbf{r})\exp(i\mathbf{K}\cdot\mathbf{R})$. Thus, the Schrödinger equation becomes

$$\left(-\frac{\hbar^2}{2\mu}\nabla^2_{\mathbf{r}} + V(\mathbf{r})\right)\psi(\mathbf{r}) = \left(E - \frac{\hbar^2\mathbf{K^2}}{2m^*}\right)\psi(\mathbf{r}). \tag{2.58}$$

The eigenvalue $E - \frac{\hbar^2 K^2}{2m}{}^*$ is minimised when the momentum of the center of mass vanishes ($\mathbf{K} = 0$), i.e. the two electrons have opposite momenta. By introducing the Fourier

transform on the wavefunction, $\psi(\mathbf{k}) = \int d^3r\psi(\mathbf{r})\exp(-i\mathbf{k}\cdot\mathbf{r})$, The Schrödinger equation gives

$$\int \frac{d^3k'}{(2\pi)^3}V(\mathbf{k}-\mathbf{k}')\psi(k') = (E-2\mathcal{E}_k)\psi(\mathbf{k}), \tag{2.59}$$

where a change of variables are made as $\mathbf{q} = \mathbf{k}-\mathbf{k}'$, and $\mathcal{E}_k = \frac{\hbar^2k^2}{2m}$. By modifying the wave function $\Delta(\mathbf{k}) = (E-2\mathcal{E}_\mathbf{k})\psi(\mathbf{k})$, the Schrödinger equation becomes

$$\Delta(\mathbf{k}) = -\int \frac{d^3k'}{(2\pi)^3}\frac{V(\mathbf{k}-\mathbf{k}')}{(E-2\mathcal{E}_{k'})}\Delta(\mathbf{k}'). \tag{2.60}$$

By (i) considering an attractive potential $V(\mathbf{k}-\mathbf{k}') = -V_0$ for $\mathcal{E}_k$, $\mathcal{E}_{k'} < \omega_D$ and zero elsewhere, where ω_D is the Debye frequency [1], (ii) considering a constant solution with $\Delta(\mathbf{k})= \Delta$ that implies an even spatial wave-function $\psi(\mathbf{r})=\psi(-\mathbf{r})$ which satisfies the singlet state where the spins of the two electrons must be anti-parallel, and (iii) defining the density of states per spin of a two-electron system: $\rho(\mathcal{E}) = \frac{m^{3/2}}{\sqrt{2}\hbar^3\pi^2}\sqrt{\mathcal{E}}$, Eq. 2.60 leads [29] to

$$\frac{V_0m^{3/2}}{\sqrt{2}\hbar^3\pi^2}\left[\sqrt{\omega_D} - \sqrt{\frac{-E}{2}}\arctan\left(\sqrt{\frac{2\omega_D}{-E}}\right)\right] = 1, \tag{2.61}$$

Eq. 2.61 determines the value of the bound state energy with $E < 0$ in terms of the attractive potential V_0. To obtain the minimum value of $V_{0,min}$, E is set to $E \to 0^-$. Thus

$$V_{0,min} = \frac{\sqrt{2}\hbar^3\pi^2}{m^{3/2}\sqrt{\omega_D}}. \tag{2.62}$$

This implies that there will be a bound state only if the attractive interaction is strong enough. However, in the actual many-body system, only the electrons near the Fermi level will be affected by the attractive interaction which can be tackled by (i) considering the an attractive potential $V(\mathbf{k}-\mathbf{k}') = V_0$ for the unoccupied electronic states above the Fermi energy, and (ii) by approximating the density of states for its value at the Fermi level $\mathcal{E}_F$. Thus Eq. 2.60 becomes [29]

$$\frac{2}{V_0\rho(\mathcal{E}_F)} = \ln\left(\frac{2\mathcal{E}_F - E + 2\omega_D}{2\mathcal{E}_F - E}\right). \tag{2.63}$$

By defining the binding energy $E_b = 2\mathcal{E}_F - E$, and for small $V_0\rho(\mathcal{E}_F) << 1$, the $E \to 2\mathcal{E}_F$, therefore the term $2\mathcal{E}_F - E + 2\omega_D \approx 2\omega_D$. Thus the binding energy reads

$$E_b = 2\omega_D\exp(-\frac{2}{V_0\rho(\mathcal{E}_F)}), \tag{2.64}$$

[1] The Debye frequency ω_D is the maximum vibrational frequency in a lattice.

This implies that a bound state is formed without taking into account the value of the attractive potential, whether it's small or not. This bound state is what called a Cooper pairs.

2.3.3 Cooper pairs in terms of many-body system

Using mean-field theory, the problem of single cooper pair can be extended for a system of many Cooper pairs. Detailed analysis of the BCS state for many Cooper pairs is beyond the scope this thesis, where I here cover some results as obtained on the basis of BCS state using mean-field theory. Based on the these results, the gap equation reads [29, 30, 31]

$$\Delta_{\mathbf{k}} = -\frac{1}{2}\sum_{k,q}\frac{V_{kq}\Delta_q}{2E_q}\tanh\left(\frac{E_q}{2k_BT}\right), \tag{2.65}$$

from which the nonzero solution for the gap $\Delta(T)$ can be obtained below a critical temperature T_c. At $T < T_c$, the properties of the system are qualitatively different from the normal metal. To simplify this, the scattering potential was approximated as $V_{k,q} = -V_0$ for $|\mathcal{E}_k| < \hbar\omega_D$, and zero for $V_{k,q} = -V_0$ for $|\mathcal{E}_k| > \hbar\omega_D$. With this approximation the second-order transition temperature in zero magnetic field leads to

$$kT_c = 1.14\hbar\omega_D \exp\left(-\frac{1}{\rho_F V_0}\right), \tag{2.66}$$

where ρ_F is the density of states at the Fermi surface. At zero temperature, the gap reads [29, 30, 31]

$$\Delta_0 = 1.764kT_c. \tag{2.67}$$

By combining the last two equations, the gap at $T = 0$ becomes [29, 30, 31]

$$\Delta_0 \approx 2\hbar\omega_D \exp\left(-\frac{1}{\rho_F V_0}\right). \tag{2.68}$$

Thus an arbitrarily small attractive interaction V_0 gives rise to a finite gap at zero temperature.
Near the critical temperature there is another form for the gap suggested by M. J. Buckingham [30, 31, 32]

$$\Delta(T \to T_c) \approx 3.06\, k_B T_c \sqrt{1 - (T/T_c)} \tag{2.69}$$

One of main predictions of the BCS theory is the presence of an energy gap at the Fermi level. Such a gap is an interpretation for the experimental observation of an exponential decay of superconductors specific heat at low temperatures which suggests that the energy spectrum of a superconductor is gapped. This gap is not observed in normal metals due to the fact that the low cost of excitation energy of the most energetic electrons near the Fermi level.

A direct consequence of the energy gap is the specific heat suppression of superconductor. Another experimental observation is the isotope effect [33], where it has been shown that the critical temperature T_c decays with $M^{1/2}$ where M is the mass of the isotope. As the mass reflects the lattice formation, this indicates the role of phonons in the superconducting state formation.

2.4 Langer, Ambegaokar, McCumber and Halperin (LAMH) theory & Skocpol, Beasley Tinkham (SBT) model

2.4.1 LAMH theory

For a superconductor of one-dimensional geometry, the Mermin-Wagner-Hohenberg theory [34, 35] state that a long-range order is impossible. In such superconducting system (long and thin wire), the order parameter fluctuates to zero at some point along the wire, allowing the relative phase across the point to slip by 2π [36]. Phase slip events cause voltage pulses which finally lead to resistive steps in the $I(V)$ curves of the wire. Langer, Ambegaokar, McCumber and Halperin (LAMH) [37, 38] have developed a theory in which a phase slip event is attributed to thermal activation when the system passes over a free-energy barrier proportional to the cross-sectional area of a wire. Experimentally, LAMH theory was confirmed [39] using tin whiskers of 0.5 μm diameter.
Resistive fluctuations in a narrow wire, or the variations in the magnitude of the superconducting order parameter can be described by the Ginzburg-Landau theory in which the free energy of a superconductor wire with length L and cross-sectional area $A = \pi R^2$ can be written in the form

$$F = A \int_0^L \big(|\nabla\psi(x)|^2 + \alpha|\psi(x)|^2 + \frac{\beta}{2}|\psi(x)|^4\big)dx, \tag{2.70}$$

where α and β are arbitrary parameters chosen to normalize the order parameter $|\psi(x)|^2$ that defined for 1D by $\psi(x) = \Delta(x)\exp[i\varphi(x)]$, and assumed to vary slowly along the x-direction and be essentially constant in the transverse directions. The Ginzburg-Landau equation is a results of the stationary condition $\frac{dF}{d\psi} = 0$, from which one obtains

$$-\nabla^2\psi(x) + \alpha\psi(x) + \beta|\psi(x)|^2\psi = 0. \tag{2.71}$$

In presence of magnetic field, the operator ∇ is replaced by $\nabla - \frac{-2ie}{\hbar c}\mathbf{A}$. Eq. 2.71 leads to following helix solution:

$$\psi(x) = \sqrt{\frac{\alpha - k^2}{\beta}}\exp\big[-i\varphi(x)\big], \tag{2.72}$$

where $\varphi(x) = kx$, and k is the allowed wavevectors with $k = \frac{2\pi}{L}n$, in which n is an integer

that satisfies periodic boundary conditions $\varphi(x+L) = \varphi(x) + 2\pi n$. Here, it should be taken into account the flux quantization condition which reads

$$\oint \nabla\varphi \cdot \ell = 2n\pi. \tag{2.73}$$

Furthermore, the potential difference V between a finite wire terminals is a time derivative of the total phase difference which is by Josephson relation, $\frac{d\Delta\varphi}{dt} = \frac{2eV}{\hbar}$, where $\Delta\varphi = \varphi(L) - \varphi(0)$. According to this relation, when $V = 0$, the phase difference is constant, which implies that the current oscillates forming an ac current. This relation also implies for a finite voltage, the phase difference φ is linearly proportional with time.
Phase slips, which are described by the LAMH theory [40, 38] leads to a nonzero resistance for any 1D wire at any finite temperature. The nonzero resistance is a result of phase jumps by 2π of the phase difference. For unbiased samples the number of the phase slip events in which $\Delta\varphi = 2\pi$ is the same as number of anti-phase-slip events in which $\Delta\varphi = -2\pi$. When the sample is biased, the number of phase slips becomes larger than number of anti-phase-slips. As result, a voltage emerges on the sample with $V = \frac{\hbar\Delta\dot{\varphi}}{2e}$. As the order parameter is suppressed to zero, the energy of the system during a phase slip event increases. As result of the TDGL theory for the case of a long and thin wire, the attempt frequency $\Omega(T)$ derived is given by [38]

$$\Omega(T) = \frac{L}{\xi(T)}\frac{1}{\tau_{GL}}\left(\frac{\Delta F}{k_B T}\right)^{1/2}, \tag{2.74}$$

where the wire and L is the length of the wire, $\xi(T)$ is the GL coherence length, and τ_{GL} is the relaxation time of the time dependent GL theory, which reads

$$\tau_{GL} = \frac{\pi\hbar}{8k_B(T - T_c)}, \tag{2.75}$$

in which $\left(\frac{\Delta F}{k_B T}\right)^{1/2}$, is a correction factor for the overlap of fluctuations at different regions of the wire, and the factor $\frac{L}{\xi(T)}$ gives the number of statistically independent regions in the wire [38, 41]. For a single phase slip, the barrier of the free energy reads [37, 42]

$$\Delta F = \frac{8\sqrt{3}}{3}\frac{H_c^2(T)}{8\pi}A\xi(T), \tag{2.76}$$

in which $\frac{H_c^2(T)}{8\pi}$ is the condensation energy density, and $\frac{8\sqrt{3}}{3}A\xi(T)$, is the effective volume, where A the cross-section area of the wire. The time averaged of the nonzero voltage V caused by a bias current I is given by

$$V = \frac{\hbar\Omega(T)}{e}\exp\left(\frac{-\Delta F}{k_B T}\right)\sinh\left(\frac{I}{I_0}\right), \tag{2.77}$$

where $I_0 = 4ek_B/h$. Thus, the differential resistance reads

$$\frac{dV}{dI} = \frac{\hbar\Omega(T)}{eI_0} \exp\left(\frac{-\Delta F}{k_B T}\right) \cosh\left(\frac{I}{I_0}\right). \tag{2.78}$$

In the limit of low currents $I \ll I_0$, one can assume that there is a linear resistance coming from Ohm's law. Thus

$$R_{LAMH} = R_q \left(\frac{\pi\Omega(T)}{k_B T}\right) \exp\left(\frac{-\Delta F}{k_B T}\right), \tag{2.79}$$

where $Rq = \frac{h}{(2e)^2} = 6.5\ \mathrm{k}\Omega$. With this approach, the fluctuation resistance does not explicitly depend on the normal resistance of the wire.

According to Little's model [41, 43, 44], Eq. 2.79 was modified to estimate the contribution of thermally activated phase slips (TPS), where $R_{WL} = R_N \exp(-\Delta F_{WL}/k_B T)$. As a result, the free energy barrier reads

$$\Delta F_{TPS} = \left[-0.83 k_B \frac{\beta w d R_q}{\rho_n \xi_0} \left(1 - \frac{T}{T_c}\right)^{3/2} T_c \right], \tag{2.80}$$

Thus, the final expression for the normal resistance of the wire reads

$$R_{TPS} = R_N \left[-0.83 \frac{\beta w d R_q}{\rho_n \xi_0} \left(1 - \frac{T}{T_c}\right)^{3/2} \frac{T_c}{T} \right], \tag{2.81}$$

where w is the width of the bridge, d is thickness of the film, ρ_n is the normal resistivity, $A = wd$, and the parameter $\beta = \frac{8\sqrt{2}\xi(T)}{3}$ measures the ratio of the phase slip length along the bridge to the effective length of a phase slip in a 1D wire.

2.4.2 Skocpol, Beasley and Tinkham (SBT) model

A model of the resistive current state in an extended 1D system was proposed by [45] Skocpol, Beasley and Tinkham (SBT). In this model, the framework of the quasiparticle diffusion [46] was integrated with phase slip processes. The model suggests, when a superconducting wire is biased with current $I < I_c$, where the voltage drop between the two ends of the wire is ideally assumed to be zero, thermal fluctuations and/or quasiparticle diffusion cause a small but nonzero voltage. As this voltage is related to the phase by $d\varphi/dt = 2eV/\hbar$, the phase increases. To the maintain steady state, the phase will keep increasing until instantaneously slips by 2π [45]. Within this short period of time, the superconducting energy gap vanishes and the order parameter suppresses at the core of what called phase-slip centres (PSCs) that considered as a source for dissipation and fluctuations. Historically, SBT models was restricted for 1D superconductors before extending it for wider superconducting wires (2D system or quasi 1D superconductors) in terms of what called phase slip lines (PSL). As consequence of PSCs, steps occur around transition region in the $I(V)$ curve of the system. The extrapolation for slopes of the

linear part following the resistive steps converge to a nonzero current I_s at zero voltage. Within this framework, the generated voltage by PSCs reads

$$V(I) = R(I_{Is})\frac{2n\Lambda}{L}\tanh\left(\frac{L}{2n\Lambda}\right), \tag{2.82}$$

where R is the normal state resistance of the track, n is the number of PSCs, L is the track length, is the quasiparticle diusion length, and I_s is the intercept of the slopes on the current axis determined by the time-average supercurrent at the center of the PSC.

2.5 Transport properties of thin superconducting strips

As already demonstrated in Sec. 2.2.5, if a superconducting film is placed in magnetic field with $H > H_c$, Abrikosov vortices penetrate the film and form a lattice. When transport current is applied to the film, the vortices experience the Lorentz force of the current. As a result of vortex motion, the energy of system dissipates, finite voltage and electrical field in the superconductor emerge. In other words, this causes a hysteresis behaviour in the $I(V)$ characteristic according to Larkin and Ovchinnikov (LO) prediction [47]. At the end of the 1970s it was speculated that lines with fast vortex motion called phase slip lines (PSLs) should appear in the superconductor at the transition point [48]. However, as the analytical calculations are strongly restricted due to the mathematical complexity of the problem, only a semi-quantitative analysis was made using the assumption that phase-slip lines are already exist in the sample [48, 49, 50]. In this section, theoretical and experimental investigations for superconducting strips are reviewed.

2.5.1 Theoretical investigations

In Ref [48, 49] nonequilibrium processes in a superconducting stripe in the presence of a transport current have been investigated, where the influence of the finite length of the stripe and it's normal current contacts on the $I(V)$ characteristics have been theoretically considered using the TDGL theory, where the dynamics of superconducting vortices for a model with superconducting stripe with computational unit cell of lateral dimensions L and W, and thickness d is smaller than the coherence length ξ and the penetration depth λ. For such model, a current is applied along the x, and the TDGL equations can be written as:

$$\frac{u}{\sqrt{1+\gamma^2|\psi|^2}}\left(\frac{\partial}{\partial t}+i\varphi\frac{\gamma^2}{2}\frac{\partial|\psi|^2}{\partial t}\right)\psi = (\nabla - i\mathbf{A})^2\psi + (1-|\psi|^2)\psi, \tag{2.83}$$

$$\frac{\partial \mathbf{A}}{\partial t} = \Re[\psi^*(i\nabla - \mathbf{A})\psi] - \kappa^2\nabla\times\nabla\times\mathbf{A}, \tag{2.84}$$

the parameter $\gamma = 2\tau_{in}\Delta(T)/\hbar$ is the product of the inelastic collision time τ_{in} for electron-phonon scattering [48], and $\Delta(T) = 4k_BT_cu^{1/2}/\pi\sqrt{1-T/T_c}$ is the order parameter at

temperature T which follows from Gor'kov's derivation [11] of the Ginzburg-Landau equations.

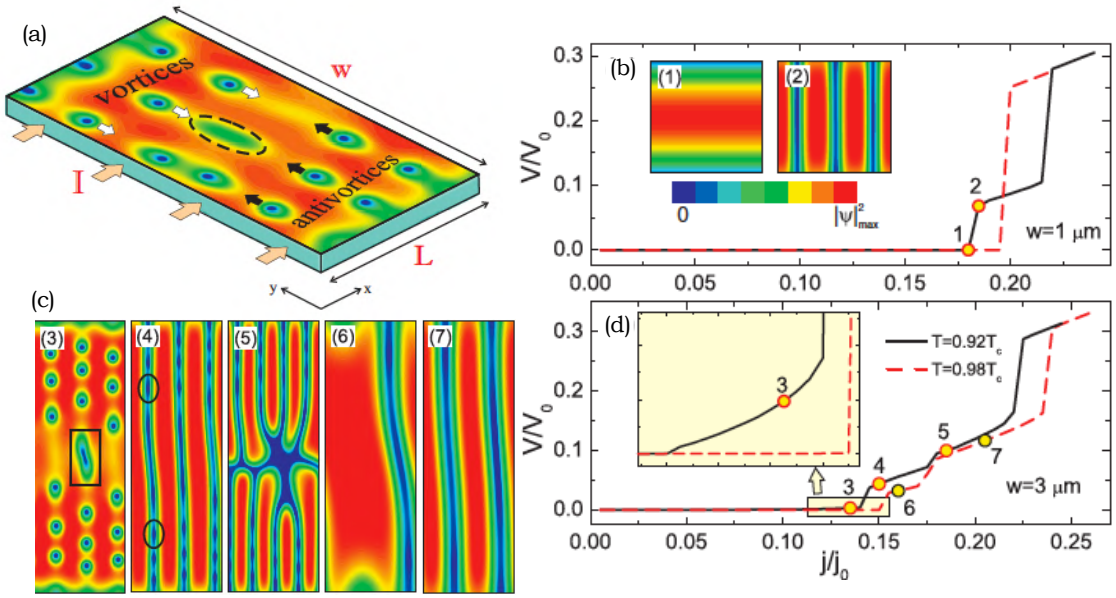

Figure 2.7: (a) The model system: a superconducting film (width W and with periodic boundary condition in the x direction) under applied dc current (I). A density plot of the order parameter $|\psi|^2$ of a superconducting film, in which the direction of moving vortices/antivortices indicated by white/black arrows. Time-averaged voltage against current-density $I(V)$ characteristics of the sample with width $W = 1$ μm (a) and $W = 3$ μm (d) at temperatures $T = 0.92T_c$ (solid black curve), and $T = 0.98T_c$ (dashed red curve). The length of the computational unit cell is $L = 1$ μm and the GL parameter is $\kappa = 10$. Inset in (d) shows the lower part of the $I(V)$ curve. (c) Panels 1-7 show snapshots of the density plot of the order parameter $|\psi|^2$ for current values indicated on the $I(V)$ curves. Black square in panel 3 shows the annihilation region of a vortex-antivortex pair and black circles in panel 4 indicate the positions of a fast-moving vortex (on top) and an antivortex (bottom). Adapted from [49].

Eqs. 2.83 and 2.84 are scaled to be dimensionless, where the temperature is written in terms of the critical temperature T_c, the vector potential $A = (A_x, A_y, 0)$ and the momentum $p = \nabla\phi - \mathbf{A}$ are scaled relative to $\Phi_0/2\pi\xi$, the order parameter $\psi = \psi_0 \exp(i\varphi)$ is scaled relative to Δ_0, the film coordinates are scaled in units of the coherence length $\xi(T) = (8k_B(T_c - T)/\pi\hbar D)^{1/2}$ (D is the diffusion constant), the time is scaled relative to Ginzburg-Landau relaxation time $\tau_{GL} = \pi\hbar/8\pi T_c u$, the voltage V is scaled using the normal-state conductivity (σ_n) relative to $\varphi_0 = \sigma_n\hbar/2e\tau_{GL}$, the magnetic field is scaled relative to $H_{c2} = \Phi_0/2\pi\xi^2$, and the current density is scaled relative to $J_0 = \sigma_n\hbar/2\pi e\tau_{GL}\xi_0$. In those calculations [48], the parameter u has been selected to be 5.79 following the value given in [11]. TDGL equations have been numerically solved to obtain the $I(V)$ characteristic in the absence of an external applied magnetic field. The transport current I, was introduced via the boundary condition for the vector potential in the x-direction of the film with $\nabla \times \mathbf{A}|_z(x = 0, W) = H \pm H_I$, where $H_I = 2\pi I/c$ is the magnetic field induced by the current I (per unit length in the z-direction), and H is the applied magnetic

field. The potential differences can be calculated using the integral form expressed by [51]

$$V(t) = \int_0^L \left(\frac{1}{W} \int_0^W \left(\frac{d\mathbf{A}}{dt} dy \right) \right) dx, \tag{2.85}$$

where L and W are the dimensions of the superconducting stripe away from the superconducting/normal interface. TDGL equations describe the oscillations of the order parameter in superconductors which occurs in form of waves propagating across the sample. Such waves that carries the the order parameter, are called kinematic vortices [49, 48, 52]. In Ref [53], Vodolazov *et al* have shown that a phase-slip line occurs at time t, consists of a line of counter propagating as vortices and antivortices which are created on the opposite edge of the film [Fig. 2.7(a)], and overlap at the center of the sample where they annihilate.

In Ref [49], calculations for a superconducting stripe with length $L = 1$ μm, and different values of the width W with coherence length $\xi_0 = 10$ nm, were considered as a representative example. To construct the $I(V)$ characteristics of the sample, the voltage signal has been averaged over a time interval much larger than the characteristic voltage variations. For the system with $W = 1$ μm, the zero resistance of the sample has been maintained up to a threshold current j_c at the point indicated by 1 in Fig. 2.7(a), above which the system goes into the resistive state with a finite jump in the output voltage indicated by point 2. By increasing temperature the system transports from the Meissner state into the normal state as shown by the dashed line plotted in Fig. 2.7 which also shows a none-resistive state. Fig. 2.7(c) shows the $I(V)$ characteristics of the sample with $W = 1$ μm. The figure was linked to the panel given in the figure, where vortices are created periodically at the opposite edges of the sample and annihilate in the middle as marked by a black square in panel 3 linked to point 3 in the $I(V)$ characteristics. With increasing the applied current, a larger nucleation rate of vortex-antivortex pairs are induced, vortex lattice gets distorted, and a rectangular lattice of vortices can be observed. This can be seen in the panel 4 of Fig. 2.7(d), where a phase-slip line enters the sample (in the middle where the order parameter $|\psi|^2 \approx 0$), and causes the finite transition indicated by point 4 in the $I(V)$ curve. By increasing the applied current to higher values, more channels (phase-slip lines) appear as these shown in panel 5 which associated with a new transition in the $I(V)$ curve indicated by point 5. However, for panel 6 the number of phase-slip lines decreases with temperature in comparison to panels 5 and 7. This due to the fact that the sample in units of the characteristic length scales, i.e, $\xi(T)$, and $\lambda(T)$, becomes shorter at high temperatures, which finally makes accommodating more phase-slip lines difficult.

In Ref [49], $V(t)$ characteristics for a system with $L = 1$ μm and $W = 2$ μm have been investigated. Fig. 2.8 shows the time evolution of $V(t)$ curves at different values of dc applied currents with duration $1000t_0$, where $t_0 = 10$ ps. Curves I and II in Fig. 2.8(a) have been calculated at currents $J = 0.12J_0$, and $J = 0.14J_0$ respectively, in which the output voltage oscillates in time with well defined maxima that correspond to a vortex penetration (panel 1), or an annihilation of a vortex-antivortex pair (panel 2). An increase in the applied current results in formation of phase-slip lines such that shown in the panels 3 and 4, which significantly increases the output voltage as shown in Fig. 2.8(b). A further increase in the applied current increases the nucleation rate of vortex-

antivortex pairs, as well as the number of phase-slip lines, and the output voltage. The voltage reaches a maxima just before the formation of phase-slip lines (point 5), which are due to nonequilibrium effects (see panel 5). A further increase in applied current increases the number and velocity of vortex-antivortex pairs which leads to the appearance of local hot spots in which the density of Cooper pairs reduces to zero. These spots indicated by the blue areas in the panel 6, are first created near the sample edges at $t \approx 100t_0$, and quickly propagate to middle of the sample at $t > 200t_0$ (panel 7). At this state, the average of the voltage signal increases, and the sample becomes more resistive. The area of the hot spots evolves with time and spreads to occupy more space, which results in a further increase in the average of the voltage signal until the entire system goes into a transition to the normal state.

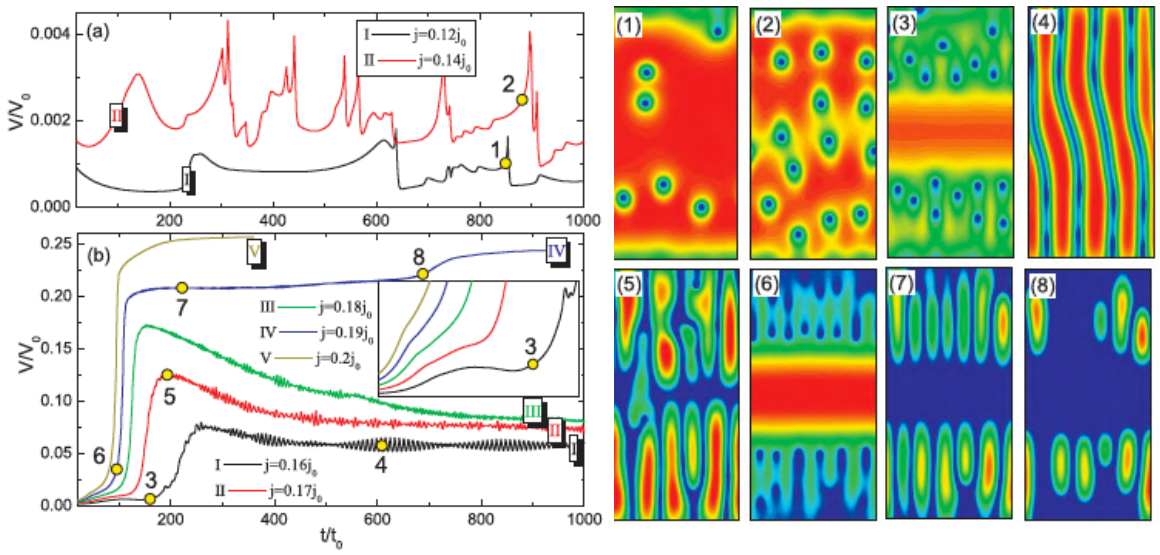

Figure 2.8: Calculations of $V(t)$ characteristics of a sample with $L = 1$ μm $[L = 31.6\xi(T)]$ and $W = 2$ μm $[W = 63.3\xi(T)]$ at $T = 0.9T_c$, and for different values of the applied current. Panels 1-8 are density plot of the order parameter $|\psi|^2$. Inset of (b) shows a narrow window of the $V(t)$ curves. Adapted from [49].

2.5.2 Earlier experimental investigations

Experimental results on $I(V)$ characteristics of a mesoscopic superconducting NbN wire with several superconducting contacts shown in Fig. 2.9(a) have been reported in [54]. Figs. 2.9(b)-(f) show the $I(V)$ curves of each segment with lengths of 36, 6 and 12 μm respectively. Gray curves in Figs. 2.9(b)-(f) are the $I(V)$ characteristics when the segments are driven by voltage. For this case, the nonequilibrium regions become more obvious compare to those obtained for the same segments driven by current. This indicates that there is a possibility for the existence of several normal resistive regions simultaneously. However, for the current sweep down, a continuous behaviour is found without any jump between different resistive states. The reported normal-state resistance of the segments just above T_c is quite high 8.5 kΩ/m.

It's quite obvious from Fig. 2.9 that the measured $I(V)$ curves show a clear hysteresis with finite steps, where the number of these steps increases as the length of the segment of

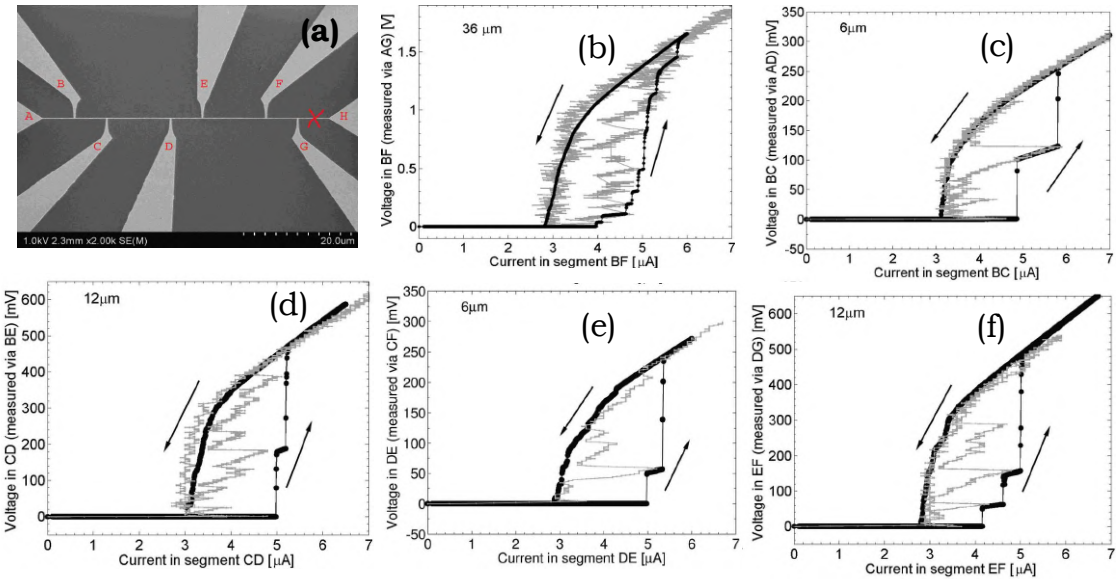

Figure 2.9: (a) A scanning electron microscopy image of a NbN nanowire with attached current and voltage electrodes. $I(V)$ characteristic of (b) the segment BF with 36 μm long, 70 nm wide, and 75 nm thick, (c), (d), (e), and (f) $I(V)$ characteristic of BC, CD, DE, and EF segments with 6 μm or 12 μm long, 70 nm wide, and 75 nm thick. All curves were measured with current drive (black curve) and (or) with voltage drive (gray curve) at $T = 4.2$ K. More finite resistive steps occur around the transition region of the $I(V)$ curves as the superconducting segment becomes longer. This indicates more phase-slip events as theoretically underlined by simulations using the TDGL equations such that given in Fig. 2.7. Adapted from [54].

the superconducting wire increases. The increase in the number of these steps indicating an increasing number of phase-slip events, as each step corresponds to phase-slip lines entering the sample. In other words, the transport properties shown in the figure imply that the resistive domains of superconducting segments scale with their lengths. Such argument is supported by numerical simulations using the TDGL equations shown in Fig. 2.7 given in previous subsection.

Bibliography

[1] de Bruyn Ouboter, Rudolf. "Heike Kamerlingh Onnes's discovery of superconductivity." Scientific American **276**. (3), 98-103 (1997).

[2] Kirton, Peter George, and A. D. Armour. "Nonlinear dynamics of a driven nanomechanical single-electron transistor." Physical Review B **87**.15 (2013): 155407.

[3] W. Meissner, and R. Ochsenfeld. "Ein neuer effekt bei eintritt der supraleitfähigkeit." Naturwissenschaften **21** .(44) 787-788 (1933).

[4] J F. Annett. "Superconductivity, superfluids and condensates." **5**. Oxford University Press (2004).

[5] S. Blundell. "Magnetism in condensed matter." Oxford University Press (2003).

[6] U. Essmann, and H. Träuble. "The direct observation of individual flux lines in type II superconductors." Physics letters A **24**. 10 (1967).

[7] A. A. Abrikosov. "The magnetic properties of superconducting alloys." Journal of Physics and Chemistry of Solids **2**. 3 (1957).

[8] F. London, and H. London. "The Electromagnetic Equations of the Supraconductor". Proceedings of the Royal Society A: Mathematical, Physical and Engineering Sciences **149** (866) (1935).

[9] L. Vitaly Ginzburg, and Lev D. Landau. "On the theory of superconductivity." On Superconductivity and Superfluidity. Springer, Berlin, Heidelberg, (2009).

[10] Dmitriev, A. V., and W. Nolting. "Details of the thermodynamical derivation of the Ginzburg–Landau equations." Superconductor Science and Technology **17**.3 (2004): 443.

[11] Gor'kov, Lev Petrovich. "Microscopic derivation of the Ginzburg-Landau equations in the theory of superconductivity." Sov. Phys. JETP 9.6 (1959): 1364-1367.

[12] Abrikosov, Alexei A. "On the magnetic properties of superconductors of the second group." Sov. Phys. JETP 5 (1957): 1174-1182.

[13] Buckel, Werner, and Reinhold Kleiner. "Superconductivity: fundamentals and applications." John Wiley & Sons, (2008).

[14] Buscaglia, Gustavo C., Carlos Bolech, and Arturo López. "On the numerical solution of the time-dependent Ginzburg-Landau equations in multiply connected domains." Connectivity and Superconductivity. Springer, Berlin, Heidelberg, 2000. 200-214.

[15] M. Tinkham, Introduction to Superconductivity, Mc Graw Hill, New York, 1975.

[16] Du, Qiang, Max D. Gunzburger, and Janet S. Peterson. "Solving the Ginzburg-Landau equations by finite-element methods." Physical Review B **46**.14 (1992): 9027.

[17] Kato, Ryuzo, Yoshihisa Enomoto, and Sadamichi Maekawa. "Computer simulations of dynamics of flux lines in type-II superconductors." Physical review B **44**.13 (1991): 6916.

[18] Enomoto, Y., and R. Kato. "Computer simulation of a two-dimensional type-II superconductor in a magnetic field." Journal of Physics: Condensed Matter **3**.3 (1991): 375.

[19] Liu, Fong, M. Mondello, and Nigel Goldenfeld. "Kinetics of the superconducting transition." Physical review letters **66**.23 (1991): 3071.

[20] Frahm, Holger, Salman Ullah, and Alan T. Dorsey. "Flux dynamics and the growth of the superconducting phase." Physical review letters **66**.23 (1991): 3067.

[21] Machida, Masahiko, and Hideo Kaburaki. "Direct simulation of the time-dependent Ginzburg-Landau equation for type-II superconducting thin film: Vortex dynamics and V-I characteristics." Physical review letters **71**.19 (1993): 3206.

[22] Milošević, M. V., and R. Geurts. "The Ginzburg–Landau theory in application." Physica C: Superconductivity **470**.19 (2010): 791-795.

[23] Gonçalves, W. C., *et al.* "Numerical solution of the time dependent Ginzburg-Landau equations for mixed (d+ s)-wave superconductors." Journal of Mathematical Physics **55**.4 (2014): 041501.

[24] Buscaglia, Gustavo C., Carlos Bolech, and Arturo López. "On the numerical solution of the time-dependent Ginzburg-Landau equations in multiply connected domains." Connectivity and Superconductivity. Springer, Berlin, Heidelberg, 2000. 200-214.

[25] Cooper, Leon N. "Bound electron pairs in a degenerate Fermi gas." Physical Review **104**.4 (1956): 1189.

[26] Bardeen, John, Leon N. Cooper, and J. Robert Schrieffer. "Microscopic theory of superconductivity." Physical Review **106**.1 (1957): 162.

[27] Schrieffer, J. Robert. Theory of superconductivity. CRC Press, 2018.

[28] Bardeen, John, Leon N. Cooper, and John Robert Schrieffer. "Theory of superconductivity." Physical review 108.5 (1957): 1175.

[29] Fernandes, Rafael M. "Lecture Notes: BCS theory of superconductivity."

[30] Bennemann, Karl-Heinz, and John B. Ketterson, eds. Superconductivity: Volume 1: Conventional and Unconventional Superconductors Volume 2: Novel Superconductors. Springer Science & Business Media, 2008.

[31] Tinkham, Michael. Introduction to superconductivity. Courier Corporation, 2004.

[32] Buckingham, M. J. "Very high frequency absorption in superconductors." Physical Review **101**.4 (1956): 1431.

[33] Maxwell, Emanuel. "Isotope effect in the superconductivity of mercury." Physical Review 78.4 (1950): 477.

[34] Mermin, N. David, and Herbert Wagner. "Absence of ferromagnetism or antiferromagnetism in one-or two-dimensional isotropic Heisenberg models." Physical Review Letters **17**.22 (1966): 1133.

[35] Hohenberg, Pierre C. "Existence of long-range order in one and two dimensions. "Physical Review **158**.2 (1967): 383.

[36] Lau, Chun Ning, et al. "Quantum phase slips in superconducting nanowires." Physical review letters 87.21 (2001): 217003.

[37] Langer, James S., and Vinay Ambegaokar. "Intrinsic resistive transition in narrow superconducting channels." Physical Review **164**.2 (1967): 498.

[38] McCumber, D. E., and B. I. Halperin. "Time scale of intrinsic resistive fluctuations in thin superconducting wires." Physical Review B **1**.3 (1970): 1054.

[39] Newbower, R. S., M. R. Beasley, and M. Tinkham. "Fluctuation effects on the superconducting transition of tin whisker crystals." Physical Review B **5**.3 (1972): 864.

[40] Ambegaokar, Vinay, and Alexis Baratoff. "Tunneling between superconductors." Physical Review Letters **10**.11 (1963): 486.

[41] Chu, Sang L., Anthony Travis Bollinger, and Alexey Bezryadin. "Phase slips in superconducting films with constrictions." Physical Review B **70**.21 (2004): 214506.

[42] Tinkham, M., and C. N. Lau. "Quantum limit to phase coherence in thin superconducting wires." Applied physics letters **80**.16 (2002): 2946-2948.

[43] Tinkham, M. "Introduction to Superconductivity ed. by McGraw-Hill." (1996).

[44] Brenner, M. W., Roy, D., Shah, N., Bezryadin, A. "Dynamics of superconducting nanowires shunted with an external resistor." Physical Review B **85**.22 (2012): 224507.

[45] Skocpol, W. J., M. R. Beasley, and M. Tinkham. "Phase-slip centers and nonequilibrium processes in superconducting tin microbridges." Journal of Low Temperature Physics **16**.1-2 (1974): 145-167.

[46] Hsieh, S. Y., and James L. Levine. "Diffusion of quasiparticles in superconducting aluminum films." Physical Review Letters **20**.26 (1968): 1502.

[47] Larkin, A. I., and Y. U. N. Ovchinnikov. "Nonlinear conductivity of superconductors in the mixed state." Sov. Phys. JETP **41**.5 (1975): 960-965.

[48] Berdiyorov, G. R., *et al.* "Finite-size effect on the resistive state in a mesoscopic type-II superconducting stripe." Physical Review B **79**.17 (2009): 174506.

[49] Berdiyorov, G., *et al.* "Dynamics of current-driven phase-slip centers in superconducting strips." Physical Review B **90**.5 (2014): 054506.

[50] Lempitsky, S. V. "Phase slippage lines in wide superconducting films." ZHURNAL EKSPERIMENTALNOI I TEORETICHESKOI FIZIKI **90**.2 (1986): 793-799.

[51] Machida, Masahiko, and Hideo Kaburaki. "Numerical simulation of flux-pinning dynamics for a defect in a type-II superconductor." Physical Review B **50**.2 (1994): 1286.

[52] Andronov, A., *et al.* "Kinematic vortices and phase slip lines in the dynamics of the resistive state of narrow superconductive thin film channels." Physica C: Superconductivity and its Applications **213**.1-2 (1993): 193-199.

[53] Vodolazov, D. Yu, and F. M. Peeters. "Rearrangement of the vortex lattice due to

instabilities of vortex flow." Physical Review B **76**.1 (2007): 014521.

[54] Elmurodov, A. K., *et al.* "Phase-slip phenomena in NbN superconducting nanowires with leads." Physical Review B **78**.21 (2008): 214519.

3 Superconducting Junctions & SQUIDs

3.1 Flux quantization

As previously demonstrated, superconductors can be described by a macroscopic wave function $\psi(\mathbf{r},t) = \exp\varphi(r,t)$. Here, the wavefunction describes the whole ensemble of the superconducting particles such that $\psi^*(\mathbf{r},t)\psi(\mathbf{r},t) = n^*(\mathbf{r},t)$, where $n^*(\mathbf{r},t)$ is the density of the superconducting particles.
Based on the London equations given in Sec. 2.1.3, and for a superconducting medium in a simply connected superconducting region, the magnetic flux threading such region is actually quantized. Over closed contours C and within a region S, such quantization can be written as

$$\oint_C (\mathbf{\Lambda J}_s)\cdot d\ell + \oint_S \mathbf{B}.d\mathbf{s} = n\frac{h}{2e} = n\Phi_0, \tag{3.1}$$

where $\Lambda = \frac{m_s}{n_s q_2^2}$, and the flux quantum $\Phi_0 = 2.06783384810^{-15}Wb$. Here, the quantity Φ_0 represents the flux quantum that is the smallest amount of flux. Experimentally, the flux quantization in superconducting cylinders and rings has been investigated and proved [1, 2] in 1961 by R. Doll and M. Näbauer in the Walther-Meissner-Institute in Munich and W. M. Fairbank at Stanford.

3.2 Josephson effect in superconducting weak links

3.2.1 General overview

The Josephson effect is a macroscopic quantum phenomenon predicted [3, 4, 5] in 1962 by Brian D. Josephson by introducing the mathematical relationships for the current and voltage across a weak link mediated by two superconductor banks. Several types [6] of weak links such as tunnelling junctions, or superconductor-insulator-superconductor (SIS) junctions, superconductor-normal metal- superconductor (SNS) junctions, nanobridge junctions of a narrow constriction, point-contact junctions, and weak links due to the proximity effect that are classified into types: a normal film causes local suppression of the order parameter of a superconducting film, and a small drop of solder on a superconducting wire. Fig. 3.1 shows the superconducting weak links mentioned above. It should be noted here, the theoretical work considered by Josephson was superconductor-insulator-superconductor (SIS) junctions. Experimentally, the DC Josephson effect had

been observed [4, 5] prior to 1962. However, this observation has been interpreted by "super-shorts" or breaches in the insulating barrier that lead to the direct conduction of electrons between the superconductors.

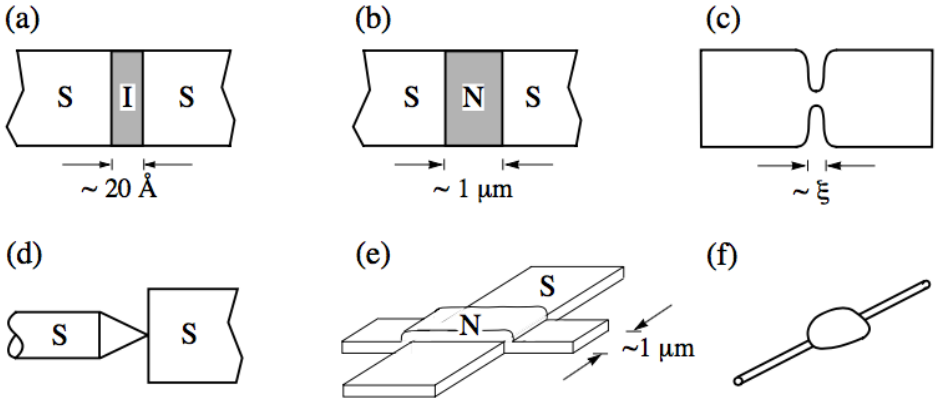

Figure 3.1: Some kinds of weak links: (a) SIS tunnelling junction, (b) SNS junction, (c) nanobridge with a narrow constriction, (d) point-contact junction, (e) and (f) weak links due to the proximity effect. Adapted from [6].

3.2.2 Dayem bridges

A Dayem bridge is a thin-film of the Josephson junction where two weakly coupled superconductor banks coupled by a weak link which consists of a superconducting bridge with dimensions in scale of the coherence length ξ. The properties of the whole junction depend on the width, thickness, and significantly on the ratio L/ξ where L is the length of the bridge. Here, I consider the two cases of Dayem Bridges: (i) short Dayem bridges relative to the coherence length ($L \leqslant \xi$), and (ii) long Dayem bridges where ($L > \xi$).

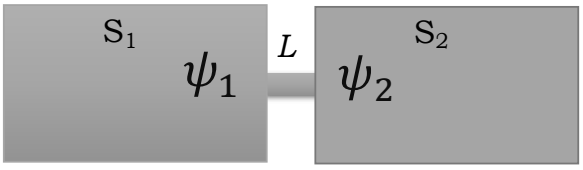

Figure 3.2: Two weakly coupled superconductor banks S_1 and S_2 with wavefunctions ψ_1 and ψ_2. A wavefunction of a superconducting electrode propagates through the interface, interfering with the other wavefunction propagting from the other electrode.

3.2.2.1 Short Dayem bridges ($L \leqslant \xi$)

I start with typical type of the Josephson junctions, where the length of the weak link is comparable with the coherence length of the superconducting electrodes. Fig. 3.2 shows two identical superconductor banks S_1, and S_2 coupled by a weak link (bridge) of length L. Here, the superconductors are described by the Ginzburg–Landau (GL) order parameter $\psi_1 = \sqrt{n^*_{s,1}}\exp(i\varphi_1)$, and $\psi_2 = \sqrt{n^*_{s,2}}\exp(i\varphi_2)$. After establishment of the weak link, each wave function propagates through the bridging region, where the wavefunction emerged

in the link region is described by interference between the independent wavefunctions ψ_1, and ψ_2. To quantitatively describe such system, the problem is simplified to be in one-dimensional. Thus, the problem can be solved using the 1D time independent Ginzburg- Landau Equation. Here, the left and right interfaces are assumed to be located at $x = 0$ and $x = L$ respectively. Also, the length of the weak link L is assumed to be too short relative to the coherence length of the superconducting electrodes, i.e. $L << \xi$. By assuming that the value of the superelectron density of the both electrodes are $|\Psi_0|^2 = n^*_{s,1} = n^*_{s,2}$, the wavefunction inside the bridge can be written as a superposition:

$$\Psi(x) = |\Psi_0| \exp(i\varphi_1) g(x) + |\Psi_0| \exp(i\varphi_2)[1 - g(x)], \tag{3.2}$$

with $g(x \to 0) = 1$, and $g(x \to L) = 0$ which are the functions used to match the wavefunction values at the interfaces. The first GL equation in 1D reads

$$-\frac{\hbar^2}{2m^*}\frac{\partial^2\Psi}{\partial x^2} + \alpha\Psi + \beta\Psi|\Psi|^2 = 0, \tag{3.3}$$

where α and β are in the initial argument were treated as phenomenological parameters. Now by introducing the reduced wavefunction $f(x)$ with $\Psi(x) = |\Psi_0| f(x)$, and using the relations $|\Psi_0|^2 = -\frac{\alpha}{\beta} = \frac{|\alpha|}{\beta}$, and $\xi^2 = \frac{\hbar^2}{2m^*|\alpha|}$, the GL equation can be rewritten in the reduced form

$$\xi^2\frac{\partial^2 f}{\partial x^2} + f - |f|^2 f = 0. \tag{3.4}$$

Thus, Eq. 3.2 takes the reduced wavefunction

$$f(x) = \exp(i\varphi_1) g(x) + \exp(i\varphi_2)[1 - g(x)]. \tag{3.5}$$

If $L \ll \xi$, the first term in Eq. 3.4 yields $\frac{\partial^2 f}{\partial x^2} \approx \frac{f}{L^2}$. Thus

$$\xi^2\frac{\partial^2 f}{\partial x^2} - \left(\frac{\xi}{f}\right)^2 f >> f. \tag{3.6}$$

This implies that the gradient term dominants Eq. 3.4. By applying the boundary conditions given earlier for $g(x)$ in which $g(x \to 0) = 1$, and $g(x \to L) = 0$, the solution for $g(x)$ can be obtained:

$$g(x) = 1 - \frac{x}{L}. \tag{3.7}$$

Thus, the function $f(x)$ given in Eq. 3.5 reads

$$f(x) = \left(1 - \frac{x}{L}\right) \exp(i\varphi_1) + \frac{x}{L} \exp(i\varphi_2), \tag{3.8}$$

which leads to the wavefunction that follows

$$\Psi(x) = |\Psi_0|\left[\left(1 - \frac{x}{L}\right)\exp(i\varphi_1) + \frac{x}{L}\exp(i\varphi_2)\right]. \tag{3.9}$$

The current-phase relation

Now the supercurrent density $J_s(x)$ can be obtained from the second GL Equation

$$\begin{aligned} J_s(x) &= -\frac{ie^*\hbar}{2m^*}\left(\Psi^*\frac{\partial\Psi}{\partial x} - \Psi\frac{\partial\Psi^*}{\partial x}\right) \\ &= \frac{ie^*\hbar}{2m^*}|\Psi_0|^2\left(f^*\frac{\partial f}{\partial x} - f\frac{\partial f^*}{\partial x}\right) \\ &= \frac{e^*\hbar}{2m^*}\Re(f^*\partial_x f) \\ &= \frac{2e\hbar}{2m^*}|\Psi_0|^2\Re\left[\left(1 - \frac{x}{L}(1-\exp(i\delta))\right)\frac{1}{L}(\exp(i\delta)-1)\right] \\ &= \frac{e^*\hbar}{2m^*}|\Psi_0|^2\Re\left[\exp(i\delta) - 1 - \frac{x}{L}|1-\exp(i\delta)|^2\right] \\ &= \frac{e^*\hbar}{2m^*}|\Psi_0|^2\frac{1}{L}\sin(\delta), \end{aligned} \tag{3.10}$$

where $\Re$ stands for the real part, $\delta = \varphi_2 - \varphi_1$, and $e^* = 2e$. By integrating over the junction cross-sectional area A the current reads

$$I = I_c\sin(\delta), \tag{3.11}$$

which is the current-phase relation of a typical Josephson junction with a critical current I_c that yields

$$I_c = \frac{e^*\hbar}{2m^*}|\Psi_0|^2\frac{A}{L}. \tag{3.12}$$

The voltage-phase relation

So far equilibrium properties of a Josephson junction were considered, where no bias is applied to the two superconducting electrodes. A problem with applied bias can be tackled with the time-dependent Ginzburg-Landau (TDGL) Theory. At equilibrium, the wavefunction yields the first GL equation, which has the form of the non-linear Schrödinger equation given in Eq. 3.4. In this limit, the time-dependent generalization for the GL wavefunction can simply given by the TDGL equation.

$$i\hbar\frac{\partial\Psi}{\partial t} = \mathcal{H}\Psi, \tag{3.13}$$

with stationary solutions $\Psi(x,t) = \exp(-\frac{iEt}{\hbar})\Psi(x)$. Thus the last equations leads to $i\hbar\frac{\partial\Psi}{\partial t} = E\Psi$, or in terms of the phase δ, Eq. 3.13 becomes

$$\Psi(x,t) = |\Psi(x,t)|\exp(i\delta(x,t)). \tag{3.14}$$

By combining the last two equations and setting $E = e^*V = 2eV$, one obtains

$$\partial_t\delta = \frac{2eV}{\hbar}, \tag{3.15}$$

which is the second Josephson Equation, i.e. voltage-phase relation.

3.2.2.2 Long Dayem bridges ($L > \xi$)

For several superconducting materials, where the coherence length is too short [7], the fabrication of typical junctions with a weak link with $L > \xi$ is technically challenging. The purpose of this subsection is to introduce a quantitative description for a weak link device with a long bridge with $L > \xi$ based on the GL equation. Here several numerical methods for GL equation are briefly presented.

Finite element method (FEM) calculations

Hasselbach *et el* [8] have used this method to model superconducting quantum interference devices (SQUIDs) by solving the GL equations to obtain the supercurrent–phase relationships. Staring from the wave function Ψ written as the complex order parameter $\Psi = |\Psi|\exp(i\varphi)$ and substitute it in the 2D form of Eq. 3.3, and by separating the real and imaginary parts of this equations, one gets

$$\begin{aligned}\alpha|\Psi| + \beta|\Psi|^3 - \frac{\hbar^2}{2m}\left[\frac{d^2|\Psi|}{dx^2} - |\Psi|\left(\frac{d\varphi}{dx}\right)^2\right.\\ \left. - \frac{\hbar^2}{2m}\left[\frac{d^2|\Psi|}{dy^2} - |\Psi|\left(\frac{d\varphi}{dy}\right)^2\right] = 0,\right.\end{aligned} \tag{3.16}$$

and

$$2\frac{d\varphi}{dx}\frac{d|\Psi|}{dx} + |\Psi|\frac{d^2\varphi}{dx^2} + 2\frac{d\varphi}{dy}\frac{d|\Psi|}{dy} + |\Psi|\frac{d^2\varphi}{dy^2} = 0. \tag{3.17}$$

By defining the wavefunction as $\Psi(x,y) = |\Psi_0|f(x,y)$, and using reduced units in which $x' = x/\xi(T)$ and $y' = y/\xi(T)$, Eq. 3.16 becomes

$$\frac{d^2f}{dx'^2} - f\frac{d^2\varphi}{dx'^2} + \frac{d^2f}{dy'^2} - f\frac{d^2\varphi}{dy'^2} + f - f^3 = 0, \tag{3.18}$$

and Eq. 3.17 becomes

$$2\frac{df}{dx'}\frac{d\varphi}{dx'} + f\frac{d^2\varphi}{dx'^2} + 2\frac{df}{dy'}\frac{d\varphi}{dy'} + f\frac{d^2\varphi}{dy'^2} = 0. \tag{3.19}$$

And the supercurrent density J_s can be written in terms of f and φ as

$$\mathbf{J}_s = \frac{e^*\hbar}{2m\xi(T)}|\Psi_0|^2 f^2\left(\hat{\mathbf{i}}\frac{d\varphi}{dx'} + \hat{\mathbf{j}}\frac{d\varphi}{dy'}\right). \tag{3.20}$$

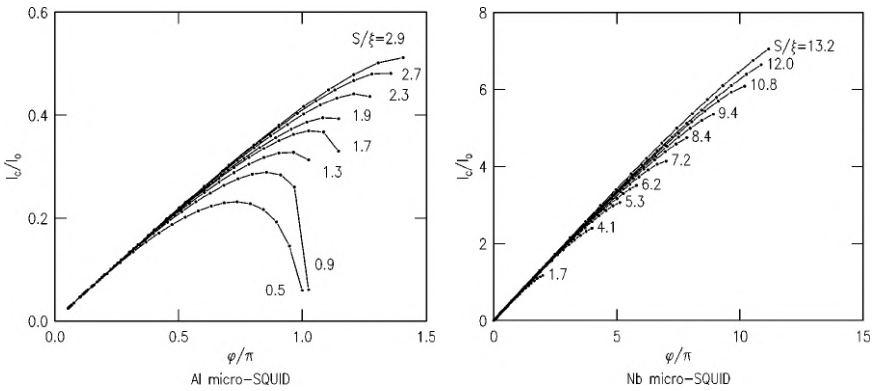

Figure 3.3: Current–phase relationship as numerically calculated for different values of weak link length which was obtained for AL and Nb. S refers to the length of the bridge. Adapted from Hasselbach.

By discretizing the last three differential equations with discrete steps δ using the finite element method (FEM), one gets the following expression for Eq. 3.18

$$\begin{aligned} &f_{i+1,j} + f_{i-1,j} + f_{i,j+1} + f_{i,j-1} \\ &+ \left[4 - (\varphi_{i+1,j} - \varphi_{i,j})^2 - (\varphi_{i,j+1} - \varphi_{i,j})^2 + \delta^2\right] f_{i,j} = \delta^2 f_{i,j}^3, \end{aligned} \tag{3.21}$$

and Eq. 3.19 yields

$$\begin{aligned} &\varphi_{i+1,j}\left[f_{i,j} + 2(f_{i+1,j} - f_{i,j})\right] + f_{i,j}\varphi_{i-1,j} + \\ &\varphi_{i,j+1}\left[f_{i,j} + 2(f_{i,j+1} - f_{i,j})\right] + f_{i,j}\varphi_{i,j-1} + \\ &\varphi_{i,j}\left[-4f_{i,j} - 2(f_{i+1,j} - f_{i,j}) - 2(f_{i,j+1} - f_{i,j})\right] = 0, \end{aligned} \tag{3.22}$$

and the total current through the junction can be written as:

$$I = I_c \sum_{j=1} f_{i,j}^2 \big(\varphi_{i+1,j} - \varphi_{i,j}\big). \tag{3.23}$$

The last three equations can be reduced to 1D. This gives

$$f_{i+1} + f_{i-1} + \left[2 - (\theta_{i+1} - \theta_i)^2 + \delta^2\right] f_{i+1} = \delta^2 f_i^3, \tag{3.24}$$

$$\varphi_{i+1}\big[f_i + 2(f_{i+1} - f_i)\big] + f_i\varphi_{i-1} + \varphi_i\big[-4f_i - 2(f_{i+1} - f_i)\big] = 0, \tag{3.25}$$

and

$$I = I_c f_i^2\big(\varphi_{i+1} - \varphi_i\big). \tag{3.26}$$

The last three equations have been self-consistently solved, and the results are shown in Fig. 3.4 which shows sinusoidal current–phase relationship when $L \ll \xi$

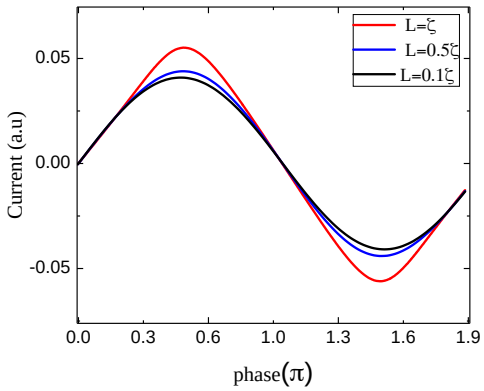

Figure 3.4: Current–phase relationship as numerically calculated from the reduced 1D GL equation at different values of bridge length. As the bridge becomes shorter the relationship becomes more sinusoidal.

Numerical integration method

In this method [9] GL equation was employed to study nano-Dayem bridges having dimensions (length L and/or width W) greater than coherence length of the superconducting film. The approach presented here has been followed in several studies such as [10, 11, 12]. By transforming the GL equation to the integral form, one obtains two equations describing the behaviour of the critical current in terms of the phase difference across the Dayem bridge, and the ratio L/ξ. These equations are:

$$\frac{L}{\xi} = 2\int_{a_0}^{1} \frac{da}{|\sqrt{a_0^2 + \frac{a_0^4}{2} + \frac{j_0^2}{a_0^2} - a(x)^2 + \frac{a(x)^4}{2} + \frac{j(x)^4}{2}}|}, \tag{3.27}$$

$$\varphi = 2j_0\xi\int_{a_0}^{1} \frac{da}{a(x)^2|\sqrt{a_0^2 + \frac{a_0^4}{2} + \frac{j_0^2}{a_0^2} - a(x)^2 + \frac{a(x)^4}{2} + \frac{j(x)^4}{2}}|}, \tag{3.28}$$

where the function $a(x)$ satisfies [12] the relations, $a(0) = a(L) = 1$, and $a(x) < 1$ in the region of the nanobridge. Furthermore, it has minimum a_0 at the center of the bridge. The parameters j_0 and φ are the scaled current density and the phase difference across the bridge respectively. Scalar nonlinear zero finding function was used [9] to find j_0 values

by varying the a_0 parameter in Eq. 3.27. The pairs then (a_0, j_0) are substituted in Eq. 3.28 to find the corresponding phase values. In such a way, the pairs (φ, j_0) have been calculated [9] to obtain the current-phase curve at different values of $P_{L/\xi(\varphi)}$. The results as obtained in [9] are presented in Fig. 3.5. In this figure the current values are normalized to the supercurrent values (I_s). The figure shows a sinusoidal behaviour when the length of the bridge is equal to the coherence length. However, this behaviour is deformed by increasing the ratio L/ξ. The critical current I_0 was also calculated at different L/ξ values and plotted in the inset of Fig. 3.5, in which $I_0(L/\xi)$ behaviour shows an exponential-like decay as $L \leq \xi$ at which the critical current density of an infinitely long superconducting wire is depaired [13].

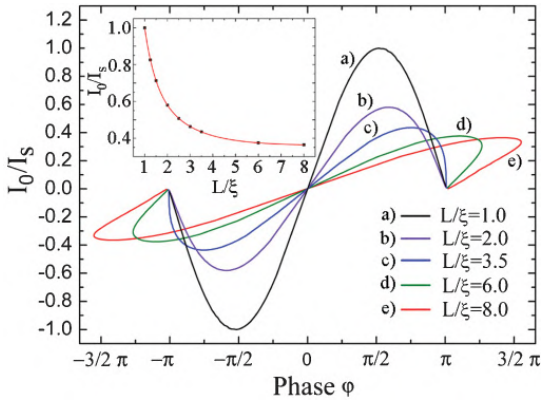

Figure 3.5: Current-phase relationship at different values of L/ξ. The inset shows the normalized critical current I_0 as a function of theL/ξ ratio. Adapted from [9].

3.2.3 Josephson effect in point contacts

So far weak links with relatively short and long bridges have been highlighted. Here three types of junctions are dissuaded: (i) Aslamazov-Larkin model, (ii) Kulik-Omelyanchuk model, dirty limit (KO-1), and (iii) Kulik-Omelyanchuk model, clean limit (KO-2).

3.2.3.1 Aslamazov-Larkin model

In the Aslamazov-Larkin model [13, 14] the Josephson coupling occurs due to an overlap of superconducting wavefunctions of both electrodes in the weak-link region. Two conditions to be satisfied in this model: (i) the temperature is near T_c, and (ii) the effective length of the weal-link is much smaller than the coherence length ($L_{eff} << \xi$). These conditions lead to the following results for the current phase relationship:

$$I_S = \frac{\pi \Delta_1 \Delta_2}{4 e R_N T} \sin(\varphi), \tag{3.29}$$

Where $\Delta_{1,2}$ are the magnitudes of the pair potentials in the superconducting electrodes, and R_N is the normal state resistance of the weak link. The Boltzmann constant K_B in Eq. 3.29 is set to be 1.

3.2.3.2 Kulik-Omelyanchuk model, dirty limit (KO-1)

In the dirty limit where electron mean free path is much shorter than the superconducting coherence length ξ_0. A quantitative description for the critical current has been derived by Kulik and Omelyanchuk known as (KO1) [15]. Point contact as a diffusive quasi 1D wire has been considered in this model, where conditions to be satisfied are: the length $L \ll \sqrt{\xi_0 \ell}$ with transverse size $a \ll L$, where $\xi_0 = \hbar v_F / 2\pi T_c$, and $\ell \ll \xi_0$ is the electronic mean free path. If the junction consists of identical superconductor electrodes, then the current phase relationship is given by:

$$I_S(\varphi) = \frac{4\pi T}{eR_N} \sum_{\omega_n > 0} \frac{\Delta \cos(\varphi/2)}{\delta} \arctan\left(\frac{\Delta \sin(\varphi/2)}{\delta}\right), \tag{3.30}$$

with $\delta = \sqrt{\Delta^2 \cos^2(\varphi/2) + \omega_n^2}$, and $\omega_n = \pi T(2n+1)$ is the Matsubara frequency. Numerical calculations for the current phase relationship given Eq. 3.30 is presented in Fig. 3.6.

A general case for KO1 model can be considered [16] when the superconductor electrodes are not identical with the pair potentials $\Delta_{1,2}$. Here the current phase relationship is given by:

$$I_S(\varphi) = \frac{\Delta_1}{eR_N} \left[\ln\left(\frac{2\Delta_2}{\Delta_1[1+\cos(\varphi)]}\right)\right] \sin(\varphi) \tag{3.31}$$

3.2.3.3 Kulik-Omelyanchuk model, clean limit (KO-2)

A clean point contact is a constriction with a size in both transversal and longitudinal directions are shorter than the electronic mean free path. Kulik and Omelyanchuk [17] have presented a theory known as KO-2 model to describe the Josephson effect in the fully ballistic case, where the diffusive parameter $D = 1$. The calculations performed in this model were based on the Eilenberger equations [18]. Here the details of these calculations are not given. However, the final expression for the current phase relationship is given by

$$I_S(\varphi) = \frac{\pi \Delta}{eR_N} \sin(\varphi/2) \tanh\left[\frac{\Delta \cos(\varphi/2)}{2T}\right], \tag{3.32}$$

with the Sharvin resistance $R_N^{-1} = \frac{e^2 k_F^2 S}{4\pi^2 \hbar}$, where k_F is the Fermi wave vector, and S is the constriction area. It's important to refer that the conductance of a ballistic point contact is quantized [19] with $G = \frac{ne^2}{h}$. At zero temperature, theoretical studies [20, 21] show that the critical current of impurity-free superconducting constriction increases stepwise as a function of its width, with step $e\Delta/\hbar$. With this result, Eq. 3.32 can be extended with the quantum resistance $R_N^{-1} = \frac{e^2}{\pi\hbar}$, where N is the open channels. Thus, Eq. 3.32 becomes

$$I_S(\varphi) = N \frac{e\Delta}{\hbar} \sin(\varphi/2) \tanh\left[\frac{\Delta \cos(\varphi/2)}{2T}\right], \tag{3.33}$$

Experimentally, the quantizes supercurrent at different junction width has been observed [22] in ballistic S/2DEG/S structures.

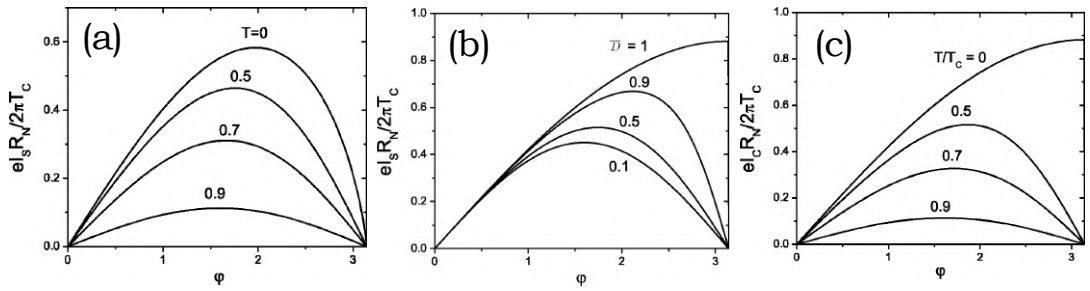

Figure 3.6: Current-phase relations for (a) a symmetric diffusive point contact according the Kulik-Omelyanchuk (KO-1) model at various normalized temperatures T/T_c, (b) a clean point contact at $T = 0$ and various values of transmission probability $\overline{D}$, (c) a clean point contact for $D = 1$ and various temperatures. Adapted from [23].

3.2.3.4 The general case of the point contact: arbitrary transparency

More general case for KO results with arbitrary transparency have been obtained in Ref [24] by solving Gor'kov equations [25]. This leads to following current phase relationship

$$I_S(\varphi) = \frac{\pi\Delta}{2eR_N} \frac{\sin\varphi}{\sqrt{1-\overline{D}\sin^2(\varphi/2)}} \tanh\left(\frac{\Delta}{2T}\sqrt{1-\overline{D}\sin^2(\varphi/2)}\right), \tag{3.34}$$

where $\overline{D}$ is the averaged transmission probability, and contact resistance $R_N^{-1} = \frac{e^2k_F^2S}{4\pi^2\hbar}\overline{D}$. Results for Eq. 3.34 are given in Fig. 3.6 (b) and (c) for the current phase relationship at different values of $\overline{D}$ and T.

3.2.3.5 Quasiparticle theory: arbitrary geometries

Structures with arbitrary geometries were achieved by Gor'kov, Eilenberger, and Usadel [18, 25, 26] using Green's function. Here, a general description for the results obtained using Usadel's equation are briefly presented. For this purpose, calculations based on Usdal's equations were adapted from Ref [27, 28], where weak links with Dayem bridges of different thickness, length and width have been considered to obtain the current phase relationships. The Usadel equations for superconductors in terms of the Green's function and the diffusion constant, are given by

$$\omega F_\omega(\mathbf{r}) + \frac{D}{2}\left(F_\omega\nabla^2 G_\omega - G_\omega\nabla^2 F_\omega\right) = \Delta^* G_\omega(\mathbf{r}), \tag{3.35}$$

where Δ is complex quantity which is analogous to the superconducting order parameter that reduced to the ordinary gap Δ_0 a spatially homogeneous superconductor. The

ordinary gap Δ_0 is given in terms of the Matsubara frequencies ω_n as

$$\omega_n = (2n+1)\pi \frac{T}{\Delta_0}. \tag{3.36}$$

If the phase drops from the left electrode to the right in the weak link, the gradient terms of Eq. 3.35 becomes the dominating one. An analytical solution for such case leads to the results obtained by Kulik-Omelyanchuk (KO-1).

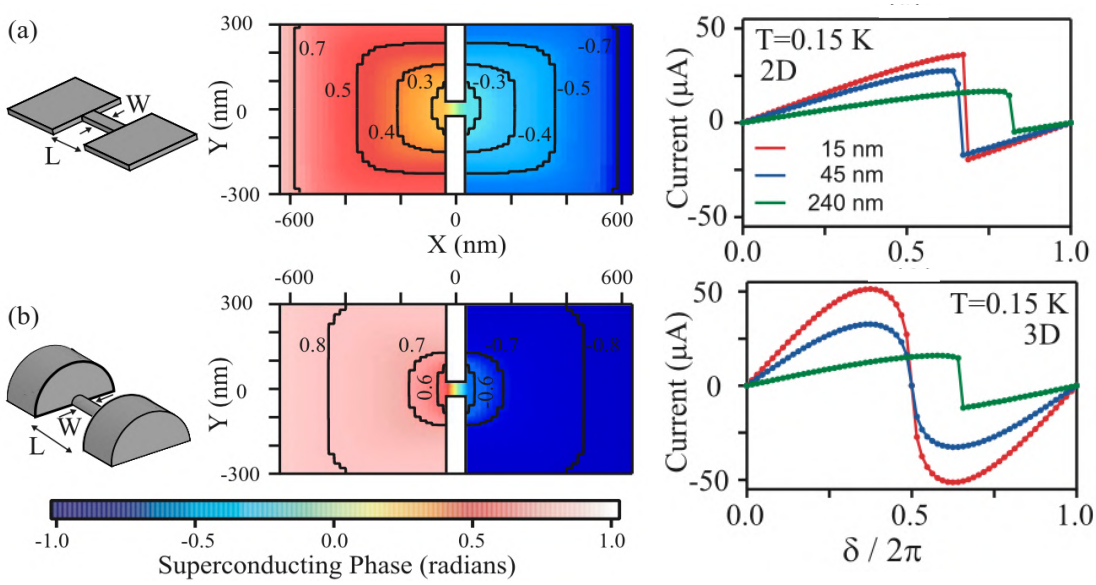

Figure 3.7: (Left: top and bottom) 2D and 3D nanobridge geometries used for simulations presented in Ref [27, 28], with $L = 75$ nm, $W = 45$ nm, and lateral dimensions of 600×300 nm. Here, the lateral dimensions are both for the 2D and 3D banks. The results of the phase evolution across the 2D and 3D junctions are presented in the middle (top and bottom). Right (top and bottom): the calculated current phase relations for Al nanobridge with width $W = 45$ nm at different lengths $L = 15$, 45, and 240 nm, and $T = 0.15$ K. The structures were assumed to be made of Al with $\xi_0 \approx 30$ nm, and $T_c = 1.2$ K.

To numerically solve the Usadel equations for 2D and 3D structures, the Gorkov-Nambu formalism [25, 23] was used in Ref [28], where the superconducting gap and phase have modulated following the parametrization of the Usadel equations given in Ref [23]. In this parametrization F and G in Eq. 3.35 have been introduced by a new function Φ, which reads for a bulk superconductor $\Phi = \Delta$, and satisfies the condition: $F_\omega^2 + G_\omega^2 = 1$, where F_ω and G_ω are given in terms of Φ as:

$$F_\omega = \frac{\Phi}{\sqrt{\omega_n^2 + |\Phi|^2}}, \quad \text{and} \quad G_\omega = \frac{\omega_n}{\sqrt{\omega_n^2 + |\Phi|^2}}, \tag{3.37}$$

which leads to the following equation

$$g(\omega_n)\big[\Phi(\omega_n) - \Delta\big] = \frac{D_0}{2}\nabla\big[g(\omega_n)^2 \nabla\Phi(\omega_n\big], \tag{3.38}$$

with $g(\omega_n) = G_\omega/\omega_n$. The self-consistency equation is given by

$$\Delta = \frac{\sum_n g(\omega_n)\Phi(\omega_n)}{\sum_n(\omega_n^2+1)^{-1/2}}, \tag{3.39}$$

and the current density was calculated using

$$J(r) = \frac{\sigma}{e}\pi T \sum_\omega g(\omega_n)^2 \Im\big[\Phi^*(\omega_n)\partial_x\Phi(\omega)\big], \tag{3.40}$$

where $\Im$ stands for the imaginary part. To obtain the current density given in Eq. 3.40, the functions $g(\omega_n)$, $\Phi(\omega_n)$, and Δ are calculated by solving Eqs. 3.37-3.39, where the left and right boundaries were defined as $\Delta_R = \Delta_L \exp(-i\delta)$. With this condition the problem can be solved as a boundary value problem at different values of δ between 0 and 2π.

Fig. 3.7 shows the 2D and 3D junction geometries used for simulations presented in Ref [27, 28]. The structures are assumed to be made of Aluminium with coherence length $\xi \approx 30$ nm, and $T_c = 1.2$ K. The calculations have been performed with: $T = 0.15$ K, the dimensions of banks are 600×300 nm, the width of the Al nanobridge is $W = 45$ nm, and different length values between $L = 15$ and 240 nm. The results show that the behaviour of current phase relationship of the 3D structures is almost sinusoidal as $L < \xi$. However, it becomes linear when $L > \xi$. In contrast, the current phase relationship of the 2D structures shows a nearly linear behaviour for all selected bridge lengths.
Fig. 3.7 shows also simulations for phase evolution, where a total phase difference of 2 radians is imposed symmetrically across the bridge. In the 3D structure, most of the phase declines across the constriction, while significant phase change occurs in the banks of the the 2D structure.

3.3 The RCSJ model of a Josephson junction and qubits

3.3.1 The RCSJ model of a Josephson junction

Junction dynamics can be described by a model called "resistivity and capacitively shunted junction" (RCSJ) [29]. In this model an ideal Josephson junction with a sinusoidal current phase relationship, is shunted with a resistor and capacitor as shown in Fig. 3.8(a) in which the resistor R reflects the normal state resistance of the junction, and the capacitance between the two superconducting electrodes is C. The dynamics of the system can be described by considering a current I_b flowing through a circuit such that shown in Fig. 3.8(a). This is given by

$$I_b = I_c \sin(\delta) + \frac{V}{R} + C\frac{dV}{dt}, \tag{3.41}$$

where V is the voltage drop across the circuit that is given in terms of δ by

$$\frac{d\delta}{dt} = \frac{\hbar}{2e} V(t). \tag{3.42}$$

By combining that last two equations, the phase difference can be written as

$$\frac{d^2\delta}{dt^2} + \frac{1}{\omega_p RC}\frac{d\delta}{dt} + \sin(\delta) = \frac{I_b}{I_c} \tag{3.43}$$

where $\omega_p = \left(\frac{\Phi_0}{2\pi}\frac{I_0}{C}\right)^{1/2}$ is the plasma frequency of the junction. The behaviour given in the last differential equation is similar to the equation of motion of a particle with a mass $C\left(\frac{\hbar}{2e}\right)^2$ moving a washboard potential given by

$$U(\delta) = \frac{\Phi_0}{2\pi}\Big[I_0[1-\cos(\delta)] - i\delta\Big] = E_J\big[1-\cos(\delta) - i\delta\big], \tag{3.44}$$

where E_J is the junction coupling energy, and $i = I_b/I_0$. Fig. 3.8(b) shows washboard potential for a junction biased with $I_b = 0.5I_0$, and $0.9I_0$. When the currents is less than the critical current, the potential is tilted in such a way that the particle is trapped in a potential well within the washboard potential, in which the particle oscillates inside it at the plasma frequency. The well potential is determined by

$$\Delta U = -\frac{\Phi_0}{2\pi} I_0 \left[\sqrt{1 - \frac{I_B^2}{I_0}} - \frac{I_B}{I_0}\cos\left(\frac{I_B}{I_0}\right)\right]. \tag{3.45}$$

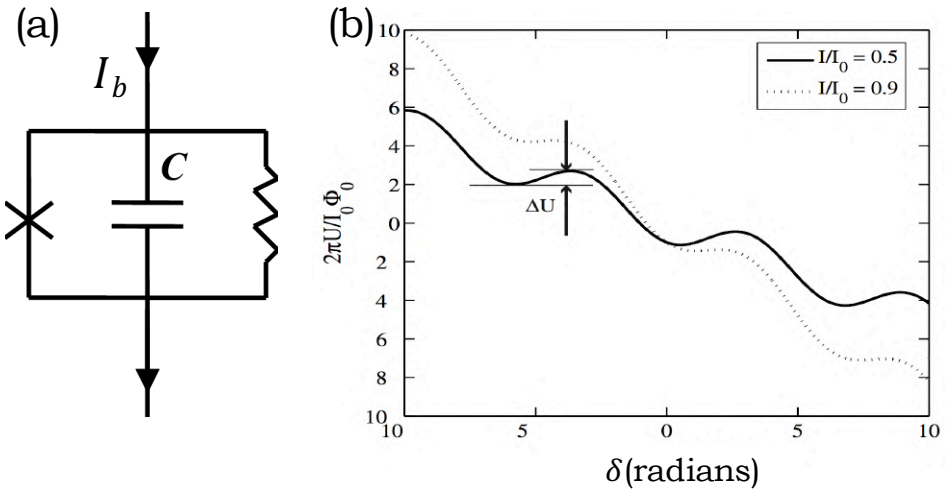

Figure 3.8: (a) A schematic illustration for the RCSJ model. (b) The washboard potential for Josephson junction with $I_b = 0.5I_0$, and $0.9I_0$.

3.3.2 I(V) Characteristics of Josephson junction based on RCSJ model

$I(V)$ characteristics can be calculated for Josephson junction by solving the coupled differential equations given by Eqs. 3.42, and 3.43. These equations can be numerically solved to obtain the time dependent voltage variation for given bias values, critical current, resistance and capacitance. Numerically, this can be performed using 4th order Runge-Kutta method (RK4). A full $I(V)$ characteristics can be obtained by repeating the calculations for the average of the time dependent voltage at different values of the bias current. It should be noted here that Runge-Kutta method requires transforming all second differential equations to first order. Details of such technical analyses are given in Sec. 3.4.

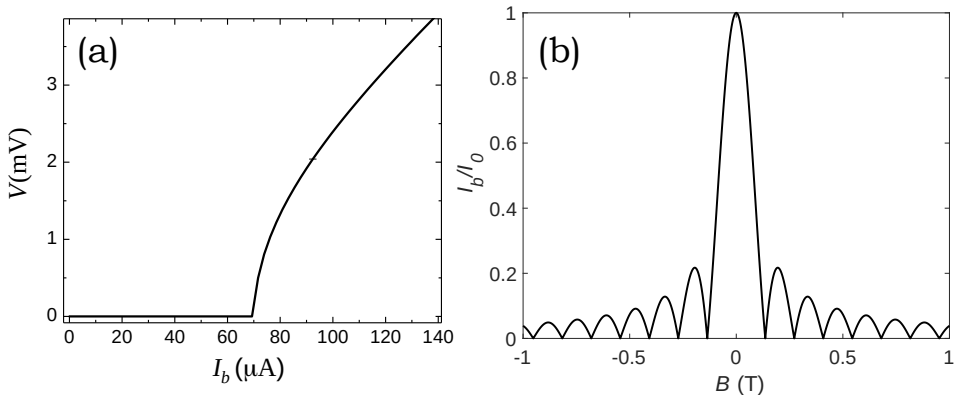

Figure 3.9: (a) $I(V)$ characteristics was calculated using the following parameters: $R_N = 30\Omega$, $I_0 = 70$ A, and $C = 1$pF, and (b) Fraunhofer diffraction pattern that describes the critical current dependence on magnetic field.

In Fig 3.9(a) the $I(V)$ characteristics was calculated using the following parameters: $R_N = 30\Omega$, $I_0 = 70$ A, and $C = 1$pF. Here, the calculated $I(V)$ characteristic are obtained in the absence of the magnetic field. However, in the presence of magnetic field the critical current is modified I_c as

$$I_c = \left| \frac{\sin\left(\frac{\pi\Phi}{\Phi_0}\right)}{\frac{\pi\Phi}{\Phi_0}} \right|, \tag{3.46}$$

The result of the critical current given in the last equation exhibits a diffraction pattern known Fraunhofer diffraction pattern shown by Fig 3.9(b).

3.3.3 Ambegaokar and Baratoff formula for SIS tunnel junctions

Let's consider two superconductors separated by a thin insulating barrier such superconductor/insulator/superconductor (SIS) junctions are shown in Fig 3.10, where the two superconductors are with states filled to a certain level, offset by the energy eV, where

V is the externally applied bias voltage is depicted in Fig 3.10(a). For SIS junctions, the tunnel current is given by the expression:

$$I(V) = \frac{1}{eR_n}\int_{-\infty}^{\infty} \frac{|E|}{(E^2-\Delta_1^2)^{1/2}} \frac{|E+eV|}{[(E+eV)^2-\Delta_2^2]^{1/2}} [f(E)-f(E+eV)]dE, \tag{3.47}$$

the integral is assumed to exclude values of E, where $|E| < \Delta_1$ and $|E+eV| < \Delta_2$. By fowling the $I-V$ characteristics along the voltage axis, a current rise to V/R_n when we reach a bias potential $V = (\Delta_1+\Delta_2)/e$, where R_n is the normal tunnel resistance. At finite temperature, an increase in current will also be observed at a bias voltage of $V = |\Delta_1+\Delta_2|/e$. Josephson effects can also be observed in weak-link systems where a nanoscale-size superconducting element connects macroscopic-scale superconductors, as with a so-called point contact. In general, The critical current is given in by Ambegaokar and Baratoff formula [30] as

$$I_c R_n = \frac{\pi[\Delta_1(T)+\Delta_2(T)]}{4e} \tanh \frac{\Delta_1(T)+\Delta_2(T)}{4k_B T}, \tag{3.48}$$

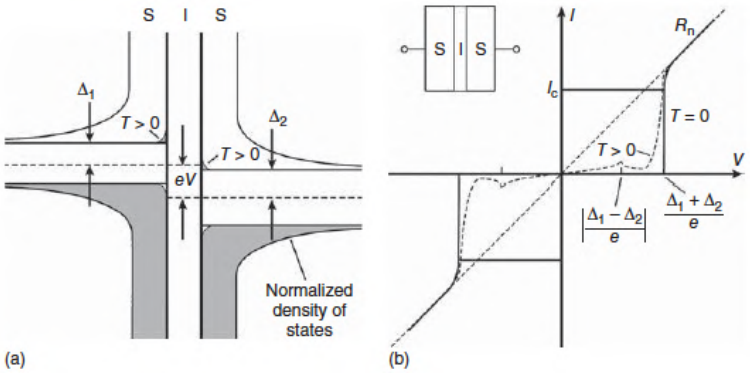

Figure 3.10: (a) Density of states for a superconductor/insulator/superconductor (SIS) tunnel junction. (b) Current–voltage characteristics for an SIS tunnel junction. Adapted from [31].

3.3.4 Hamiltonian of a Josephson junction and qubits

One of the future goals of the project of this thesis, is to produce a quantum processor containing a qubit coupled to a nanomechanical resonator. Such systems should enable a fully quantum measurement of a single phonon mode and allow quantum manipulation of qubits. Many types of qubits such as superconducting devices with Josephson junctions or weak links, can be used to construct three main classes of qubits: charge, phase and flux qubits. This subsection is a brief overview for the theoretical aspects of the Josephson junction qubit.

In Sec. 3.3.1, the equation of motion for the phase difference of a Josephson junction was given in Eq. 3.43, which is identical to the equation of motion of a damped driven pendulum with the angular displacement δ. In the pendulum analogue, the current I_b corresponds to a torque, the capacitance term $\frac{\phi_0}{2\pi}C$ is the moment of inertia of the pendulum,

and the resistance term $\frac{\phi_0}{2\pi}\frac{1}{R}$ corresponds to the damping [32, 33, 34]. The Lagrangian for a Josephson junction satisfies the following equation

$$\frac{d}{dt}\frac{\partial \mathcal{L}}{\partial \dot{\delta}} - \frac{\partial \mathcal{L}}{\partial \delta} = 0, \tag{3.49}$$

and the Hamiltonian follows

$$\mathcal{H}(p_\delta, p_{\dot{\delta}}) = p_\delta \dot{\delta} - \mathcal{L}(p_\delta, p_{\dot{\delta}}), \tag{3.50}$$

where

$$p_{\dot{\delta}} = \frac{\partial \mathcal{L}}{\partial \dot{\delta}} \left(\frac{\Phi_0}{2\pi}\right)^2 C\dot{\delta}, \tag{3.51}$$

by ignoring the dissipation, and comparing the last three equations, the Hamiltonian reads:

$$\mathcal{H} = \frac{1}{2C}\left(\frac{\Phi_0}{2\pi}\right)^2 p_\delta^2 - \left(\frac{I_0\Phi_0}{2\pi}\right)(I_0\cos\delta + \delta I_b), \tag{3.52}$$

The Hamiltonian given by Eq. 3.52 is used to solve the associated Schrodinger equation $\mathcal{H}\psi = E\psi$. The Schrodinger equation is solved and the solutions are plotted in Fig. 3.11 . Microwave spectroscopy experiments [35] performed on Josephson junctions indicated that the washboard potential given by Eq. 3.44 actually contains multiple quantised energy levels with a ground state defined by $E = \hbar\omega_p$ separated by approximately integer factors of the plasma frequency. Such quantisation means that the device can be used as a qubit, with the ground state $|0\rangle$, and the first excited state representing the first qubit state $|1\rangle$. As the bias current can be used to tune the washboard potential, the Hilbert space can be modified for quantum states of two level system.

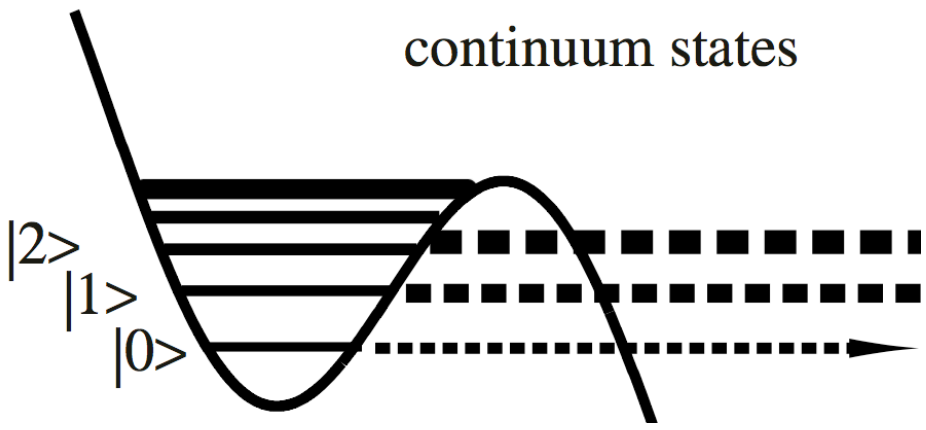

Figure 3.11: The quantum states obtained from solving the Schroedinger equation with the Hamiltonian given in Eq. 3.52 . Close to the top of the barrier, the energy levels form a continuous energy band.

3.4 Superconducting quantum interference devices (SQUID)

A superconducting quantum interference device (SQUID) consists of two Josephson junctions in a superconducting loop shown in Fig. 3.12(b). In the absence of external magnetic field, the bias current I_b splits the two equals parts. When a small external magnetic field is applied to the loop, a circulating current J emerges in the loop, and creates an additional Josephson phase which is proportional to this external magnetic flux. As the induced current is in the same direction as of I_b in one arm of the superconducting loop, and opposite to the I_b on the another arm of the loop, the currents I_1, and I_2 shown in Fig. 3.12(a) are: $I_b/2 + J$, and $I_b/2 - J$ respectively.

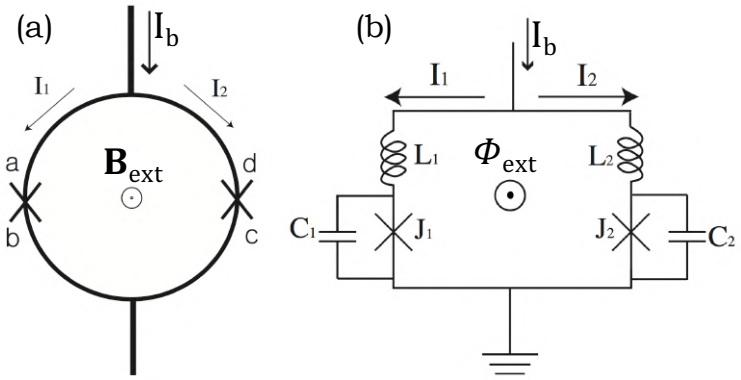

Figure 3.12: Schematic diagram of a dc SQUID loop which consists of two Josephson junctions. The bias current I_b splits into two parts $I_1 = I_b/2 + J$ and $I_2 = I_b/2 - J$, B_{ext} is the applied magnetic field. (b) Schematic of a dc SQUID in which J_1 and J_2 are the junctions, C_1 and C_2 are the junction capacitances, and L_1 and L_2 are the junction conductances, Φ_{ext} is the applied flux. Adapted from [36].

RCSJ model for dc SQUID shown in Fig. 3.12(b) is used to analysis the dynamic of the dc SQUID loop, where a dc SQUID is described by phase differences of the junctions involved in two coupled second order differential equations. A symmetric dc SQUID system yields:

$$\frac{\Phi_0}{2\pi} C \ddot{\delta_1} + \frac{\Phi_0}{2\pi} \frac{1}{R} \dot{\delta_1} + I_0 \sin(\delta_1) = \frac{1}{2} I_b + J, \tag{3.53}$$

$$\frac{\Phi_0}{2\pi} C \ddot{\delta_2} + \frac{\Phi_0}{2\pi} \frac{1}{R} \dot{\delta_2} + I_0 \sin(\delta_2) = \frac{1}{2} I_b - J, \tag{3.54}$$

and

$$\delta_1 - \delta_2 = 2\pi \frac{\Phi_{\text{tot}}}{\Phi_0}, \tag{3.55}$$

where $\delta_{1,2}$ are the phase differences of the junctions, $\Phi_0 = h/2e$ is the flux quantum, I_b is the bias current, I_0 is the critical current, and Φ_{tot} is the total magnetic flux which consists of two components: (i) the external flux Φ_{ext}, and (ii) the flux due to the circulating

current, J, flowing through the inductance of the loop, L. Therefore, $\Phi_{\text{tot}} = \Phi_{\text{ext}} + LJ$, and Eqs. 3.53 -3.55 are coupled via the circulating current as

$$J = \frac{1}{L}\left(\frac{\delta_1 - \delta_2}{2\pi}\Phi_0 - \Phi_{\text{ext}}\right). \tag{3.56}$$

Eqs. 3.53 - 3.55 can be rewritten in dimensionless form by introducing a new time interval:

$$\tau = \frac{2eI_0R}{\hbar}t. \tag{3.57}$$

Thus, the time derivatives $\dot{\delta_1}$, $\ddot{\delta_1}$, $\dot{\delta_2}$, and $\ddot{\delta_2}$ can be defined in terms of new variables using the chain rule:

$$\dot{\delta_1} = \frac{d\delta_1}{dt} = \frac{d\delta_1}{d\tau}\frac{d\tau}{dt} = \frac{2eI_0R}{\hbar}\frac{d\delta_1}{d\tau}, \tag{3.58}$$

$$\dot{\delta_2} = \frac{d\delta_2}{dt} = \frac{d\delta_2}{d\tau}\frac{d\tau}{dt} = \frac{2eI_0R}{\hbar}\frac{d\delta_2}{d\tau}, \tag{3.59}$$

and

$$\ddot{\delta_2} = \frac{2eI_0R}{\hbar}\frac{d^2\delta_1}{d\tau^2}, \tag{3.60}$$

$$\ddot{\delta_2} = \frac{2eI_0R}{\hbar}\frac{d^2\delta_2}{d\tau^2}. \tag{3.61}$$

With these variables, the scaled SQUID equations follow

$$\beta_c\ddot{\delta_1} + \dot{\delta_2} + \sin\delta_1 = \frac{1}{2}i_b + j, \tag{3.62}$$

$$\beta_c\ddot{\delta_2} + \dot{\delta_2} + \sin\delta_2 = \frac{1}{2}i_b - j, \tag{3.63}$$

$$\delta_1 - \delta_1 = 2\pi\left(\phi_{ext} + \frac{1}{2}\beta_L j\right). \tag{3.64}$$

Where β_c and β_L are the capacitance and the inductive screening parameters: $\beta_c = \frac{2\pi I_0R^2C}{\Phi_0}$ and $\beta_L = \frac{2I_0L}{\Phi_0}$. The bias current and circulating current are normalized using the critical current $i_b = \frac{I_b}{I_0}$, and the circulating current is normalised using $j = \frac{J}{I_0}$. Also, the flux is normalized using the flux quantum as $\phi_{ext} = \frac{\Phi_{ext}}{\Phi_0}$. The scaled time τ can be written in terms of the characteristic frequency, ω_c, as $\tau = \omega_c t$, with $\omega_c = \frac{2\pi I_0R}{\Phi_0}$. With this scaling, the normalized voltage is given as:

$$v = \frac{V}{I_0R} = \frac{\dot{\delta_1} + \dot{\delta_2}}{2}, \tag{3.65}$$

Using the analogy between the equation of motion of a particle in the tilt washboard potential and the motion of the phase difference of a Josephson junction, the β_c parameter implies: (i) when the junction capacitance and/or the resistance are large ($\beta_c \gg 1$), Josephson junctions are underdamped, and (ii) when the junction capacitance and/or the resistance are small ($\beta_c \ll 1$), Josephson junctions are overdamped.

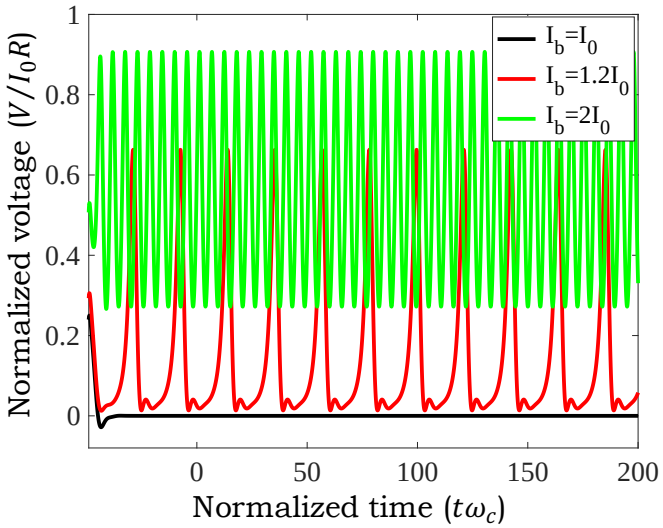

Figure 3.13: The time trace of the normalized voltage as calculated at different values of the bias current I_b and $\phi_{ext} = 0.5$.

The Runge–Kutta method (RK4) is used to numerically integrate the SQUID equations at different values of the bias current i_b, and for the flux ϕ_{ext}. To use such method, the coupled second order differential equations, Eq. 3.62, and 3.63 are transformed to the first order. This is performed by assuming $\dot{\delta_1} = p$, and $\dot{\delta_2} = q$. This results in the following coupled first order differential equations:

$$\dot{\delta_1} = p \tag{3.66}$$

$$\dot{p} = \frac{1}{\beta_c}\left(\frac{1}{2}i_b + j - p - \sin\delta_1\right), \tag{3.67}$$

$$\dot{\delta_2} = q, \tag{3.68}$$

$$\dot{p} = \frac{1}{\beta_c}\left(\frac{1}{2}i_b - j - q - \sin\delta_2\right). \tag{3.69}$$

The circulating current can be obtained from Eq. 3.64:

$$j = \frac{2}{\beta_L}\left(\delta_1 - \delta_2 - 2\pi\phi_{ext}\right). \tag{3.70}$$

By combining Eqs. 3.66 to 3.70, the SQUID equations read:

$$\dot{\delta_1} = p \tag{3.71}$$

$$\dot{p} = \frac{1}{\beta_c}\left(\frac{1}{2}i_b + \frac{2}{\beta_L}\left(\delta_1 - \delta_2 - 2\pi\phi_{ext}\right) - p - \sin\delta_1\right), \tag{3.72}$$

$$\dot{\delta_2} = q \tag{3.73}$$

$$\dot{q} = \frac{1}{\beta_c}\left(\frac{1}{2}i_b - \frac{2}{\beta_L}\left(\delta_1 - \delta_2 - 2\pi\phi_{ext}\right) - q - \sin\delta_2\right), \tag{3.74}$$

Here, the normalized voltage is given by

$$v = \frac{V}{I_0 R} = \frac{\dot{\delta_1} + \dot{\delta_1}}{2} = \frac{p+q}{2}. \tag{3.75}$$

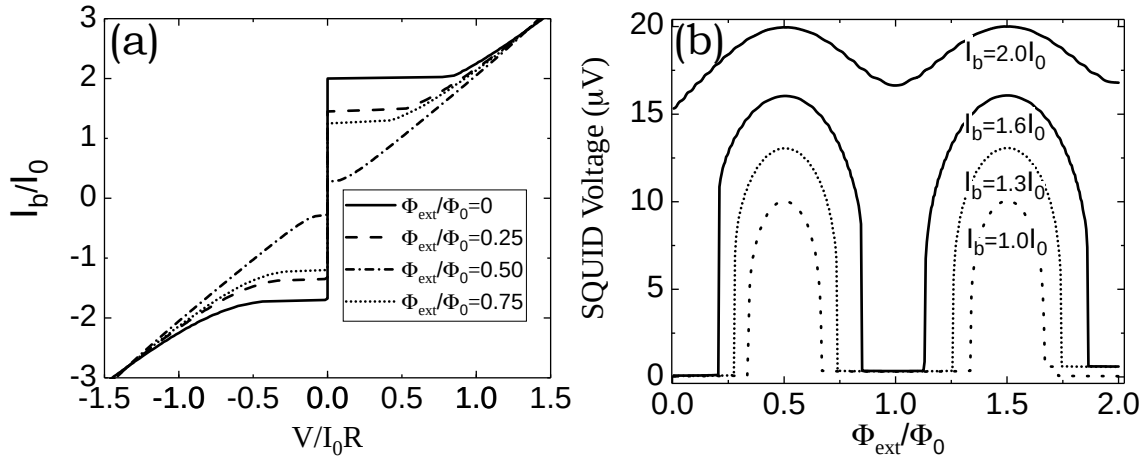

Figure 3.14: (a) Current voltage characteristics of dc SQUIDs at $I_0 = 0.7\text{A}$ and $R = 29.5\Omega$ which corresponds to $\beta_c = 1.6$, $\beta_L = 0.115$. (b) $V(\Phi)$ characteristics for a dc SQUID with $\beta_c = 1.6$, $\beta_L = 0.115$ and different values of I_b.

The time dependent voltage variation for values of the bias current is calculated and plotted in Fig. 3.13. To obtain $I(V)$ characteristics, the time average is performed to determine the steady state voltage across the junctions. The average of the voltage variation have been obtained at $I_0 = 0.7\text{A}$, and $R = 29.5\Omega$ which corresponds to $\beta_c = 1.61$, and $\beta_L = 0.115$, while the normalised external fluxes ϕ_{ext} were selected between zero and 0.75, the resulting $I(V)$ characteristic is plotted then in Fig. 3.14(a). The variation of the critical current that can be observed in Fig. 3.14(a) yields the Fraunhofer diffraction pattern described in Eq. 3.46. With the β_L and β_c values presented earlier, $V(\Phi)$ curves of an overdamped dc SQUID were calculated for bias current $1.0 \leq i_b \leq 2.0$, where the results are plotted in Fig. 3.14(b). As a SQUID is one of the most sensitive magnetometer

to measure extremely small magnetic fields, the sensitivity of a SQUID magnetometer depends on the position of the operating point in $V(\Phi)$ curves. This means that dc SQUID is most sensitive to changes in the magnetic flux by tuning it to a working point with a steep slope such that point appears at $I_b/I_0 = 2.0$, and $\Phi_{ext} = 0.25\Phi_0$. This will have a significant importance in Ch. 7, where a dc SQUID is used as a highly sensitive detector for the motion of a micromechanical cantilever embedded in a dc SQUID loop.

3.5 Granular superconductors and array of Josephson junctions

Disordered superconducting films which can be considered as a chain of identical mesoscopic superconducting grains can be modelled as arrays of Josephson junctions [37, 38, 39], which behave as a granular nanowire consisting of superconducting islands of various sizes and different coupling energies [40, 41, 42]. A network of Josephson junctions or 2D Josephson junction array which represents a granular superconductor can be studied in terms of RCSJ model [43]. This section is a brief overview for the such system as it can provide a deeper understanding for granular superconducting devices made of boron doped diamond.

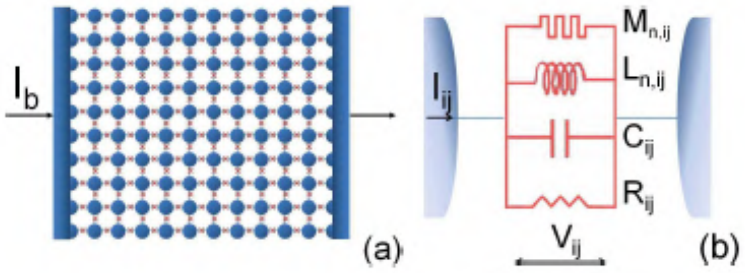

Figure 3.15: (a) A network of 2D Josephson junction array representing a granular superconductor, where the circles represent superconducting grains, and crosses represent weak-links between grains. (b) Equivalent circuit of the weak-link between the grains i and j based on the RSCJ model. Adapted from [43].

An illustration for 2D array of Josephson junctions is shown in Fig. 3.15(a), and the corresponding RCSJ model is shown in Fig. 3.15(b). A bias current I_b is applied to the left electrode illustrated in Fig. 3.15(a) in which circles represent superconducting grains connected by weak-links which are represented by crosses. Based on RCSJ model, the current I_{ij} flowing through each junction reads

$$I_{ij} = C_{ij}\frac{dV_{ij}}{dt} + \frac{V_{ij}}{R} + I_{0,ij}\delta_{ij}, \tag{3.76}$$

where C_{ij} and R_{ij} are the shunt capacitance and resistance between grains i and j, δ_{ij} is

the current phase relationship, and the voltage drop across the junction is given by

$$V_{ij} = V_i - V_j = \frac{\hbar}{2e}\frac{d\delta_{ij}}{dt}. \tag{3.77}$$

By solving the coupled differential equations given in the terms of the indexes i and j, the $I(V)$ characteristics along the array can be obtained. Although these calculations may provide an obvious picture for the superconducting devices made of granular boron doped diamond films, details about computational method to solve this system is not discussed in this thesis, and can be found elsewhere [44].

Bibliography

[1] Doll, Robert, and M. Näbauer. "Experimental proof of magnetic flux quantization in a superconducting ring." Physical Review Letters **7**.2 (1961): 51.

[2] Deaver Jr, Bascom S., and William M. Fairbank. "Experimental evidence for quantized flux in superconducting cylinders." Physical Review Letters **7**.2 (1961): 43.

[3] Josephson, Brian. "Possible new effect in superconducting tunneling." Phys. Lett. **1** (1962): 251-253.

[4] Josephson, BRIAN D. "The discovery of tunnelling supercurrents." Reviews of Modern Physics **46**.2 (1974): 251.

[5] Josephson, B. D. "The Discovery of Tunnelling Supercurrents-Nobel Lecture, 12 December 1973." Europhysics News **5**.3 (1974): 1-5.

[6] Mourachkine, Andrei. "Room-temperature superconductivity." Cambridge Int Science Publishing, 2004.

[7] Bustarret, Etienne, *et al.* "Dependence of the superconducting transition temperature on the doping level in single-crystalline diamond films." Physical review letters **93**.23 (2004): 237005.

[8] Hasselbach, K., D. Mailly, and J. R. Kirtley. "Micro-superconducting quantum interference device characteristics." Journal of applied physics **91**.7 (2002): 4432-4437.

[9] Granata, C., Vettoliere, A., Russo, M., Ruggiero, B. (2011). "Noise theory of dc nano-SQUIDs based on Dayem nanobridges." Physical Review B, **84**.22, 224516.

[10] Lam, S. K. H., and D. L. Tilbrook. "Development of a niobium nanosuperconducting quantum interference device for the detection of small spin populations." Applied physics letters **82**.7 (2003): 1078-1080.

[11] Troeman, Aico GP, *et al.* "NanoSQUIDs based on niobium constrictions." Nano Letters **7**.7 (2007): 2152-2156.

[12] Podd, G. J., *et al.* "Micro-SQUIDs with controllable asymmetry via hot-phonon controlled junctions." Physical Review B **75**.13 (2007): 134501.

[13] Likharev, K. K. "Superconducting weak links." Reviews of Modern Physics **51**.1 (1979): 101.

[14] Aslamazov, L. G., and A. I. Larkin. "Fiz. tverdogo Tela 10 (1968) 1104. translation." Soviet Physics-Solid State **10** (1968): 875.

[15] Kulik, I. O., and A. N. Omel'Yanchuk. "Contribution to the microscopic theory of the Josephson effect in superconducting bridges". Physico-technical Institute of Low Temperatures, Ukrainian Academy of Sciences, 1975.

[16] Zubkov, A. A., M. Yu Kupriyanov, and VK SEMYONOV. "STEADY-STATE PROPERTIES OF THE JOSEPHSON JUNCTION WITH DIRECT CONDUCTION." FIZIKA NIZKIKH TEMPERATUR **7**.11 (1981): 1365-1371.

[17] Kulik, I. O., and A. N. Omel'Yanchuk. "Properties of superconducting microbridges in the pure limit." Sov. J. Low Temp. Phys.(Engl. Transl.);(United States) **3**.7 (1977).

[18] Eilenberger, Gert. "Transformation of Gorkov's equation for type II superconductors into transport-like equations." Zeitschrift für Physik A Hadrons and nuclei **214**.2 (1968): 195-213.

[19] Beenakker, C. W. J., and Henk van Houten. "Quantum transport in semiconductor nanostructures." Solid state physics. Vol. **44**. Academic press, 1991. 1-228.

[20] Beenakker, C. W. J., and H. Van Houten. "Josephson current through a superconducting quantum point contact shorter than the coherence length." Physical review letters **66**.23 (1991): 3056.

[21] Furusaki, A., and M. Tsukada. "Physica (Amsterdam) 165B–166B, 967 (1990)." Phys. Rev. B **43**.10 (1991): 164.

[22] Takayanagi, Hideaki, Tatsushi Akazaki, and Junsaku Nitta. "Observation of maximum supercurrent quantization in a superconducting quantum point contact." Physical review letters **75**.19 (1995): 3533.

[23] Golubov, Alexandre Avraamovitch, M. Yu Kupriyanov, and E. Il'Ichev. "The current-phase relation in Josephson junctions." Reviews of modern physics **76**.2 (2004): 411.

[24] Haberkorn, W., H. Knauer, and J. Richter. Phys. Status Solidi A **47**. K161 (1978).

[25] Gor'kov, L. P. Zh. eksp. teor. Fiz., 34, 735. Sov. Phys. JETP **7**.505 (1958): 1959.

[26] Usadel, Klaus D. "Generalized diffusion equation for superconducting alloys." Physical Review Letters **25**.8 (1970): 507.

[27] Vijay, R., *et al.* "Optimizing anharmonicity in nanoscale weak link Josephson junction oscillators." Physical review letters **103**.8 (2009): 087003.

[28] Levenson-Falk, Eli Markus. "Static and Microwave Transport Properties of Aluminum Nanobridge Josephson Junctions." Diss. UC Berkeley, 2013.

[29] Clarke, John, and Alex I. Braginski, eds. "The SQUID handbook: Applications of SQUIDs and SQUID systems." John Wiley Sons, 2006.

[30] Ambegaokar, Vinay, and Alexis Baratoff. "Tunneling between superconductors." Physical Review Letters **10**.11 (1963): 486.

[31] Seidel, Paul, ed. "Applied superconductivity: handbook on devices and applications." John Wiley Sons, 2015.

[32] Orlando, Terry P., and Kevin A. Delin. "Foundations of applied superconductivity." Vol. **8**. Reading, MA: Addison-Wesley, 1991.

[33] Dutta, Sudeep Kumar. "Characterization of Josephson devices for use in quantum computation." Diss. 2006.

[34] Sullivan, D. B., and J. E. Zimmerman. "Mechanical analogs of time dependent Josephson phenomena." American Journal of Physics **39**.12 (1971): 1504-1517.

[35] Martinis, John M., Michel H. Devoret, and John Clarke. "Energy-level quantization in the zero-voltage state of a current-biased Josephson junction." Physical review letters **55**.15 (1985): 1543.

[36] Paik, Hanhee. "Coherence in dc SQUID phase qubits." University of Maryland, College Park, 2007.

[37] Chakravarty, Sudip, *et al.* "Onset of global phase coherence in Josephson-junction arrays: a dissipative phase transition." Physical review letters **56**.21 (1986): 2303.

[38] Fisher, Matthew PA. "Quantum phase slips and superconductivity in granular films." Physical review letters **57**.7 (1986): 885.

[39] Chakravarty, Sudip, *et al.* "Quantum statistical mechanics of an array of resistively shunted Josephson junctions." Physical Review B **37**.7 (1988): 3283.

[40] Langer, James S., and Vinay Ambegaokar. "Intrinsic resistive transition in narrow superconducting channels." Physical Review **164**.2 (1967): 498.

[41] Giordano, N. "Evidence for macroscopic quantum tunneling in one-dimensional superconductors." Physical review letters **61**.18 (1988): 2137.

[42] Bezryadin, Alexey, C. N. Lau, and M. Tinkham. "Quantum suppression of superconductivity in ultrathin nanowires." Nature **404**.6781 (2000): 971-974.

[43] Carbone, Anna, *et al.* "Array of Josephson junctions with a nonsinusoidal current-phase relation as a model of the resistive transition of unconventional superconductors." Journal of Applied Physics **108**.12 (2010): 123916.

[44] Forsman, Alexander, and Per Anders Thorén. "AC Behaviour of Josephson Junctions in Series." (2011).

4 Microwave Powder Filters

4.1 Motivation

Experiments on superconducting devices are being influenced by a considerable amount of noise such as radio frequency (RF) noise which is a result of electrical connections acting as antennas. To demonstrate the impact of such noise on the experimental results, measurements for $I(V)$ characteristics of a superconducting device made of nanocrystalline boron doped diamond were performed [1]. As shown in Fig. 4.1, $I(V)$ curves were measured with and without RF filter. A comparison between the unfiltered measurement and the one measured with the RF filter, shows a significant impact of the RF filter in improving the quality of the measurements. The impact of the filter can be clearly observed as the filtered measurement shows a typical $I(V)$ characteristics.

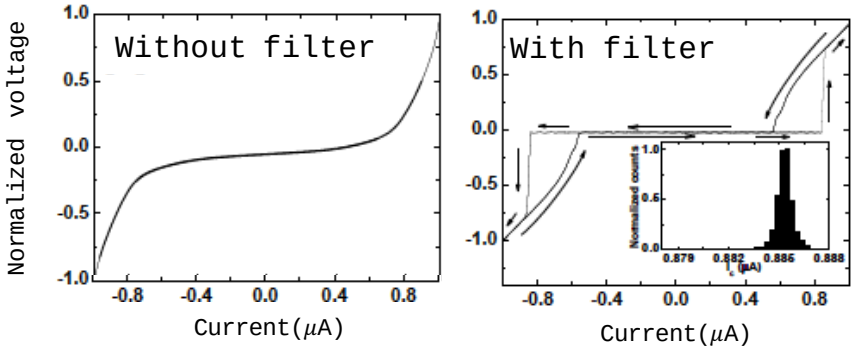

Figure 4.1: $I(V)$ characteristic of a nanostructured diamond superconducting device measured with and without RF filter. The inset shows the normalized histogram of the critical current, I_c. Adapted from [1].

In term of attenuation and the purposes for which the filters are fabricated, the filters can be classified to three different categories: (i) a low- pass filter (LPF) passes signals with a frequency lower than a selected cut off frequency f_c and attenuates signals with frequencies higher than the cut off frequency, (ii) a high- pass filter (HPF) passes signals with a frequency higher than the cut off frequency f_c and attenuates signals with frequencies lower than the cut off frequency, and (iii) a band pass filter passes frequencies within a certain range and attenuates frequencies outside that range. As RF noise results in a high dissipation, and that prevents to experimentally observe the effects of the targeted quantum region, the filter developed within the course of the of this thesis is to attenuate noise in all RF regions. This chapter shows the functioning principles, components and design of a prototype metal powder filter that can be implemented in a dilution environment for the removal of noise.

4.2 Metal powder filters

4.2.1 Functioning principles

Metal powder filters have shown highly effective performance for filtering out microwave frequencies. Such filters typically consist [3, 4, 5, 6] of a central LC circuit that is surrounded by a fine metal powder, e.g., copper or steel or metal powder/epoxy mixture. The radio frequency signals passing along the wire, are highly attenuated by the skin effect [2], where an alternating magnetic field emerges due to the AC current passing in a conductor. According to Faraday's law, further eddy currents are induced by the emerged magnetic field. As these currents oppose the initial change in the AC signal passing in the conductor, the signal is attenuated. The eddy currents are distributed where the current density is much higher near the outer surface of the conductor. A depth at which the current density falls to $1/e$ (about 0.37) of the surface current, is called the skin depth where a much higher electrical resistance influences signals with the higher frequencies which results in a higher attenuation.

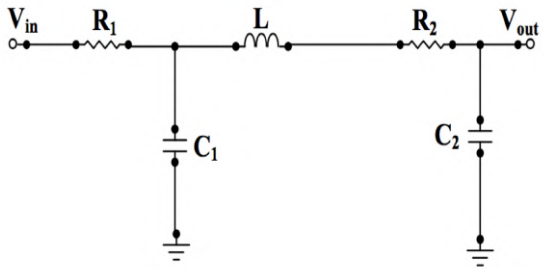

Figure 4.2: A representative circuit for the filter.

As powder filters typically consist of a central LC circuit (see Fig. 4.2) buried in a fine powder, e.g., copper or steel or metal powder/epoxy mixture, skin effect presents in such filters, where eddy currents are induced in the powder grains leads to a greater attenuation for the AC signals which finally improves the efficiency of filtering out the RF noise.

4.2.2 Earlier filters

Several types of filters have been previously developed such as thin film filters [7, 8, 9], distributed thin-film microwave filters [10], thermocoax filters [11]. As the space of a cryogenic system supposed to be occupied by the filters is an critical issue, particularly when several measurements are employed to be performed with different lines of a measurement system simultaneously, recent developments have focused on powder filters with higher performance [3, 4, 5, 6, 12] to remove the microwave noise in cryogenic environments.

A comparison between the attenuation of different filters that have been recently developed is shown in Fig. 4.3(a). The figure shows the attenuation measurements of the powder filter developed by Lukashenko *et al* [3]. Although the attenuation of this filter reaches to about -80 dB in frequency region above 1 GHz, it has a poor performance in the low frequency region below 100 MHz. An improvement for Lukashenko performance

filter has been accomplished by developing [1] RF filters for constrained cryogenic system. In these filters, the attenuation measurements indicated by the solid black line of Fig. 4.3(a), decreases gradually from about -10 dB at 10 MHz, to -45 dB at 100 MHz, and significantly drops up to -85 dB in the GHz region. The figure shows a further comparison between the performance of the two mentioned filters with thermocoax [11], and microcoax filters [14]. More recent metal powder filters have been reported in [15], where stainless steel powder and iron powder filters have been developed. Fig. 4.3(b) shows the attenuation measurements of theses filter, where the attenuation goes down to (*i*) -100 dB in the frequency regions above 20 GHz, (*ii*) -80 dB in the frequency region between 5 and 20 GHz, and (*iii*) between -30 and -80 dB in the frequency region between 1 and 5 GHz. Though such results exhibit high performance, the measurements show relatively weak attenuation in the low frequency region below 1 GHz.

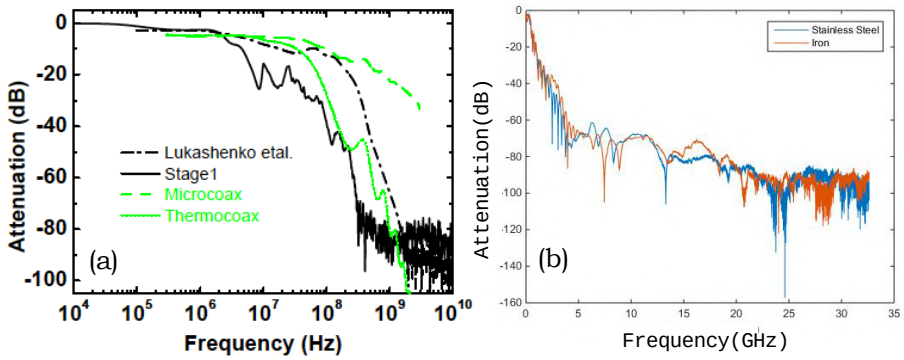

Figure 4.3: (a) A comparison between attenuation measurements of the presented in [1] and the filter designed by Lukashenko *et al* [3]. The figure shows also the attenuation curves of thermocoax [11] and microcoax filters [14]. (b) Attenuation for stainless steel and iron powder filters as reported in [15].

4.3 The prototype, basic materials and components

In the previous section, I have briefly showed how powder filters can effectively attenuate AC currents of microwave frequencies. As a part of the project of this thesis, a filter prototype developed to improve the attenuation performance in low and high frequency regions. The capability of using the filter for simultaneous measurements that take place in a cryogenic system has enabled it to be implemented in the experiments performed for acquiring the measurements given in Ch.6 of this thesis. For the long term goal of the project of this thesis, the filter will be finally used in future to attenuate the noise associated in SQUIDs and qubits.

Basic materials and components

The prototype of the powder filter which has been fabricated within the project of this thesis was designed following a technique proposed in [3]. Here, the following materials were used:

- Stainless steel powder with 45 μm grain size (GoodFellow Ltd).
- Copper powder with 14-25 μm grain size (ALDRICH Ltd).
- Stycast 1266 epoxy for cryogenic use (LOCTITE Ltd).
- Copper wire with a diameter of 114 μm and purity of 99.9% (ADVENT Research Materials Ltd).

And the following components have been used:

- A filter box.
- Inductors made of Stycast, powder, and copper wire.
- Capacitors (4400-093LF - Power Line Filter, Chassis, 0.012 μF, 50 V, 10 A).
- 25-PIN micro d-connectors.

4.4 Implementation and construction

Each inductor bar of these shown in Fig. 4.4 is a thin cylindrical rod of diameter 4 mm and length 1.7 cm, and made by a mixture of copper powder and Stycast 1266 epoxy. The mixing ratio for the mixture follows:

- 43.86% Stycast 1266 part A
- 43.86% copper powder
- 12.28% Stycast 1266 part B

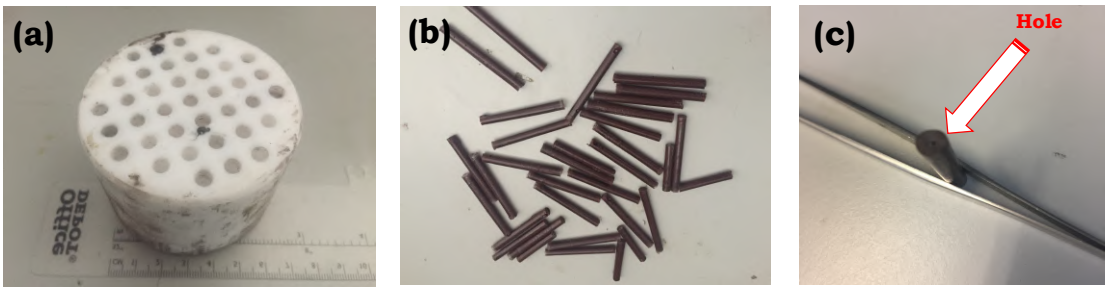

Figure 4.4: (a) The mould used to make the inductor bars, (b) the fabricated inductor bars, and (c) a drilled bar with a hole of about 0.8 mm.

The mixture is then filled in a mould such as that shown in Fig. 4.4(a), and remains inside the mould for about 48 hours to be dried. At this stage, the bars are stiff and can be ejected from the mould to finally become as these bars shown in Fig. 4.4(b). At this point, each bar is drilled longitudinally through the center of both circular ends with a hole of diameter of about 0.8 mm.

By using a CNC coil winding machine such as that shown in Fig. 4.5(a), the bar are wound with two layers of copper wire with a diameter of 114 μm and purity of 99.9%. At this point, the bars shown in Fig. 4.5(b) are ready to be used as inductors. A simple LCR meter was used to measure the inductors inductance, from which the measured inductance values are about 49.0 μH at room temperature, and 48.2 μH in liquid nitrogen.

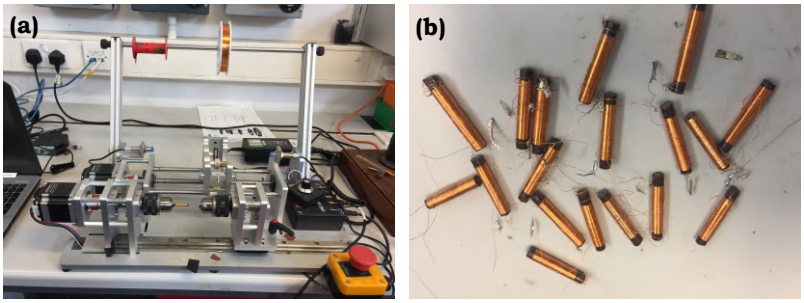

Figure 4.5: (a) CNC coil winding machine used for the bars winding, and (b) inductor bars after winding.

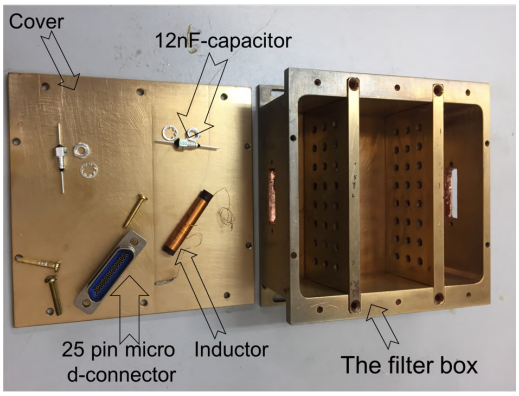

Figure 4.6: The designed filter box in which the filter's components are implemented.

Fig. 4.6 shows the designed filter box used to load 24 filters in an array of 8 columns and 3 rows, and micro d-connectors. With this design, the total elements implemented in this box are 24 inductors, two d-connectors, and 48 capacitors of capacitance of about 12 nF at room temperature, and 6 nF in liquid nitrogen.
When the inductors and capacitors are implemented inside the box according to the circuit given in Fig. 4.2, and in three layers with 8 inductors and 16 capacitors in each layer, the filter box and it's components will appear in such a way that shown in Fig. 4.7.

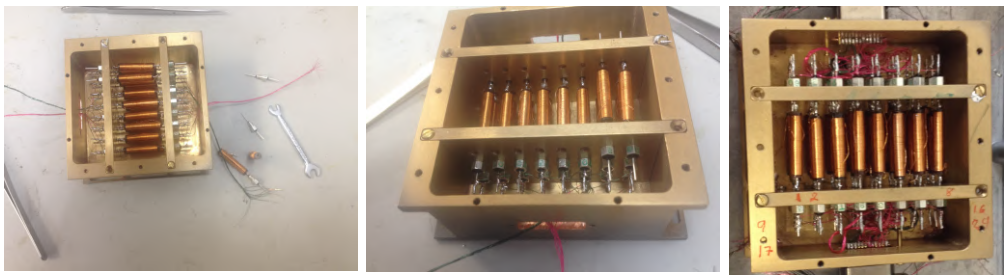

Figure 4.7: The appearance of filter box during and after implementing it's elements inside it. The filter's components follow the circuit diagram given in Fig. 4.2.

At this stage, the box is filled with Stycast epoxy mixed with stainless steel powder with 45 μ grain size. The mixing ratio for the mixture follows:

- 43.86% Stycast 1266 part A.
- 43.86% Stainless steel powder.

- 12.28% Stycast 1266 part B.

The box is covered then with a copper plate to isolate it from the environment. The construction at this stage is shown in Fig. 4.8. This is the final shape of the filter, at which the total weight of the box (including capacitors, inductors, epoxy, d-connectors) is 753 g.

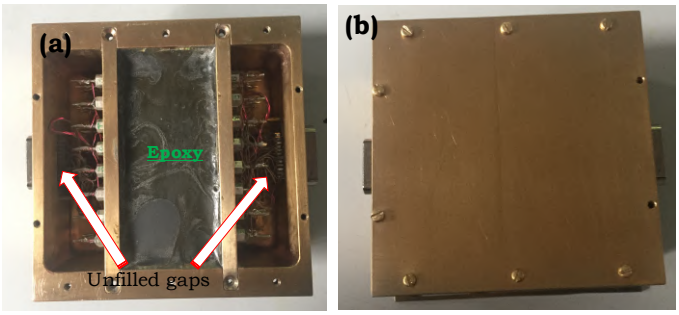

Figure 4.8: (a) A view for the filter after filling the box with epoxy mixed with stainless steel powder. (b) The final shape of the filter box after covering it with a copper plate to isolate it from the environment.

4.5 Measurements

Initially, the filter response was first tested at room temperature using a vector network analyzer (VNA) over the range between 100 kHz and 4.5 GHz. All 24 filters have been measured within this regime, and measurements for 10 of the 24 filters are shown in Fig. 4.9. The results show high reproducibility with an average attenuation of about -80 dB. High resolution measurements have been also performed in low frequency regions between 100 kHz and 500 MHz. Here, four selected measurements are shown in Fig. 4.10, in which the average attenuation is about -90 dB, with a relatively weaker attenuation of about -60 dB around 5 MHz.

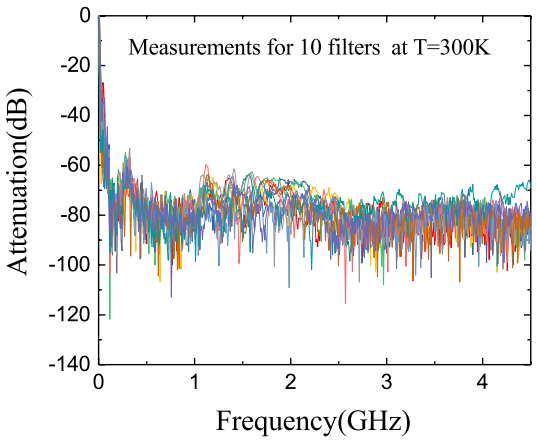

Figure 4.9: Attenuation curves of different 10 filters as measured at room temperature, and in a frequency region between 100 kHz and 4.5 GHz.

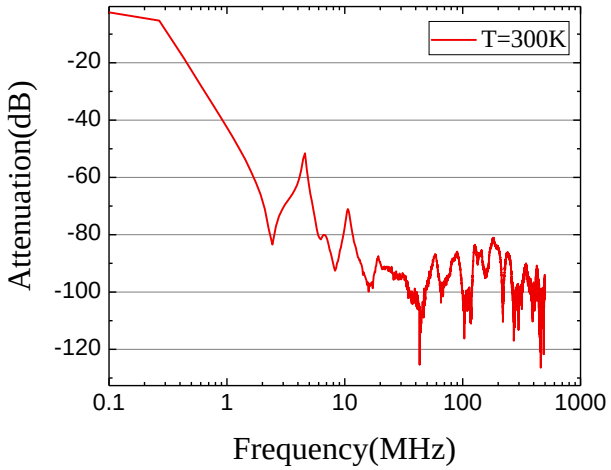

Figure 4.10: Selected high resolution measurements of attenuation response as performed at room temperature, and in low frequency regions between 100 kHz and 500 MHz.

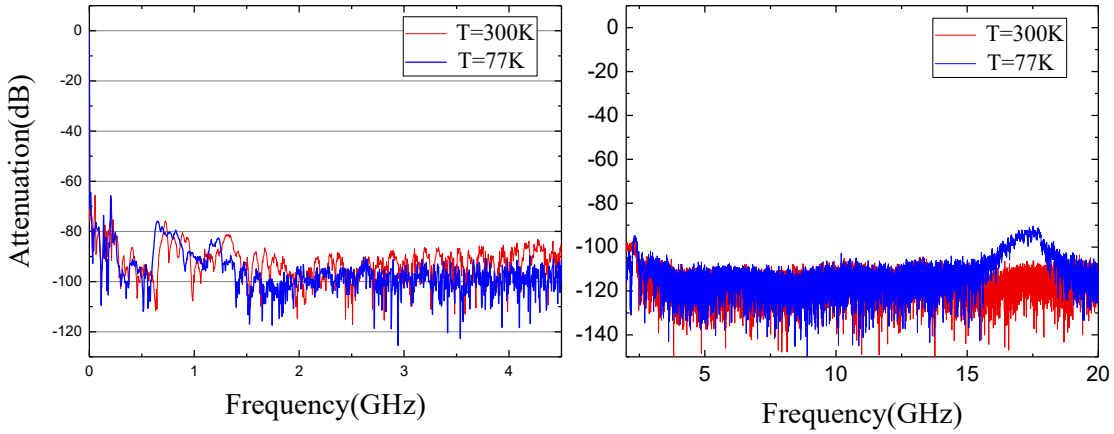

Figure 4.11: Filter performance comparison between 300 K and 77 K as measured between (a) 100 KHz and 4.5 GHz, and (b) 0.5 GHz and 20 GHz.

The filter was also measured with a range between 100 kHz and 20.0 GHz, whilst the filter was submerged in liquid nitrogen at 77 K. These measurements have been performed to investigate the filter performance at low temperatures. The performed measurements for high frequency regimes are shown in Fig. 4.11. The average of the measured attenuation for the high frequency regimes above 1 GHz, exceeds -110 dB. However, at 77 K, the attenuation power decreases slightly from about -110 dB at 15.7 GHz to -90 dB at 17.5 GHz before returning to the initial average line of -110 dB at 17.5 GHz. In contrast to previous measurements, the measurements presented in Fig. 4.11, have been performed when the gap shown in Fig. 4.8 were filled with stainless steel powder.

4.6 Coulomb blockade thermometer (CBT) measurements

A key consideration when designing filters for a dilution refrigerator [1] is the amount of space available to mount the filter box inside the fridge. As the filter box was designed for multiple lines, it's a bit bulky, in this case the space considerations may become an essential issue as the cooling power may be influenced, i.e., the temperature of the dilution room may not reach to the targeted point. To investigate the influence the filter on the cooling power of the dilution refrigerator, Coulomb blockade thermometer (CBT) is used to measure the temperature when the filter is placed on the mixing chamber plate, or on the 4K plate of the dilution refrigerator.

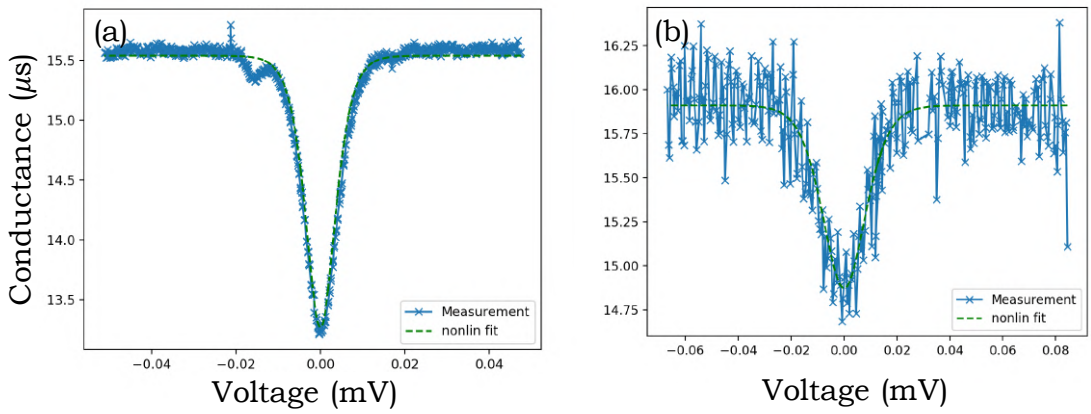

Figure 4.12: The measured conductance curve of the CBT sensor when the filter box is placed (a) on 4K plate, (b) on the the mixing chamber plate of the dilution fridge.

The principle of the CBT sensor is based on electrons tunnelling in small metallic tunnel junctions or arrays of junctions [16]. The differential conductance $G(V)$ dependence on temperature allows making the sensor an accurate tool for measuring ultra low temperatures down to few mK. From fitting of the conductance curve $G(V)$, the temperature can be obtained. For the CBT sensor used for the measurement presented in this section, an estimate of full width at half maximum of the $G(V)$ curve is given by

$$V_{1/2} = 5.439 N k_B T/e, \tag{4.1}$$

where $N = 33$ is the number of junctions in series, k_B is Boltzmann constant, and e is electron charge. The $I(V)$ characteristic of the CBT is described in [16], and further studies of the theory of the CBT sensor can be found somewhere else [17, 18, 19]. Here, the lock-in technique has been used to measure the CBT differential conductance. The equipments used in this technique are: (i) CBT sensor, Aivon CBT10, (ii) voltage preamplifier PA10, and (iii) lock-in amplifier SR830. The description of the experimental setup used for the CBT measurements presented here can be found in the manual of the commercial CBT10 sensor [20].

[1] Details about the dilution refrigerator setup are given Ch.6.

The filter box was first placed on the 4K plate of the dilution fridge, and the measured conductance curve of the CBT sensor was modelled using numerical calculations of conductance made using an algorithm derived from the free open-source library pyCBT21 [21]. According to these fittings, the tunnelling resistance R_T, the total capacitance C_Σ, and the temperature of the CBT sensor placed on the mixing chamber plate, were obtained as the following: $R_T = 32.1813\ \Omega$, $C_\Sigma = 230$ fF, and 8.41172 mK. In contrast, when the filter box and the CBT sensor were both placed on the mixing chamber plate of the dilution refrigerator, the tunnelling resistance $R_T = 31.4242\ \Omega$, the total capacitance $C_\Sigma = 230$ fF, and the temperature of the CBT sensor is 19.8295 mK. The recorded temperature of the mixing chamber plate when measurements are performed without placing the filter box on it was about 7 mK. Thus, there is a weak influence for the filter box on the cooling power as the temperature decreases only by about 1.5 mK when the filter box is placed on the 4K plate, and about 13 mK when the filter is placed on the mixing chamber plate. The conductance measurements of the CBT sensor are shown in Fig. 4.12.

It should be noted here, when the filter box is placed on the mixing chamber plate, a noise emerges in the measured $G(V)$ curve of the CBT sensor [Fig. 4.12(b)]. Such noise can be due to (i) the size of the filter box that may slightly prevent the temperature of the mixing chamber plate to be remarkably stable, and/or (ii) the interaction between the CBT sensor and the filter box as they become close to each others.

In conclusion, the results demonstrated in this chapter show that the prototype of the filter developed as a part of the work of the project of this thesis, can successfully attenuate signals to the noise floor level of -110 dB in high frequency regions, and between -60 dB and -110 dB in low frequency regions below 500 MHz. Such high performance makes it an efficient tool to attenuate the noise associated in SQUIDs and qubits, and very competitive to the filters developed earlier such those shown in Fig. 4.3. CBT measurements have shown that the filter developed here is appropriate to be used for simultaneous measurements that take place in a cryogenic system where the temperatures down to few mK.

Bibliography

[1] Mandal, Soumen, *et al.* "Efficient radio frequency filters for space constrained cryogenic setups." Review of Scientific Instruments **82**.2 (2011): 024704.

[2] Casimir, H. B. G., and J. Ubbink. "SKIN EFFECT. 2. SKIN EFFECT AT HIGH FREQUENCIES." Philips Technical Review **28**.10 (1967): 300.

[3] Lukashenko, A., and A. V. Ustinov. "Improved powder filters for qubit measurements." Review of Scientific Instruments **79**.1 (2008): 014701.

[4] Fukushima, Akio, *et al.* "Attenuation of microwave filters for single-electron tunneling experiments." IEEE transactions on instrumentation and measurement **46**.2 (1997): 289-293.

[5] Milliken, F. P., *et al.* "50 ω characteristic impedance low-pass metal powder filters." Review of Scientific Instruments **78**.2 (2007): 024701.

[6] Scheller, Christian P., *et al.* "Silver-epoxy microwave filters and thermalizers for millikelvin experiments." Applied physics letters **104**.21 (2014): 211106.

[7] Vion, D., *et al.* "Miniature electrical filters for single electron devices." Journal of Applied Physics **77**.6 (1995): 2519-2524.

[8] Courtois, H., *et al.* "Miniature low-temperature high-frequency filters for single electronics." Review of scientific instruments **66**.6 (1995): 3465-3468.

[9] le Sueur, Hélène, and Philippe Joyez. "Microfabricated electromagnetic filters for millikelvin experiments." Review of scientific instruments **77**.11 (2006): 115102.

[10] Jin, I., A. Amar, and F. C. Wellstood. "Distributed microwave damping filters for superconducting quantum interference devices." Applied physics letters **70**.16 (1997): 2186-2188.

[11] Zorin, A. B. "The thermocoax cable as the microwave frequency filter for single electron circuits." Review of Scientific Instruments **66**.8 (1995): 4296-4300.

[12] Lee, Sung Hoon, and Soon-Gul Lee. "Study on the fabrication of low-pass metal powder filters for use at cryogenic temperatures." Journal of the Korean Physical Society **69**.3 (2016): 272-276.

[13] Martinis, John M., Michel H. Devoret, and John Clarke. "Experimental tests for the quantum behavior of a macroscopic degree of freedom: The phase difference across a Josephson junction." Physical Review B **35**.10 (1987): 4682.

[14] https://www.carlisleit.com/brands/micro-coax/

[15] Quentin, Damien Charles. "Powder filters for a dilution fridge scanning tunneling microscope. Diss." University of British Columbia, 2016.

[16] Pekola, J. P., *et al.* "Thermometry by arrays of tunnel junctions." Physical review letters **73**.21 (1994): 2903.

[17] Hirvi, K. P., *et al.* "Arrays of normal metal tunnel junctions in weak Coulomb blockade regime." Applied physics letters **67**.14 (1995): 2096-2098.

[18] Pekola, J. P., *et al.* "Coulomb blockade thermometry in the Milli-Kelvin temperature range in high magnetic fields." Journal of low temperature physics **128**.5-6 (2002): 263-269.

[19] Meschke, M., *et al.* "Electron thermalization in metallic islands probed by coulomb blockade thermometry." Journal of low temperature physics **134**.5-6 (2004): 1119-1143.

[20] Manual of CBT Sensor CBT10 and Voltage preamplifier PA10, v 3.0. www.aivon.fi

[21] Python library for Coulomb Blockade Thermometer (CBT) data fitting. https://github.com/AivonOy/pyCBT.

5 Review of Superconducting Diamond: Properties, Fabrications, and Earlier Studies

5.1 The background and discovery

Naturally, diamond is composed of carbon atoms arranged in a crystal structure called diamond cubic. Exceptional physical properties of diamond makes it a candidate for plenty of applications in heavy industries and technology. For instance, as diamond is known as one of the hardest materials on the earth, it can be used in cutting, grinding, and polishing tools. Despite the fact that pure diamond is an insulator, it has unique physical properties by doping which converts it into a semiconductor or a superconductor. Naturally diamond forms at high temperatures and pressures that occur in the deep earth's shell about 140-190 km below earth's surface, and over a period of billions years [1]. Though extreme conditions, scientists have fabricated diamond in laboratories, where diamond is artificially grown by applying high pressure and high temperature. Another artificial process called chemical vapor deposition (CVD) has also been used to grow diamond [2]. The possibility of growing diamond films on large substrates, paves the way toward a variety of technological applications. Using the CVD process allows also controlling film properties such as the grain sizes which can vary from a few nanometres to micrometers [1]. The main interest of this thesis is the aspect of the CVD process associated with altering the boron concentration of boron doped diamond (BDD), which allows bringing the diamond to a superconducting phase.
In 2004, Ekimov *et al* [3] reported superconducting diamond where the superconductivity was performed by heavily doping near 3% hole concentration, hosting a type II superconducting state with a $T_c = 4$ K. However, with a homoepitaxial chemical vapor deposition (CVD) process, diamond films can be grown with the critical temperature of about 11 K [20].
Several theoretical studies have been reported to understand the origin of superconductivity in diamond such as: (i) correlated impurity band theory [5], (ii) localization of spin-flip driven hole pairs close to the Fermi level [6], and (iii) studies based on electron-phonon coupling [7, 8, 9, 10]. Although more experimental studies are still required for conclusive interpretation for the origin of the superconductivity in diamond, the theoretical studies based on electron-phonon coupling are specifically nominated for this purpose, as the superconductivity observed [11] in silicon boron doping, with a $T_c = 350$ mK where the low T_c is assigned [12] to the weaker lattice vibration and reduced electron-phonon coupling.

Despite the fact that the origin of the superconductivity in diamond is an attractive

research field, the main interest of this thesis is to develop a superconducting devices that can be used in future as micro and nano electromechanical systems that oscillate in the GHz regions. Thus diamond has been selected as it has a very high Young's modulus. Based on this goal, the fabrication process of diamond, and earlier studies on superconducting junctions and superconducting quantum interference devices (SQUIDs) that are made of diamond, are presented in the following sections.

5.2 Nanofabrication of boron-doped diamond devices

The films used in the experimental work performed for this thesis have been grown by CVD process on a silicon substrate of 500 μm thickness coated with layer of 500 nm thick silicon dioxide.

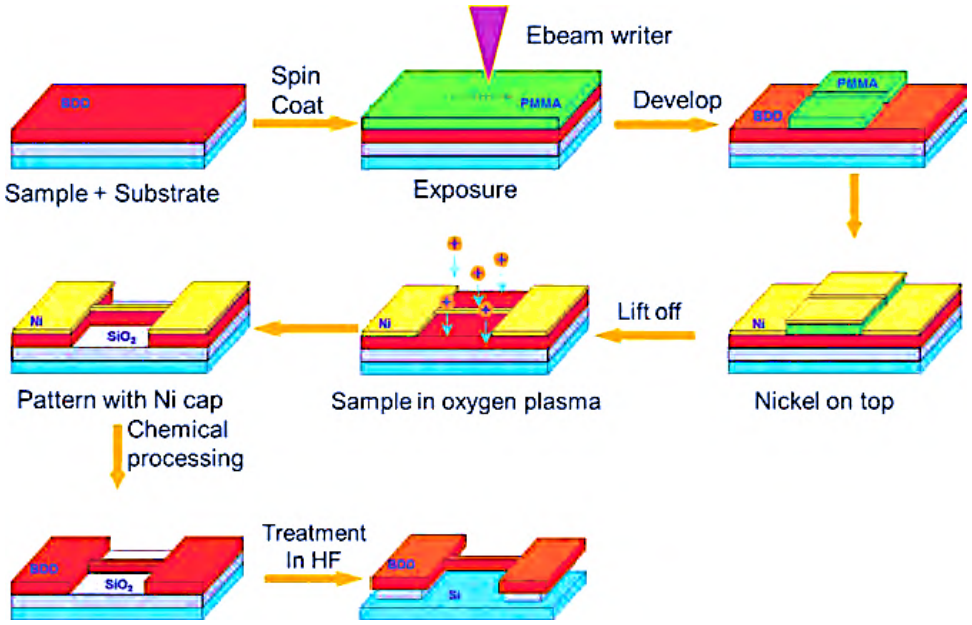

Figure 5.1: Schematic of the processes used in the fabrication of a superconducting circuit made of boron-doped diamond.

The nanofabrication of boron-doped diamond devices requires several processes, namely:

- growth process, in which boron-doped diamond was grown to a range of different thickness between 160-564 nm. The details of this process can be found in [13, 14, 15].
- Cleaning and rinsing, where the film is cleaned with acid solution, and then it is rinsed with water. Further organic pollutants was removed by acetone, and isopropyl alcohol was used to clean the surface.
- Spin coated process in which a 250 nm thick layer is formed with 4% polymethylmethacrylate (PMMA). The formed layer must be heated at 180 C for 5 min.
- Electron beam exposure and development: here, PMMA layer is exposed to an electron beam with a dose of 300 μCcm^{-2} with an acceleration voltage of 20 kV.

The PMMA layer is then developed for 35 s in a solution of 1:3 methyl isobutyl ketone (MIBK) and isopropyl alcohol.

- The layer is then covered with 65 nm of nickel using a standard electron-gun evaporator. The purpose of the nickel layer is to form a mask for the plasma etching process.
- Pattering and lifting off using acetone.
- Etching, this is performed by using an inductively coupled plasma-based reactive ion etching process.
- Removing the nickel mask using $FeCl_3$ solution, and then cleaning them by dilute acid solution, acetone, and isopropyl alcohol.
- Evaporating ohmic contacts on the contact pads. This process is achieved by photolithography and a standard electron-gun evaporation technique. With this process, a nano or micro superconducting circuit made of boron-doped diamond is completed.

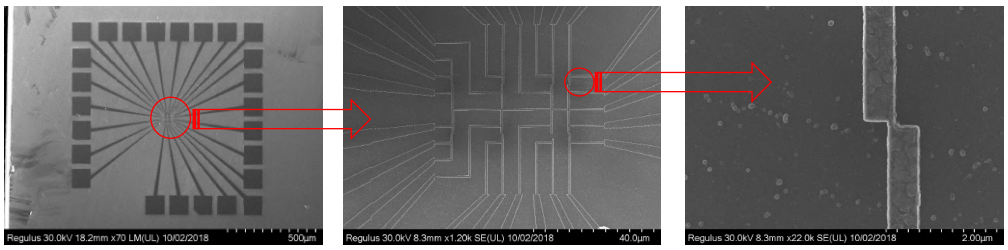

Figure 5.2: A superconducting circuit made from boron-doped diamond.

All processes given above are schematically in Fig. 5.1, and the final result for a superconducting circuit made of boron-doped diamond is shown in Fig. 5.2.

5.3 Earlier studies

5.3.1 Properties of BDD superconductors

As mentioned earlier, superconductivity was experientially proved [3] in boron-doped diamond by Ekimov *et al* in 2004. Afterword, the superconductivity in diamond has been revealed in CVD grown polycrystalline [16, 17], and single crystal films [18, 19].

Boron is an element with a total of five electrons, thus the number of valence electrons in boron is one less electron than those in carbon. The small atomic radius of boron atoms, enables inserting them between carbon atoms. When diamond is doped with boron, the electron configuration of boron makes it an acceptor while the resulting diamond becomes effectively hole (p-type) doped. In the CVD process, the diamond is doped with boron using gases such as diboran (B_2H_6), or trimethylboron (TMB) [20]. The concentration of BDD film can be controlled by changing the mixture ratio of methane and TMB.

Studies [3, 16, 19, 21] have shown that when the boron concentration is greater than 3×10^{20} cm^{-3} in a BDD film, the film enters the superconducting phase. It has been also

shown [24, 22, 23] that the susceptibility, T_C, conductivity, and the field H_{c2} of the BDD films depend strongly on the boron concentration. In Ref [19] magnetic and transport experiments on a set of single-crystalline epilayers doped in the range between 10^{20} and 10^{21} cm^{-3} have been reported. This study shows a rapid increase in T_c when the boron concentration is above some critical value ($n_c \sim 5 - 7 \times 10^{20}$) cm^{-3}. Results for the influence of n_c on T_c is given in Fig. 5.3(a), in which no transition was observed down to 50 mK for the film with $n_B = 3.6 \times 10^{20}$ cm^{-3}. When n_B is higher, the T_c increases rapidly reaching 2.1 K for $n_B = 19 \times 10^{20}$ cm^{-3}.

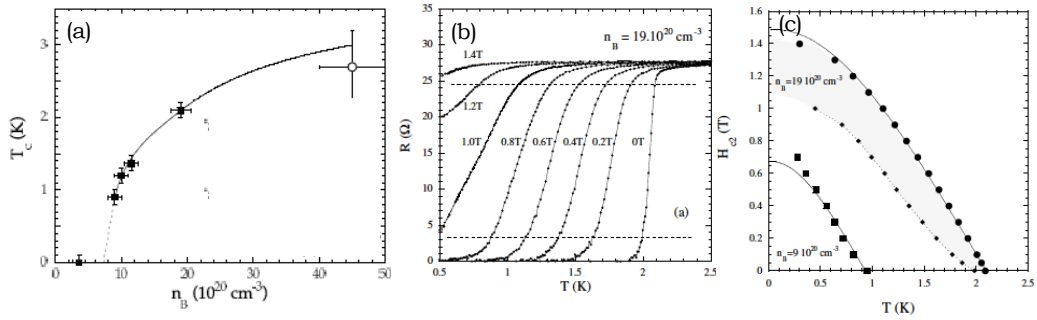

Figure 5.3: (a) Dependence of the superconducting transition temperature T_c on the boron concentration n_B, the open circle from [3]. (b) Temperature dependence of the electrical resistance at indicated magnetic fields for the film with $n_B = 19 \times 10^{20}$ cm^{-3}. (c) $H(T)$ phase diagram for the films with $n_B = 19 \times 10^{20}$, and $n_B = 19 \times 10^{20}$ cm^{-3}. Adapted from [19].

The influence of an external field on the superconducting transition of BDD films have been also studied [19]. Results for such studies are shown in Fig. 5.3(b) in which a BDD film with $n_B = 19 \times 10^{20}$ cm^{-3} shows a transition shift towards lower temperatures as the magnetic field is increased. The transition width remains relatively small up to ~ 1 T and rapidly increases for larger fields. The corresponding $H_{c2}(T)$ curves are shown in Fig. 5.3(c), from which $H_{c2}(0)$ can be extracted with 1.4 T. Thus, the corresponding coherence length, $\xi_{GL} = \sqrt{\Phi_0/2\pi H_{c2}(0)} = 15$ nm for a BDD film with $n_B = 19 \times 10^{20}$ cm^{-3}. For a BDD film with $n_B = 9 \times 10^{20}$, the $H_{c2}(0)$ is about 0.7 T, and the corresponding coherence length, $\xi_{GL} \sim = 22$ nm.

The estimated [25] mean free path ℓ as determined through a combination of Hall effect and conductivity measurements at 4.2 K was of the order of 0.5 nm. In the later reference the London penetration length have been also obtained with $\lambda_L = 150$ nm. Since $\ell \ll \xi \ll \lambda_L$, boron doped diamond is considered a dirty superconductor.

Tunnelling spectroscopy have been performed [26] at different locations of the surface of superconducting hole doped diamond films made of boron-doped single crystalline diamond epilayer (epitaxial wafer). The differential conductance measurements have been performed using a lock-in amplifier linked to the tip of scanning tunnelling microscope (STM) cooled down to a base temperature of 50 mK in a dilution refrigerator. Fig. 5.4 shows the temperature dependence of the superconducting gap $\Delta(T)$ as extracted from differential conductance measurements. The results given in the figure agree with the BCS theory with a T_c =1.85 K, where $\frac{\Delta}{k_B T_c} \simeq 1.74$.

STM images of the vortex lattice of BDD films in a dilution refrigerator at 50 mK have also obtained at fields H of 1200 Oe and 1900 Oe. The STM images are shown in Fig.

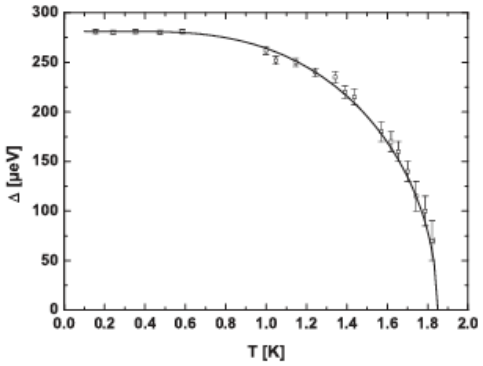

Figure 5.4: Temperature dependence of the superconducting gap of boron-doped single crystalline diamond (open squares) compared with a BCS theory with $T_c = 1.85$ K (solid line). Adapted from [26].

5.5, in which the spatial distribution of the measured vortices is strongly disordered even though a local hexagonal arrangement persists. Although the lattice is on the contrary of the perfect Abrikosov vortex lattice, and appears strongly disordered, autocorrelation pictures have been obtained using the autocorrelation function defined by $G(\delta x, \delta y) = \int I(x + \delta x, y + \delta y) I(x, y) dx dy$, where $I(x, y)$ is the local degree of brightness, G gives the probability of finding a similar brightness in the image for a spatial shift equals to $\delta(\delta x, \delta y)$ from any point. The obtained autocorrelation pictures shown in Fig. 5.5, exhibit a sixfold symmetry of first rings of neighbours which indicates a persistental order for any site of the lattice.

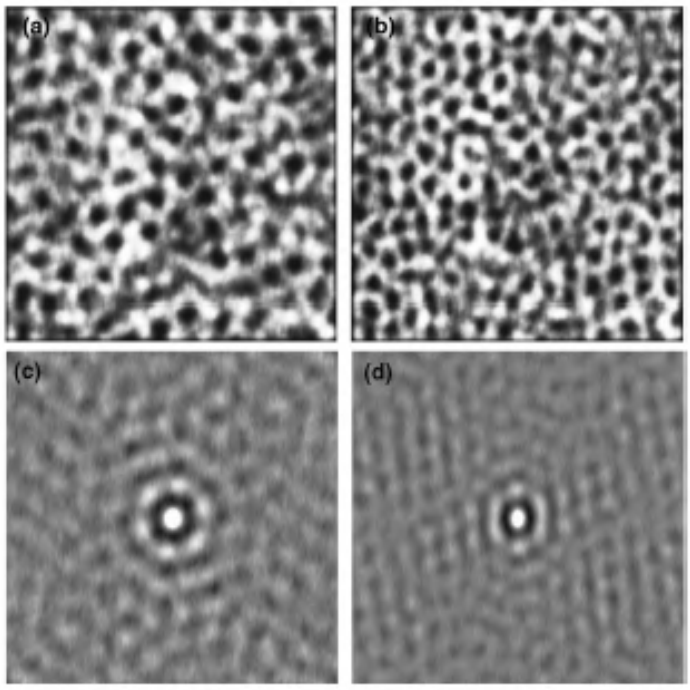

Figure 5.5: Vortex images (1.5×1.5 μm ^{2}) at two different magnetic fields: (a) 1200 Oe, (b) 1900 Oe. (c) and (d) The corresponding images as obtained from autocorrelation function. Adapted from [26].

Investigations of boron-doped granular diamond provide the understanding of the influence of disorder at different length scales. A study [27] conducted in 2008 has shown that superconductivity caused by the heavy boron doping in diamond is highly unlikely, mainly because of the microstructure of polycrystalline boron-doped diamond. in contrast to that argument given in [27], results [28] of dark-field scanning transmission electron microscopy (ADF-STEM), electron energy-loss spectroscopy (EELS), STM/STS, electrical transport, and magnetization measurements, superconductivity has been observed in polycrystalline, and coincides with the substitutional heavy boron doping in diamond grains.

The coherence length of a clean monocrystalline diamond as reported in [19] is $\xi_0 = 15$ nm. In contrast, two distinct coherence lengths must be considered [29] for granular systems: (i) the coherence length associated with a Cooper pair which straddles a grain boundary through tunneling ξ_t, and (ii) that for a Cooper pair contained within a single grain ξ_g. Both ξ_t, and ξ_g are given in terms of diffusion constant as: $\xi_t = (\pi\hbar D_{eff}/8k_BT_c)$, and $\xi_g = (\pi\hbar D/8k_BT_c)$. Here, D stands for the single-crystal diffusion constant, while D_{eff} is the bulk effective diffusion constant. For granular boron-doped nanocrystalline diamond (BNCD), the location of cross-overs in the $R(T)$ trace was used to estimate [32] these values as: $D \approx 12$ cm$^2/s$, and $D_{eff} \approx 0.6$ cm$^2/s$. Thus, $\xi_t \approx 7$ nm, and $\xi_g \approx 30$ nm. The upper critical field can be also estimated using the formula $H_{c2} = \Phi_0/2\pi\xi^2$, from which H_{c2} is about 6.7 T. This value for H_{c2}, agrees with the reported value for BNCD in [17].

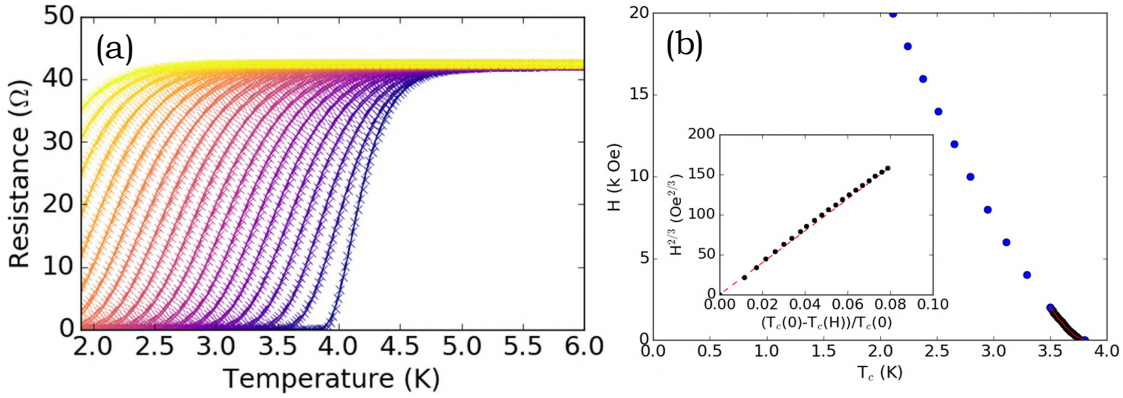

Figure 5.6: (a) $R(T)$ curves measurements as performed for BNCD film at applied magnetic fields between zero and 4 T. (b) Magnetic field dependence on transition temperature as obtained for a 564 nm thick BNCD film. Inset, $H(T)$ is a fit function where the date was analysed in terms of $H^{2/3}$ power law behaviour. Adapted from [31].

Other investigations for BNCD have been performed in [31], where measurements for the resistance dependence on temperature at different applied magnetic fields in the range between zero and 4 T, have been reported. These measurements are shown in Fig. 5.6(a), from which T_c can be precisely determined, and the magnetic field dependence on the temperature has been interpreted following the quasi de Almeida-Thouless $H^{2/3}$ behaviour, with $H_{irr} \propto (1-T/T_c)^{2/3}$. Such behaviour that can be observed in the fitting given in Fig. 5.6(b), was linked [31] with magnetic relaxation measurements from which a logarithmic decay of the remanent magnetization have been obtained following [33], which is coupled with observed irreversibility behaviour of $H_{irr}(T)$. As results, this coupling was attributed [31] to a superconducting glass state resulting from the morphological granularity of the

BNCD films.

5.3.2 Junctions made from diamond

As earlier demonstrated in the previous subsection, diamond exhibits superconductivity by doping it with boron. In terms of technology, a direct application of such discovery appears in possibility of forming a Josephson junction composed of diamond films. SNS weak-link Josephson junctions fabricated from a single-crystal BDD film, and by following the procedure outlined in [34] have been experientially investigated [35].

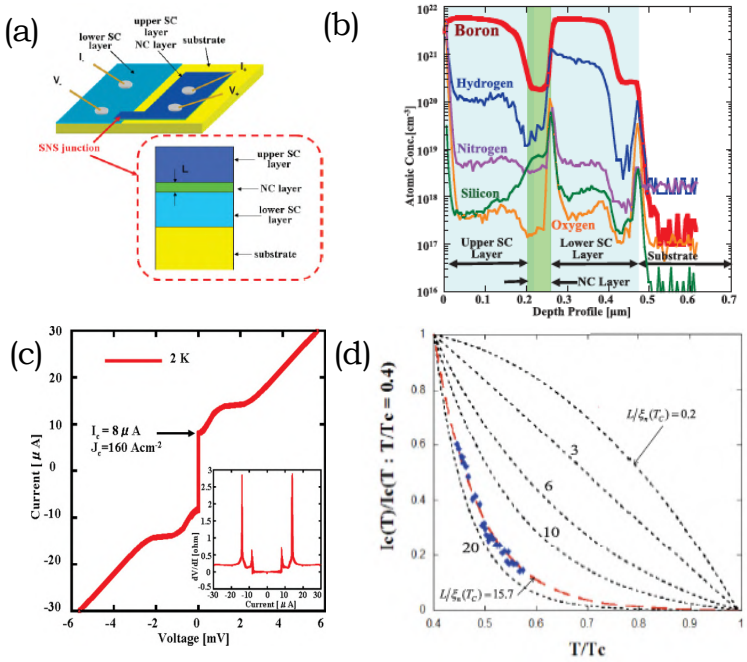

Figure 5.7: (a) Schematic of vertical SNS structure, in which a normal-state diamond film (NC layer) is sandwiched between two superconducting diamond films (lower SC layer and upper SC layer). (b) Depth profiles of the junction. (c) $I(V)$ characteristics of the junction at 2 K, and (d) the temperature dependence of the critical superconducting current I_c, and the one calculated from Likharev's theory of SNS junctions in the dirty limit. Adapted from [34].

$I(V)$ characteristics of the fabricated Josephson junction which schematically shown in Fig. 5.7(a) with depth profiles illustrated in Fig. 5.7(b), have been measured at 2 K as shown in Fig. 5.7(c), from which the critical superconducting current was extracted with $I_c = 8\ \mu$A. The temperature dependence of the critical superconducting current have been obtained and fitted to Likharev's theory developed in [36, 37] for SNS weak-link junctions. This is given as

$$\begin{aligned} I_c(T,L) &= \frac{2}{\pi e R_n}\frac{|\Delta_\infty|^2}{k_B T}\frac{L/\xi_n}{\sinh(L/\xi_n)} \qquad 0.3T_c < T < T_c \\ &\approx \frac{2}{\pi e R_n}\frac{|\Delta_\infty|^2}{k_B T}\frac{L}{\xi_n}\exp(-L/\xi_n), \end{aligned} \tag{5.1}$$

where Δ_∞ is the superconducting gap in the bulk of the superconductor described by BCS theory, L is the thickness of the NC layer [see Fig.5.7], and ξ_n is the coherent length in the normal conductor. Δ_∞ was calculated self-consistently by the following Eq. 4 given in [34]. For the dirty limit where the hole mean free path ℓ_n is much lower than the coherence length ξ_n, the later equation can be written [38] by expanding de Gennes' proximity theory [39, 40] to a three-dimensional free-electron gas model as:

$$\xi_n(T) = (3\pi^2 n)^{1/3} \sqrt{\frac{\hbar^3 \mu}{6\pi k_B T e m^*}}, \tag{5.2}$$

where m^* is the effective mass of the carriers, μ is the carrier mobility, and n is the carrier density of the semiconductor. The expression given in Eq. 5.2 has been successfully applied to estimate ξ_n for a SNS Josephson junction with a Pb/highly B-doped Si/Pb structure [41] in which the N (normal metal) region is highly boron-doped Si. In the presented model the SNS structure is analogous to that of highly boron-doped diamond, in which $m^* = 0.4m_e$, $\mu = 2$ cm^2/Vs, $n = 1.7 \times 10^{20}$ cm^{-3}. Thus $\xi_n = 3$ nm.

In Fig. 5.7(d) the temperature dependence of the critical superconducting current has been fitted [34] to Likharev's theory of SNS weak-link junctions described by Eqs. 5.1 and 5.2. The fit shows the signature of the proximity effect in SNS junctions [42] which agrees with experimental results when the non-superconducting layer thickness L is 15.7 times the coherence length $\xi_n(T)$, where the normalized critical current density exhibits exponential-like behaviour, $\exp(-L_{eff}/\xi_n)$, as

$$I_c(T, L) \approx \frac{4}{\pi e R_n} \frac{|\Delta_\infty(T)|^2}{k_B T_c} \frac{L}{\xi_n} \exp(-L/\xi_n(T)), \tag{5.3}$$

in which the superconducting gap $\Delta_\infty(T)$ in the bulk of the superconductor, dominates $I_c(T, L)$ when $L \ll \xi_n(T)$. However, if $L \gg \xi_n(T)$, the signature of the proximity effect in SNS junctions with an exponential-like behaviour $\exp(-L_{eff}/\xi_n)$ becomes obvious in the temperature dependence of the $I_c(T)$ functions.

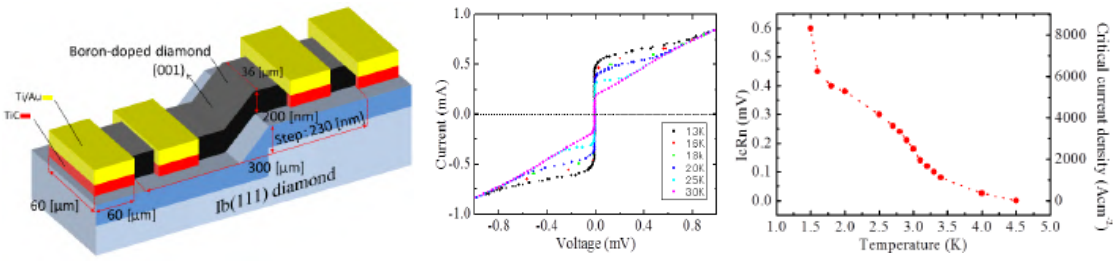

Figure 5.8: (a) The step edge structure Josephson junction of boron-doped diamond. (b) The $I(V)$ characteristic of the junction at various temperatures between 1.3 and 3 K, and (c) the critical currents in terms of I_cR_n, and the corresponding density current, J_c, as extracted from $I(V)$ characteristic. Adapted from [43].

In reference [43] fabrication process and characteristics of superconducting (111) boron-doped diamond junctions with regrowth-induced (001) step edge structure, has been reported. The transition temperature of the fabricated junction shown in Fig. 5.8(a) was measured with $T_c = 4$ K, and $I(V)$ characteristics of the junction have been also measured

at various temperatures between 1.3 and 3.0 K. The measured $I(V)$ curves as presented in Fig. 5.8(b) have shown overdamped signature with no hysteresis.

In Fig. 5.8(c), the temperature dependence of critical current in terms of I_cR_n, and the corresponding density current, J_c, have been extracted from the $I(V)$ curves. The behaviour of $I_c(T)$ has been attributed [43] to a weak link type Josephson junction effect. In 2019, three years later, a SQUID was developed [44] based on the function of the junction presented in Fig. 5.8. Such SQUID is briefly demonstrated in Sec. 5.3.3.2.

5.3.3 SQUIDs made from diamond

Although the wide range of applications of the superconducting quantum interference devices (SQUIDs), e.g, an ultra-sensitive motion detector of nano or micro mechanical resonators [45], there have been very less work [44, 46] on SQUIDs made of boron doped diamond. In this subsection the main experimental investigations on diamond SQUIDs are reviewed.

5.3.3.1 SQUIDs made of using nanocrystalline boron-doped diamond

Micro-SQUIDs patterned from a superconducting nanocrystalline diamond film of 300 nm thick, have been fabricated and investigated as reported in [46]. These diamond SQUIDs are shown in Fig. 5.9, where the mean loop area of all SQUIDs is 2.5×2.5 μm^2, 300 nm thickness, and various weak link designs of width of 250, 170, and 100 nm.

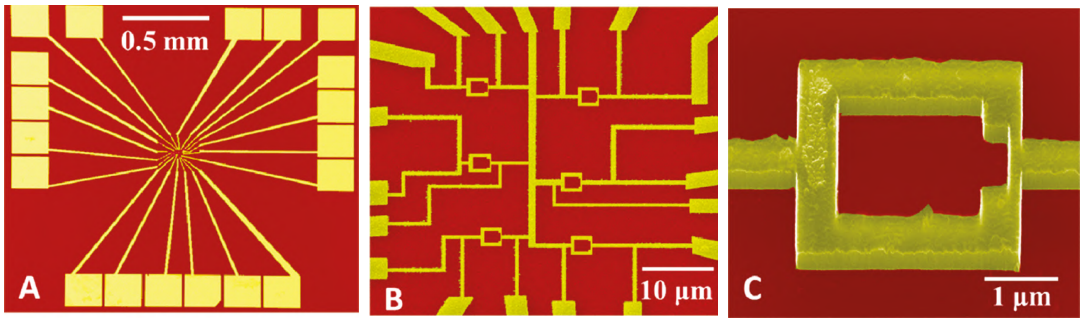

Figure 5.9: (a) The image of the complete diamond chip with total size of 2×2 mm^2. (b) A view for the middle of the chip with a scale of 50×50 μm^2 in which six different SQUIDs with different designs are shown. (c) A view of a single SQUID. Adapted from [46]

The transition temperature with $T_c = 4$ K has been obtained from the $R(T)$ curve measurements shown in Fig. 5.10(a). The $I(V)$ curves have been measured in absence and presence of magnetic field, from which the critical current have been obtained. In Fig. 5.10(c) and Fig. 5.10(d), $I_c(B)$ characteristics have been extracted with low field for two SQUIDs with width of 170, and 100 nm. The later $I_c(B)$ characteristics have shown oscillations with a period of about 0.31 mT, which has been attributed by the effective SQUID surface area of the measured SQUIDs. By repeating measurements at a fixed magnetic field, the histogram of I_c shown in Fig. 5.10(e) can be obtained, from which the full width at half-maximum was considered to find the devices sensitivity with about $4 \times 10^{-5}\Phi_0\text{Hz}^{-1/2}$. The magnetic field dependence of the critical current for the same

SQUID has been finally obtained by obtaining several histograms at different magnetic fields, and the extracted $I_c(B)$ function is given in Fig. 5.10(f).

Although the SQUID measurements presented in [46], and summarised here, can be an important step toward the detection of quantum motion of a cantilever implemented in a diamond-based SQUID, a prominent question mark arises regarding to the principle of such SQUID loop consisting of weak links with large width where, $L \gg \xi_0$. As mentioned earlier in Ch. 3, a typical Josephson junction requires a weak link of width in order of the coherence length ξ_0. Thus, the effect reported in [46] may be due to proximity effect discussed in Sec.5.3.2, or quantum phase slip dissusted in Sec. 2.4. However, more experimental and theoretical work are still required to find out the reasons behind this issue.

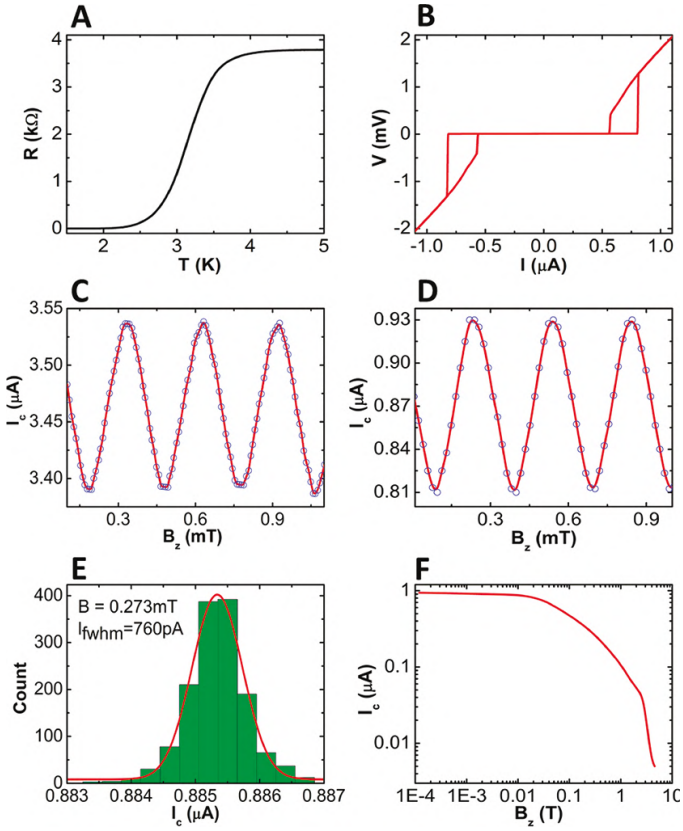

Figure 5.10: Characteristic features of the diamond SQUID as reported in [46]. (a) $R(T)$ curves showing a transition temperature at about 3 K which is close to the T_c of the diamond thin film. (b) $I(V)$ characteristics of the SQUID with a weak link of 100 nm wide, shows a hysterical behaviour with $I_c = 1$ μA. (c and d) Low field oscillations of the critical current as a function of magnetic field as measured for SQUIDs with weak link widths of 170 and 100 nm respectively. (e) Histogram of the switching current of a SQUID with a wide weak link of 100 nm wide, and (f) field dependence of the critical current for the same SQUID.

5.3.3.2 SQUID made of single-crystalline boron-doped diamond

In the previous subsection, I have briefly reviewed the only diamond SQUIDs reported until 2019, which has been fabricated from nanocrystalline boron-doped diamond with

a bridge-structured weak-link junction. However, based on the function of the single-crystalline boron-doped diamond Josephson junction with a regrowth step-edge structure demonstrated in Sec.5.3.2, a SQUID with new structure have been reported in [44]. The fabricated junction reported in [44] is shown in Fig. 5.11(a), in which the step angle (α) is the angle between the surface of the substrate and the step which is the parameter forming the junction. This angle was controlled during the fabrication process by adjusting the ratio of the thickness of the regrowth undoped layer d_{UN}, and etched step height h. $I(V)$ curves shown in Fig. 5.11(b) as measured at different temperatures between 1.6 and 3.4 K exhibit an overdamped type behaviour with I_c of about 52 μA at $T = 1.6$ K. By increasing the temperature, the critical current decreases as clearly shown in Fig. 5.11(c). The non-hysteretic behaviour, and the high critical current of such junction were considered as an advantage for fabricating high-performance junctions and SQUIDs.

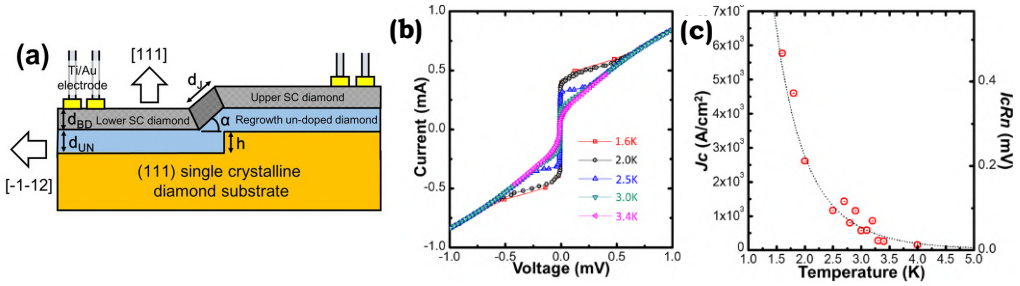

Figure 5.11: (a) Schematic diagram of cross-section of regrowth-induced step edge structure. (b) $I(V)$ curve at different temperatures between 1.6 and 3.4 K. (c) Temperature dependence of the critical current density and the critical currents in terms of I_cR_n. Adapted from [44].

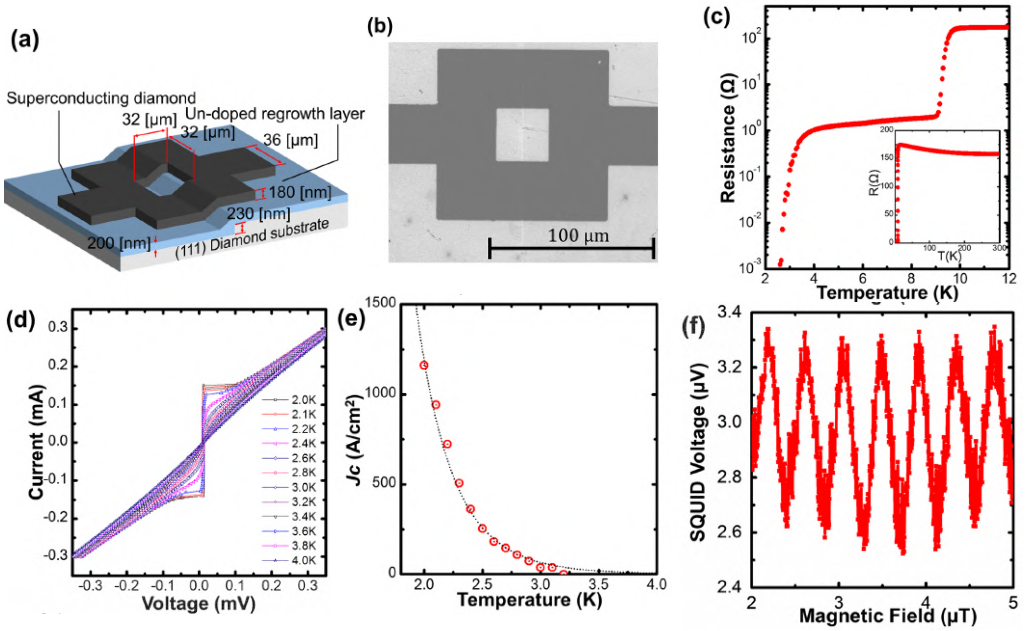

Figure 5.12: (a) Schematic diagram of single-crystalline diamond SQUID. (b) SEM image of the device. (c) Temperature dependence of the resistance, the inset shows the measurements from 300 K to 2 K. (d) $I(V)$ curves at temperature between 2.0 K and 4.0 K. (e) Temperature dependence of the critical current density. (f) $V(\Phi)$ characteristics of the fabricated SQUID at 2.6 K. Adapted from [44].

The transport properties of the fabricated single-crystalline diamond SQUID have been also reported [44]. The SQUID structure is shown in Fig. 5.12(a), and an overview of SEM image of a single device is shown in Fig. 5.12(b), in which the structural parameters have been adjusted to be the same as those for the single junction devise with $h = 200$ nm, $d_{UN} = 230$ nm, and $d_{BD} = 180$ nm, and $\alpha = 50$, with SQUID loop dimensions of 32×32 μm^2. Fig. 5.12(c) shows the $R(T)$ measurements of the SQUID in which T_c is similar to that obtained for the junction device from which the SQUID consists of. The reported $I(V)$ curves are presented in Fig. 5.12(d), and the temperature dependences of J_c are shown in Fig. 5.12(e). The $J_c(T)$ was fitted with $J_c(T) \propto \exp(\frac{-d_j}{\xi' \sqrt{(T_c)}} \sqrt{T})$ with $\frac{d_j}{\xi' \sqrt{(T_c)}} = 9.1$. The reported $V(\Phi)$ curve at 2.6 K presented in Fig.5.12(f) shows oscillations with an interval of about 0.43 μT, which corresponds to an effective area of 68×68 μm^2, and the peak-to-peak voltage $V_{p-p} \approx 0.8$ μV.

5.3.4 Superconducting micro and nanomechanical diamond resonators

In General, micro and nano mechanical resonators have attracted enormous attention as they can be used in several potential applications e.g, they can be used for ultra-sensitive mass [47, 48, 49], force [50, 51], charge [52, 53] and displacement detection [45, 54]. On the other hand, such systems allows studying macroscopic quantum phenomena. Regarding to this perspective, significant progress has been made in the last years by cooling a nano-mechanical resonator into its ground state [55, 56, 57, 58]. Etaki, *et al* [45] have demonstrated that a SQUID made of Niobium (Nb), could be utilised to detect motion of a 2MHz mechanical resonator. However, with such low frequency, the measured position resolution was about 133 fm (36 times the quantum limit), which is still far from the quantum regime.

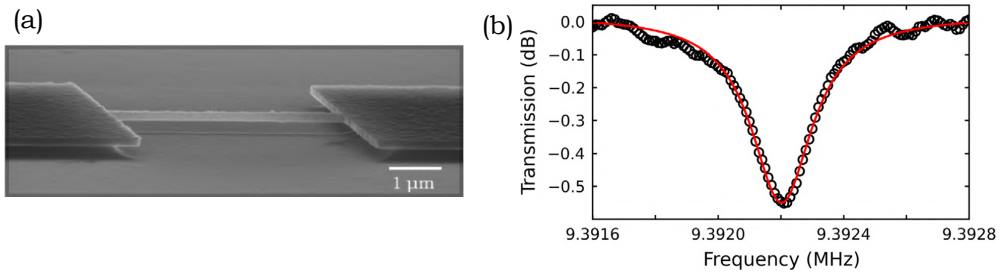

Figure 5.13: (a) Scanning electron micro-graph of a diamond resonator with dimensions of 480×300 nm^2. (b) Mechanical resonance at $B = 2$ T showing a quality factor of 4.0×10^4. The red line is a Lorentzian fit. Adapted from [60].

The fundamental frequency of a mechanical resonator is determined by [59]

$$f_0 = 1.028 \sqrt{\frac{E}{\rho}} \frac{d}{L^2}, \tag{5.4}$$

where E is the Young's modulus, ρ is the density, and L and d are the length and thickness of the cantilever respectively. From this point, diamond was chosen as it has the highest

Youngs modulus. This enables using it for detecting high frequencies approaching 1GHz, and allowing the system to enter a macroscopic quantum ground state at about 20 mK, where a single phonon mode is occupied. Thus, superconducting diamond is potentially a perfect candidate for the realization of nanomechanical resonators with high quality factors Q_0. A study on doubly clamped resonators made from boron-doped diamond has been reported in [60], where mechanical resonators such that shown in Fig. 5.13 exhibits superconducting properties up to magnetic fields of 3 T, and quality factors as high as 4.0×10^4 at a resonance frequency of around 10 MHz. Such resonator allows an implementation into fully superconducting diamond circuits such as diamond SQUIDs demonstrated in the previous sections.

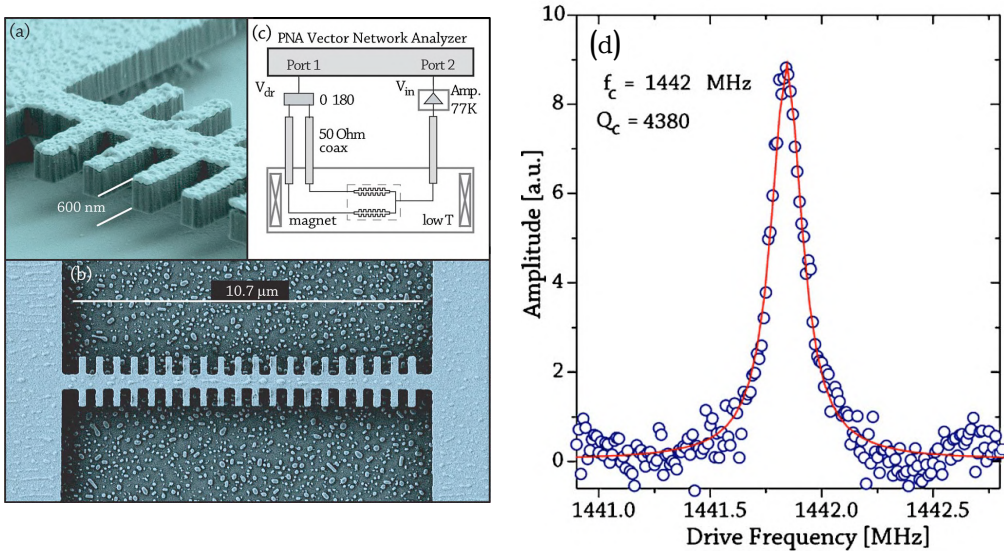

Figure 5.14: Measurement setup and SEM pictures of diamond antenna structure. (a) A close up view of the structure. (b) A top view of entire structure with two central beams containing two rows with 20 perpendicular cantilevers. (c) The measurement electronics setup used for actuation and detection of the amplitude and the phase. (d) The amplitude response of the 1.441 GHz mode, including Lorentzian fit indicated by the solid red line, from which the quality factor of 4380 is extracted. Adapted from [61].

Actuation and detection of GHz range resonance frequencies of nanocrystalline diamond mechanical resonators have been reported in [61], where transverse vibration modes have been measured in coupled-beam resonators with frequencies up to 1.441 GHz. The process used for the fabrication of such resonator is described in [61, 62, 63]. In Fig. 5.14(a) and (b) fabricated resonators are displayed where the structure contains a central beam of 21×0.4 μm^2, with 20 cantilevers of a width of 300 nm ,and a length of 500 nm, perpendicular to the central beam. The actuation and detection of the amplitude and the phase of the resonators have been investigated at 40 mK using the setup schematically shown in Fig. 5.14(c). As shown in Fig. 5.14(d), the highest frequency mode for these resonators has been reported in [61] with 1.44 GHz, and a quality factor of about 4380. Although, the cantilevers presented in this context are with high frequency, which makes them promising in respect of superconducting quantum circuits, they still require further improvement in terms of their quality factor.

Bibliography

[1] Mandal, Soumen, Tobias Bautze, and Christopher Bäuerle. "Superconductivity in Nanostructured Boron-doped Diamond and its Application to Device Fabrication." Nanodiamond. Royal Society of Chemistry, 2014. 385-410.

[2] Werner, M., and R. Locher. "Growth and application of undoped and doped diamond films." Reports on Progress in Physics **61**.12 (1998): 1665.

[3] Ekimov, E. A., *et al.* "Superconductivity in diamond." nature **428**.6982 (2004): 542-545.

[4] Takano, Yoshihiko. "Superconductivity in CVD diamond films." Journal of Physics: Condensed Matter **21**.25 (2009): 253201.

[5] Baskaran, Ganapathy. "Impurity band Mott insulators: a new route to high Tc superconductivity." Science and technology of advanced materials **9**.4 (2009): 044104.

[6] Mareš, JiříJ, *et al.* "Selected topics related to the transport and superconductivity in boron-doped diamond." Science and technology of advanced materials **9**.4 (2009): 044101.

[7] Lee, K-W., and Warren E. Pickett. "Superconductivity in boron-doped diamond." Physical review letters **93**.23 (2004): 237003.

[8] Xiang, H. J., *et al.* "Electron-phonon coupling in a boron-doped diamond superconductor." Physical Review B **70**.21 (2004): 212504.

[9] Ma, Yanming, *et al.* "First-principles study of electron-phonon coupling in hole-and electron-doped diamonds in the virtual crystal approximation." Physical Review B **72**.1 (2005): 014306.

[10] Giustino, Feliciano, *et al.* "Electron-phonon interaction via electronic and lattice Wannier functions: Superconductivity in boron-doped diamond reexamined." Physical review letters **98**.4 (2007): 047005.

[11] Bustarret, Etienne, *et al.* "Superconductivity in doped cubic silicon." Nature **444**.7118 (2006): 465-468.

[12] Liu, Chang, *et al.* "Superconductivity in Compression-Shear Deformed Diamond." Physical Review Letters **124**.14 (2020): 147001.

[13] Williams, Oliver A., *et al.* "Enhanced diamond nucleation on monodispersed nanocrystalline diamond." Chemical Physics Letters **445**.4-6 (2007): 255-258.

[14] Williams, Oliver Aneurin, *et al.* "Growth, electronic properties and applications of nanodiamond." Diamond and Related Materials **17**.7-10 (2008): 1080-1088.

[15] Williams, Oliver Aneurin. "Nanocrystalline diamond." Diamond and Related Mate-

rials **20**.5-6 (2011): 621-640.

[16] Takano, Yoshihiko, *et al.* "Superconductivity in diamond thin films well above liquid helium temperature." Applied physics letters **85**.14 (2004): 2851-2853.

[17] Takano, Yoshihiko, *et al.* "Superconductivity in polycrystalline diamond thin films." Diamond and related materials **14**.11-12 (2005): 1936-1938.

[18] Kačmarčik, J., *et al.* "Superconductivity in boron-doped homoepitaxial (001)-oriented diamond layers." physica status solidi (a) **202**.11 (2005): 2160-2165.

[19] Bustarret, Etienne, *et al.* "Dependence of the superconducting transition temperature on the doping level in single-crystalline diamond films." Physical review letters **93**.23 (2004): 237005.

[20] Takano, Yoshihiko. "Superconductivity in CVD diamond films." Journal of Physics: Condensed Matter **21**.25 (2009): 253201.

[21] Blase, Xavier, Ch Adessi, and Damien Connetable. "Role of the dopant in the superconductivity of diamond." Physical review letters **93**.23 (2004): 237004.

[22] Klein, Thierry, *et a*l. "Metal-insulator transition and superconductivity in boron-doped diamond." Physical Review B **75**.16 (2007): 165313.

[23] Kawano, Akihiro, *et al.* "Superconductor-to-insulator transition in boron-doped diamond films grown using chemical vapor deposition." Physical Review B **82**.8 (2010): 085318.

[24] Bustarret, Etienne. "Superconducting diamond: an introduction." physica status solidi (a) **205**.5 (2008): 997-1008.

[25] Winzer, K., D. Bogdanov, and Ch Wild. "Electronic properties of boron-doped diamond on the border between the normal and the superconducting state." Physica C: Superconductivity and its applications **432**.1-2 (2005): 65-70.

[26] Sacépé, B., *et al.* "Tunneling spectroscopy and vortex imaging in boron-doped diamond." Physical review letters **96**.9 (2006): 097006.

[27] Dubrovinskaia, Natalia, *et al.* "An insight into what superconducts in polycrystalline boron-doped diamonds based on investigations of microstructure." Proceedings of the National Academy of Sciences **105**.33 (2008): 11619-11622.

[28] Zhang, Gufei, *et al.* "Global and Local Superconductivity in Boron-Doped Granular Diamond." Advanced Materials **26**.13 (2014): 2034-2040.

[29] Lerner, I. V., A. A. Varlamov, and V. M. Vinokur. "Fluctuation spectroscopy of granularity in superconducting structures." Physical review letters **100**.11 (2008): 117003.

[30] Klemencic, G. M., *et al.* "Fluctuation spectroscopy as a probe of granular superconducting diamond films." Physical Review Materials **1**.4 (2017): 044801.

[31] Klemencic, G. M., *et al.* "Observation of a superconducting glass state in granular superconducting diamond." Scientific reports **9**.1 (2019): 4578.

[32] Klemencic, G. M., *et al.* "Fluctuation spectroscopy as a probe of granular superconducting diamond films." Physical Review Materials **1**.4 (2017): 044801.

[33] Yeshurun, Yu, and A. P. Malozemoff. "Giant flux creep and irreversibility in an Y-Ba-Cu-O crystal: an alternative to the superconducting-glass model." Physical review letters **60**.21 (1988): 2202.

[34] Watanabe, M., *et al.* "Stacked SNS Josephson junction of all boron doped diamond." Physica C: Superconductivity and its applications **470** (2010): S613-S615.

[35] Watanabe, M., *et al.* "Vertical SNS weak-link Josephson junction fabricated from only boron-doped diamond." Physical Review B **85**.18 (2012): 184516.

[36] Likharev, K. K. "Superconducting weak links." Reviews of Modern Physics **51**.1 (1979): 101.

[37] Kupriyanov, M. Yu, and V. F. Lukichev. "Proximity effect in electrodes and the steady-state properties of yosephson SNS structures." Fizika Nizkikh Temperatur **8**.10 (1982): 1045-1052.

[38] Seto, J., and T. Van Duzer. "Low Temperature Physics LT 13, ed. KD Timmerhous, WJ O'sullivan and EF Hammel." (1974): 328.

[39] de Gennes, PGf. "Boundary effects in superconductors." Reviews of Modern Physics **36**.1 (1964): 225.

[40] De Gennes, Pierre-Gilles. Superconductivity of metals and alloys. CRC Press, 2018.

[41] Nishino, T., E. Yamada, and U. Kawabe. "Carrier-concentration dependence of critical superconducting current induced by the proximity effect in silicon." Physical Review B **33**.3 (1986): 2042.

[42] Delin, K. A., and A. W. Kleinsasser. "Stationary properties of high-critical-temperature proximity effect Josephson junctions." Superconductor Science and Technology **9**.4 (1996): 227.

[43] Hideko, Masakuni, *et al.* "Superconducting (111) Boron-doped Diamond Josephson Junction with Regrowth-induced (001) Step Edge Structure." diamond **4**: 7.

[44] Kageura, Taisuke, *et al.* "Single-crystalline boron-doped diamond superconducting quantum interference devices with regrowth-induced step edge structure." Scientific reports **9**.1 (2019): 1-9.

[45] Etaki, S., *et al.* "Motion detection of a micromechanical resonator embedded in a dc SQUID." Nature Physics **4**.10 (2008): 785-788.

[46] Mandal, Soumen, *et al.* "The diamond superconducting quantum interference device." ACS nano **5**.9 (2011): 7144-7148.

[47] Yang, Ya-Tang, *et al.* "Zeptogram-scale nanomechanical mass sensing." Nano letters **6**.4 (2006): 583-586.

[48] Jensen, K., Kwanpyo Kim, and A. Zettl. "An atomic-resolution nanomechanical mass sensor." Nature nanotechnology **3**.9 (2008): 533.

[49] Chaste, Julien, *et al.* "A nanomechanical mass sensor with yoctogram resolution." Nature nanotechnology **7**.5 (2012): 301-304.

[50] Braginsky, Vladimir Borisovich, and Anatoliĭ Borisovich Manukin. "Measurement of weak forces in physics experiments." (1977).

[51] Moser, Joel, *et al.* "Ultrasensitive force detection with a nanotube mechanical resonator." Nature nanotechnology **8**.7 (2013): 493-496.

[52] Steele, Gary A., *et al.* "Strong coupling between single-electron tunneling and nanomechanical motion." Science **325**.5944 (2009): 1103-1107.

[53] Lassagne, Benjamin, *et al.* "Coupling mechanics to charge transport in carbon nanotube mechanical resonators." Science **325**.5944 (2009): 1107-1110.

[54] Salman, Majdi, *et al.* "Quantitative analysis of the interaction between a dc SQUID and an integrated micromechanical doubly clamped cantilever." Journal of Applied Physics **125**.22 (2019): 224503.

[55] O'Connell, Aaron D., *et al.* "Quantum ground state and single-phonon control of a mechanical resonator." Nature **464**.7289 (2010): 697-703.

[56] Rocheleau, T., et al. "Preparation and detection of a mechanical resonator near the ground state of motion." Nature **463**.7277 (2010): 72-75.

[57] Teufel, John D., *et al.* "Circuit cavity electromechanics in the strong-coupling regime." Nature **471**.7337 (2011): 204-208.

[58] Chan, Jasper, *et al.* "Laser cooling of a nanomechanical oscillator into its quantum ground state." Nature **478**.7367 (2011): 89-92.

[59] Imboden, Matthias, and Pritiraj Mohanty. "Dissipation in nanoelectromechanical systems." Physics Reports **534**.3 (2014): 89-146.

[60] Bautze, Tobias, *et al.* "Superconducting nano-mechanical diamond resonators." Carbon **72** (2014): 100-105.

[61] Gaidarzhy, Alexei, *et al.* "High quality factor gigahertz frequencies in nanomechanical diamond resonators." Applied Physics Letters **91**.20 (2007): 203503.

[62] Imboden, Matthias, *et al.* "Scaling of dissipation in megahertz-range micromechanical diamond oscillators." Applied Physics Letters **90**.17 (2007): 173502.

[63] Li, Hao, *et al.* "Stress evolution in nanocrystalline diamond films produced by chemical vapor deposition." Journal of applied physics **100**.9 (2006): 094309.

6 Experimental Investigations: Junctions, Nanobridges, and Superconducting Strips

6.1 Fabricated junctions and nanobridges devices

By following the chemical vapor deposition (CVD) process demonstrated in Sec. 5.2, research partners in the school of physics and astronomy at Cardiff university have grown and prepared devices made from superconducting nanocrystalline diamond, that I measured and present in this chapter. These devices are patterned from a 250 nm thick superconducting nanocrystalline diamond film. The boron doped diamond films were grown by CVD on seeded silicon wafers with a silica buffer layer of 500 nm. Electron beam lithography is used then to pattern the films using a deposited thin mask for subsequent highly anisotropic oxygen plasma etching. Finally, titanium-platinum gold was deposited for the contact pads and the sample was annealed at 750° C to enhance ohmic properties. More details of the fabrication method is presented in the Sec. 5.2.

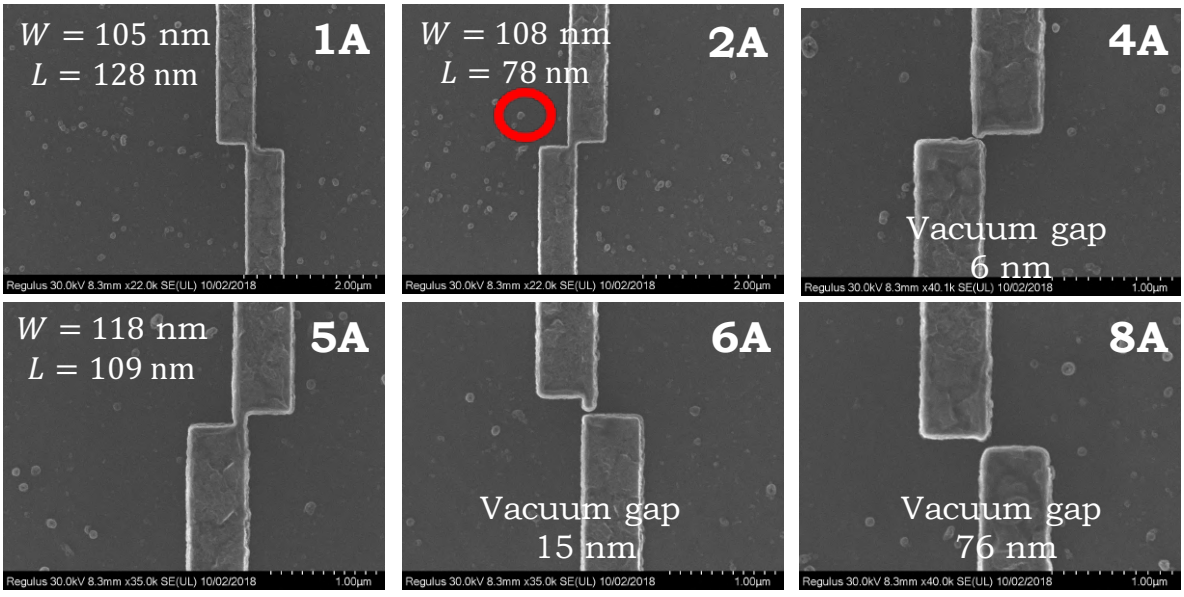

Figure 6.1: An image for the fabricated nanobridges and SIS junctions. All devices have been patterned from one diamond film. The red circle drawn on the image of device 2A, indicates superconducting diamond remainings.

As shown in Fig. 6.1, the fabricated junctions are different structures: (*i*) devices 1A, 2A, and 5A are with nanobridge structures of widths and lengths, and (*ii*) devices 4A, 6A,

and 8A are superconductor-insulator-superconductor (SIS) junctions, where the insulator in this case is a vacuum gap with widths of 6, 15, and 76 nm respectively. It should be noted here the following. The small islands appear in the regions around all devices such that the one indicated by the red circle drawn on the image of device 2A, are diamond remainings. However, these remainings are all isolated from the regions where the devices occupy, therefore, should not influence the measurements. All fabricated devices were integrated in the signal chip shown in Fig. 6.2(a), and (b), which can be then placed in a suitable sample box such that shown in Fig. 6.2(c), which is specifically designed to be installed inside the dilution refrigerator used to perform ultra low temperature measurements.

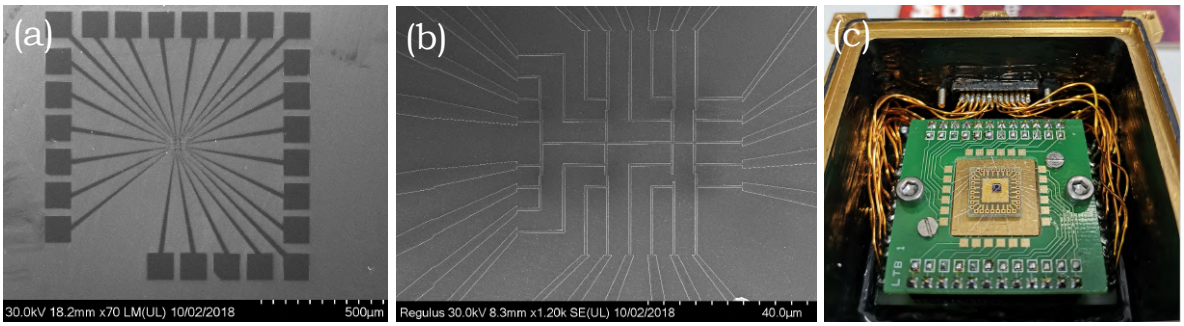

Figure 6.2: (a) The chip in which the fabricated devices have been integrated. (b) A close view of the chip, and (c) the adapter used to install the chip inside the dilution fridge.

6.2 Experimental methods

The devices presented in this thesis have been measured using two cryostats: (i) a physical property measurement system (PPMS) where the measurements were performed at $T = 1.8$ K or higher, and (ii) a dilution refrigerator where the measurements were performed at ultra low temperature down to 10 mK. Two different measurement types were performed: (i) $I(V)$ characteristics, and (ii) the differential resistance measurement. To improve the measurements accuracy, a four-terminal measurement method is used four sensing electrodes in which, the voltage drop across wires is prevented from being added to the actual voltage value of the sample. More details about four-terminal measurement method can be widely found in the literature [1].

6.2.1 Physical property measurement system (PPMS)

A large variety of physical properties can be measured using Physical Property Measurement System (PPMS) which consists of a dewar for thermal isolation, a superconducting magnet, liquid helium, and power source. The system is incorporated with several automated controllers for monitoring the temperature, gas flow, magnetic-field, and helium level. Quantum Design is a popular commercial form for such systems, the conditions of the experiment can be easily controlled by a software called MultiVu. The quantum design system used to perform some measurements presented in this thesis can be operated

in the temperature range between 1.8 and 400 K, and in applied magnetic fields up to 9 T. To perform transport measurements, the targeted sample is mounted inside a chamber which incorporates a universal 12-pin platform. More details about the working principle of PPMS can be found in [2].

6.2.2 Dilution refrigerator for ultra-low temperature measurement system

A ^{3}He/^{4}He dilution refrigerator is a cryogenic device that can provide cooling down to ultra-low temperature < 10 mK. To reach such temperature, several successive cooling stages take place. In the first stage, Pulse Tube (PT) technology is used for pre-cooling which enables the temperature to decrease to < 4.2 K.

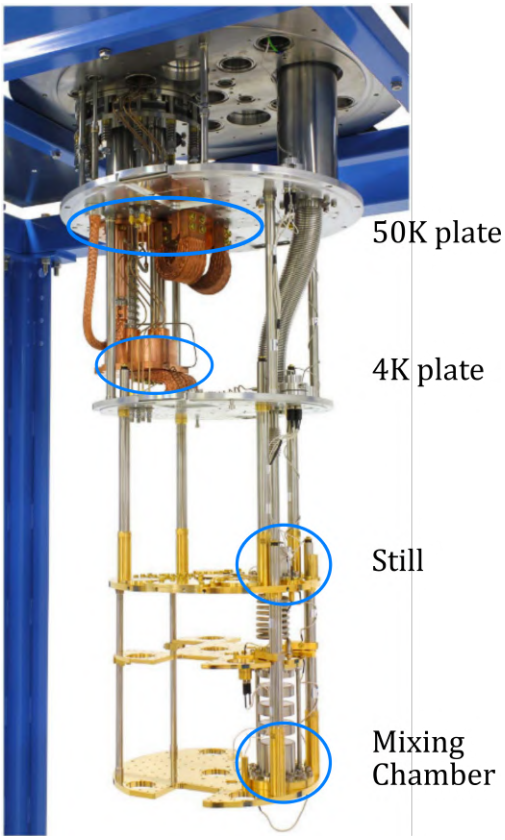

Figure 6.3: The interior of BlueFors dilution refrigerator used for the ultra low temperature measurements.

In the second stage, the temperature of the mixing charmer, which contains a mixture of ^{3}He/^{4}He, decreases to about 2.17 K, and ^{4}He undergoes a phase transition from a normal fluid into a superfluid. As the superfluid transition temperature decreases by diluting ^{3}He and ^{4}He, the temperature drops below certain critical temperature which is about 870 mK where the third stage starts, at which the mixture undergoes a phase change with two new phases: (*i*) a ^{3}He-rich phase (the concentrated phase), and (*ii*) a ^{3}He-poor phase with about 6.4 % ^{3}He (the dilute phase). Since the ^{3}He isotope is less massive, the concentrated phase floats on top of the dilute phase, which makes it easily to evaporate.

To steady the ^{3}He concentration of the dilute phase, a heat is supplied to the still which drives ^{3}He atoms to cross the phase boundary. Finally, as the enthalpy of ^{3}He in the dilute phase is larger than in the concentrated phase, an amount of energy is required to move ^{3}He atoms from the concentrated to the dilute phase. This energy is taken from a well isolated environment (the mixing chamber), which results in cooling. The major part of the measurements presented in this chapter were performed using a Bluefors LD250 dilution refrigeration system shown in Fig. 6.3. With this refrigerator a cooling up to 10 mK can be carried out. Technical details about this system can be found in [3].

6.2.3 Data acquisition setups

Several experimental setups were made using various types of electronic equipment for acquiring the data presented in this chapter. The setups were supported by codes written using the graphical language LabVIEW for specifically controlling the equipment, reading the data they measure, and recording them in sufficient files. The first setup was used alongside the PPMS, while the others were used for the measurements performed with the BlueFors dilution refrigerator.

6.2.3.1 $I(V)$ characteristics setups

The $I(V)$ curves have been measured by using the PPMS, and the dilution refrigerator cryostats. For the measurements associated with the PPMS, where the temperature and the magnetic field dependence of the $I(V)$ characteristics at $1.85 < T < 4$ K were performed, the experimental setup uses the equipment shown in Fig. 6.4.

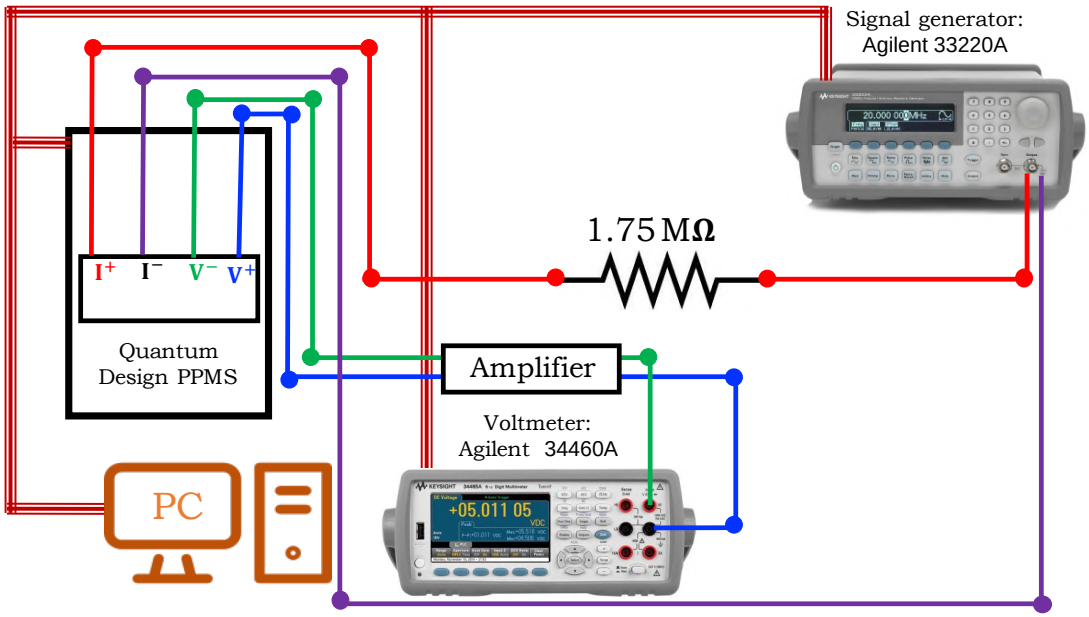

Figure 6.4: A schematic diagram of the experimental setup with which $I(V)$ characteristics were measured at different temperatures and magnetic fields. The setup uses the labeled electronic equipment and Quantum Design PPMS.

In this setup a signal generator (Agilent 33220A) was used in a triangle ramping mode to generate a dc current by connecting it to a load resistor of about 1.75 MΩ, the resulting dc current is then sent to the terminal I^+ of the device to be measured. The response of the device from the terminals V^+ and V^- are amplified using an amplifier with a 500 gain. After amplifying the voltage, a voltmeter (Agilent 34460A) was used to record it.

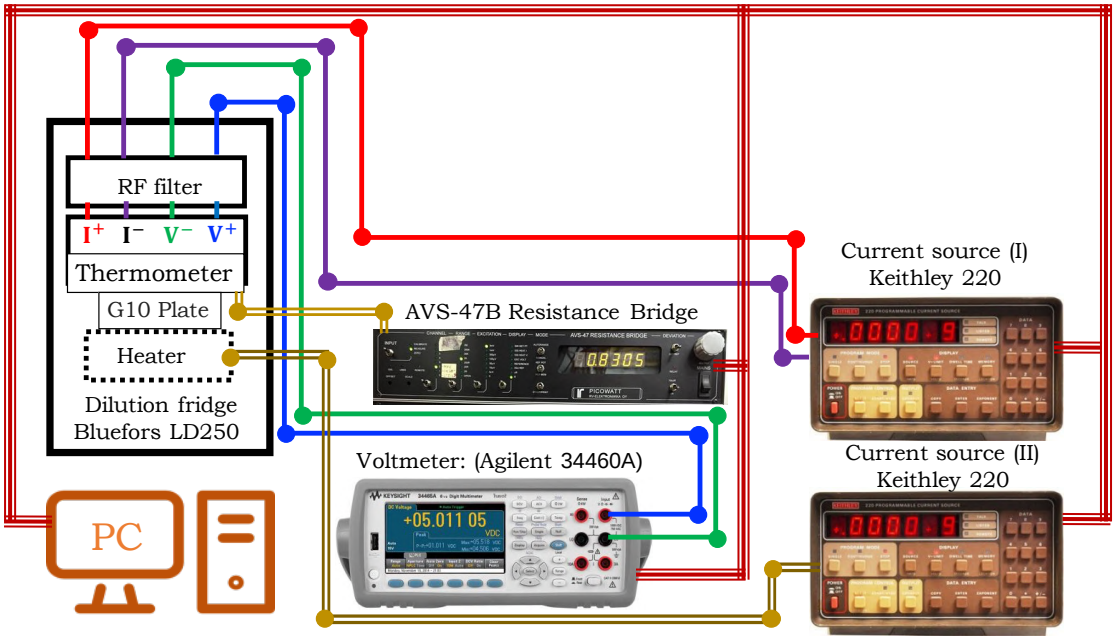

Figure 6.5: A schematic diagram of the experimental setup with which the temperature dependence of $I(V)$ characteristics were measured using the Bluefors dilution fridge. The setup was developed to measure and control the temperature using a high accurate thermometry system (AVS-47B Resistance Bridge, and low temperature thermometer) accompanied with temperature control system consisting of a thermal insulator (G10 plate), an additional current source that controls the power of a heater via PID control algorithms provided with LabVIEW software.

For the measurements associated with the Bluefors dilution fridge, where the temperature dependence of the $I(V)$ characteristics were measured using the experimental setup shown in Fig. 6.5. In this setup, a current source (Keithley 220) is used as bias, and a voltmeter (Agilent 34460A) was used to record it. To enable measuring the temperature dependence of $I(V)$ characteristics, an AVS-47B Resistance Bridge was used as thermometry at low and ultra low temperatures. The AVS Bridge is connected with a thermometer attached to the mixing chamber plate of the fridge. The temperature was controlled using a heater made of a simple copper coil, and connected to the second current source (Keithley 220) shown in the figure. A thermal insulator (G10 plate) was placed between the heater and the mixing charmer plate on which the sample box and the fabricated RF filter (see Ch. 4) are placed. A thermal insulator (G10 plate) was placed between the heater and the mixing charmer plate on which the sample box and the fabricated RF filter (see Ch. 4) are placed. As the passing current through the heater increases, the temperature increases, which in other words means that temperature can be stabilized at a specific value of the heater current fed by Keithley 220. However, during the measurements, a technical issue in keeping temperature constant arises due to the bias current passes through the device to be measured. As the bias current I_b is the one which appears in the $I(V)$ characteristics,

it must be swept during the measurements. Increasing I_b results in a thermal energy which finally changes the temperature depending on the length, width, and thickness of the device. Such a problem[1] was solved using a proportional integral derivative controller (PID controller) where the feedback of the thermometer acquired by the AVS bridge is used to adjust the output of the second current source that feeds the heater. The PID control algorithms used for this setup is the one developed by National Instruments (NI) which provides them as a part of LabVIEW software.

6.2.3.2 Differential resistance measurement setup

For differential resistance measurements, a lock-in amplifier is used as it can detect very small ac signals down to a few nanovolts. Lock-in amplifiers use a technique known as phase sensitive detection to single out the component of the signal at a specific reference frequency. Specifically, when an ac signal with frequency f_1 is multiplied by another one with frequency f_2, and integrated over a time much longer than the period of the two signals, the result is: either (i) zero if $f_1 \neq f_1$, or (ii) half of the product of the amplitudes of the two signals if $f_1 = f_1$ and the two signals are in phase.

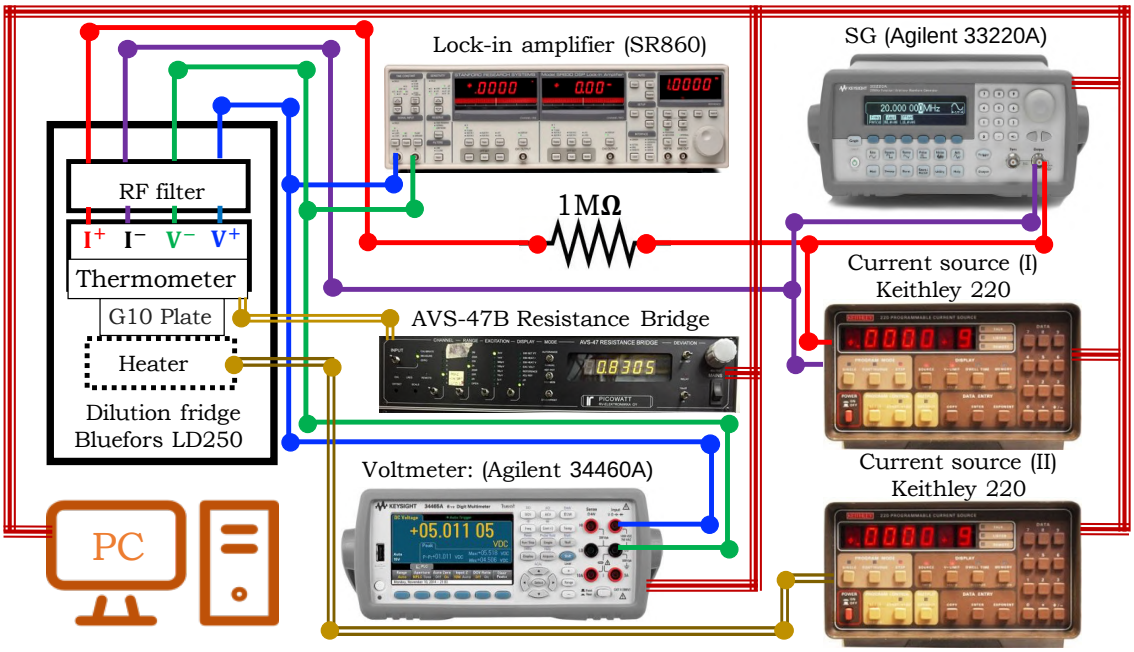

Figure 6.6: A schematic diagram of the experimental setup with which the temperature dependence of (dV/dI) were performed. The temperature is measured and controlled using an AVS- bridge, thermometer, G10 plate, heater, and PID control in the similar way followed in the setup shown in Fig. 6.5.

As a lock-in amplifier performs a multiplication of its input with a reference signal, and then applies an adjustable low-pass filter to the result, noise signals in the input terminal of the lock-in with frequencies other than the reference frequency are rejected and do not

[1] This problem emerges for devices with high critical currents, particularly for the device 8A. The problem was solved using the PID control as shown in Fig. 6.

affect the measurement. More details about principles and the state of the art of lock-in detection can be found in [4]. In the experimental setup shown in Fig. 6.6, the signal generator (Agilent 33220A) was employed[2] as an external reference for the used lock-in amplifier (SR860). A dc current source (Keithley 220) is used to output a dc current I_{dc}, and a small ac modulation current I_{ac} is combined by connecting a 1 MΩ resistor with the SG. This experimental setup can be used as a hybrid technique system, as it reduces to dc-measurements setup by turning off the SG. To enable measuring the temperature dependence of (dV/dI). The same equipment that measure and control the temperature in the setup shown in Fig. 6.5, were used here for performing the temperature dependence of (dV/dI) measurements.

6.3 Nanobridges measurements

The measurements presented in this section are those performed on the nanobridges devices: 1A, 2A, and 5A, where $I(V)$ characteristics and the differential resistance measurements (dV/dI) are reported.

Device 5A

First, $I(V)$ curves for device 5A (shown in Fig. 6.1) with bridge dimensions of $L = 118$ nm and $W = 109$ nm, were measured at various temperatures and magnetic fields using the experimental setup integrated with the PPMS which is schematically shown in Fig. 6.4, by which the $I(V)$ curves were measured in the absence of magnetic field at temperatures between 1.85 K and 4.0 K. Selected results for the $I(V)$ curves are shown in Fig. 6.7(a), and the critical currents I_c were extracted from all $I(V)$ curves measured between 1.85 K and 4.0 K. The critical current can be extracted from the dV/dI curve that can be measured by the look-in technique, or obtained by numerical differentiation of the $I(V)$ curve. Where, the I_c value occurs at the maxima of the dV/dI curve, at which $dV/dI = 0$. The critical current dependence on temperature $I_c(T)$ is plotted in Fig. 6.7(b), from which the critical temperature (T_c) can be obviously obtained with $T_c \approx 3.4$ K, at which the critical current drops to zero.

In Sec. 5.3.2, a study on the temperature dependence of the critical current for SNS weak-link junctions made of diamond was discussed in light of Likharev's theory [5, 6], where the $I_c(T)$ of a weak link with bridge of $L \gg \xi$ was fitted to a function with an exponential-like behavior, $\exp(-L_{eff}/\xi_n)$ that reduced from Eqs. 5.1 and 5.2. As the temperature dependence of the critical current has been fitted [7] to Likharev's theory of SNS weak-link junctions described by these equations. The fit shows the signature of the proximity effect in SNS junctions [8], which agrees with experimental results for a device with a non-superconducting layer thickness with $L \approx 15.7\xi_n(T)$, at which the normalized critical current density exhibits an exponential-like behaviour.
Following the superconducting diamond properties discussed in Sec. 5.3.1, where $\xi_{GL} = 15$

[2] In principle, the reference signal can generated by the lock-in amplifier (SR860) used in the experimental setup. However, due to technical issues, a separate signal generator was employed as an external reference.

nm, and taking into consideration that the ratio L/ξ_{GL} is about 8 for the device 5A, the critical current dependence on temperature can be examined for this device in terms of an $\exp(-L/\xi_n)$ function as the term, $L \gg \xi$ for this device. Since $\xi_n(T) \propto 1/\sqrt{T}$ as given in Eq. 5.2, the critical current dependence on temperature becomes: $I_c(T) \propto \exp(-L\sqrt{T})$. Accordingly, $I_c(T)$ was fitted to later function, and the result is shown in Fig. 6.7(c) in which $I_c(T)$ fits to $\exp(-L\sqrt{T})$ function when $1.85 < T < 2.5$ K.

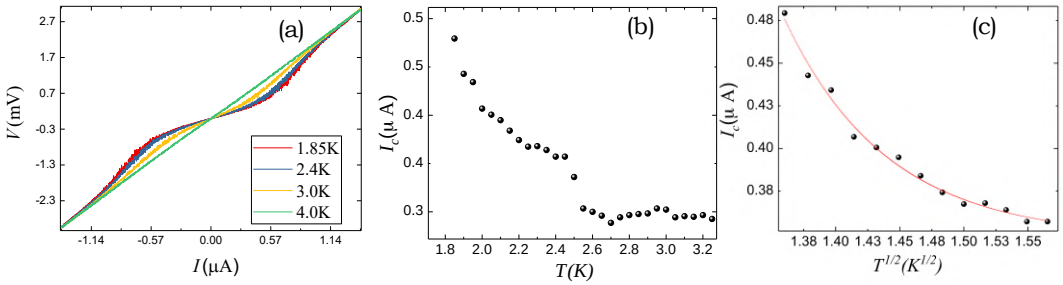

Figure 6.7: (a) Representative $I(V)$ characteristics of device 5A with bridge dimensions of $L = 118$ nm and $W = 109$ nm as measured at different temperature. (b) The critical currents of the device as extracted from the $I(V)$ characteristic measured at temperature between 1.85 and 3.6 K. (c) The critical superconducting current I_c dependence on $\sqrt{T}$ is plotted and fitted in terms of Likharev's theory of SNS junctions.

The $I(V)$ curves have been also measured at $T = 1.85$ K and various values of magnetic fields between zero and 1 T. Selected results of the measured $I(V)$ curves dependence on the field are shown in Fig. 6.8(a), and the result of critical currents $I_c(B)$ as extracted from all measured curves is shown in Fig. 6.8(b).

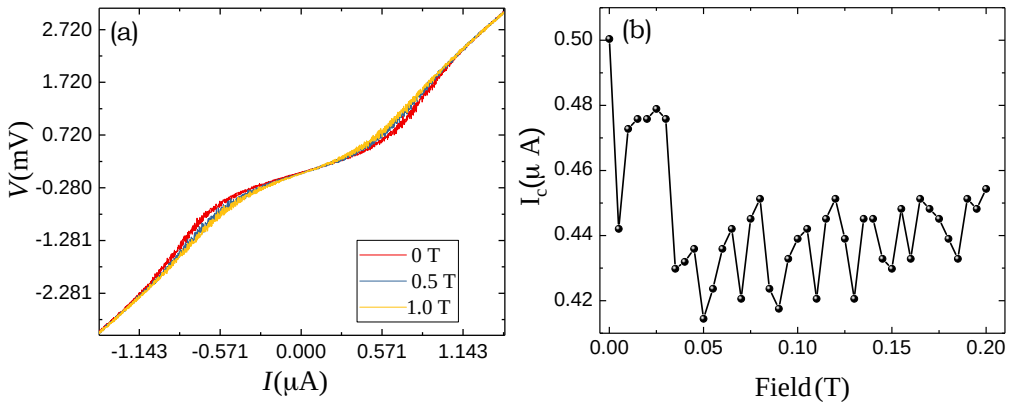

Figure 6.8: (a) Representative $I(V)$ characteristic of device 5A as measured at different magnetic fields. (b) The critical currents of the device as extracted from the $I(V)$ characteristics measured at $T = 1.85$ K, and different values of magnetic field between zero and 0.2 T. The RF filters were not used to attenuate the noise associated with these measurements.

As consequence of the later figure, $I_c(B)$ behaviour is quite noisy, and it unlikely emerges from the Fraunhofer pattern described by Eq. 3.46 which is plotted in Fig. 3.9(b). The discrepancy between the experimental data and the Fraunhofer pattern may be due to:

(i) the device 5A is not a typical Josephson junction as the coherence length ξ is much shorter than the length of the bridge L, or/and (ii) the influence of the RF or/and thermal noise on the measurements.

Other measurements for $I(V)$ characterises were performed at ultra-low temperature using the BlueFors dilution refrigerator. The results of these measurements are shown in Fig. 6.9(a). The temperature of the sample were roughly controlled up to 700 mK using the temperature control system incorporated with the BlueFors refrigerator. For comparison, the measurements are plotted together with those measured using the PPMS at $1.85 < T < 4.0$ K. This is shown in Fig. 6.9(b). It's quite obvious from the $I(V)$ that the ultra low temperature measurements are with much less noise. This probably due to the RF noise associated with PPMS measurements, which is not filtered out by the powder filter used in all measurements performed with the dilution refrigerator.

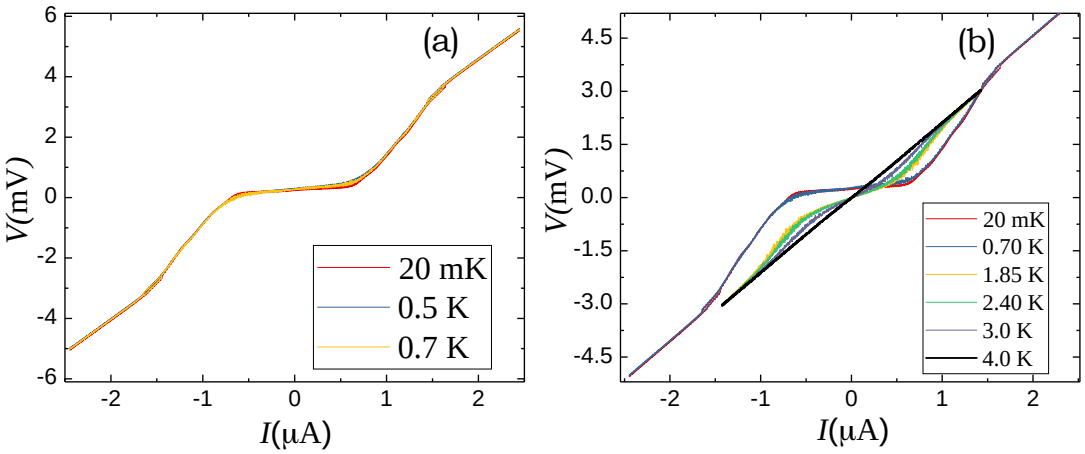

Figure 6.9: (a) Representative $I(V)$ characteristics measured at ultra-low temperature. (b) A comparison between the measurements performed at ultra low temperature and those performed using the PPMS at $T > 1.85$ K.

Differential resistance (dV/dI) measurements were performed at $T \approx 20$ mK using the setup shown in Fig. 6.6, in which an ac drive current is generated by the signal generator in the root mean square voltage (V_{rms}) mode to allow the lock-in to acquire the response of a dc coupling signal (i.e., a signal of ac and dc offset). The reference frequency of the lock-in amplifier and the frequency of the signal generator are both set at 17 Hz. The amplitude of the output signal generator was selected between 10 and 150 mV as given in the legend shown in Fig. 6.10. This allows to obtain the ac current passing through the terminals I^+ and I^- using $I_{ac} = \frac{V_{rms}}{R_{Load}}$, where R_{Load} is the load resistor shown in Fig. 6.6 which is about 1 MΩ. Thus, I_{ac} varies between 10 nA when $V_{rms} = 10$ mV, and 150 nA when $V_{rms} = 150$ mV[3]. The normalised differential resistance (dV/dI) can be obtained from the V_{rms} measured by the lock-in amplifier, and the I_{ac} current given earlier. Thus, the normalised differential resistance is given by $\frac{dV}{dI} = \frac{V_{rms}}{I_{ac}}$. This expression is applied on the non-normalised differential resistance measurements given in Fig. 6.10(a) to obtain

[3]Since the lock-in was set to acquire the response V_{rms}, and the output signal generator was also set in the V_{rms} mode, one should distinguish here between the V_{rms} measured by the lock-in, and the one generated by signal generator.

the normalised ones given in Fig. 6.10(b). Both V_{rms} and dV/dI shown in the figure have been potted versus the dc voltage measured by the voltmeter (Agilent 34460A). The reading of the voltmeter at the peak of the dV/dI curve reflects the superconducting gap, ($\Delta(T \approx 20$ mK). For device 5A, the dV/dI curve shown in Fig. 6.10 gives $\Delta(T \approx 20$ mK)= 2 meV. However, this gap slightly decreases as the drive current I_{ac} increases, which can be considered as a background noise that can significantly or slightly influences the measurements depending on I_{ac} amplitude.

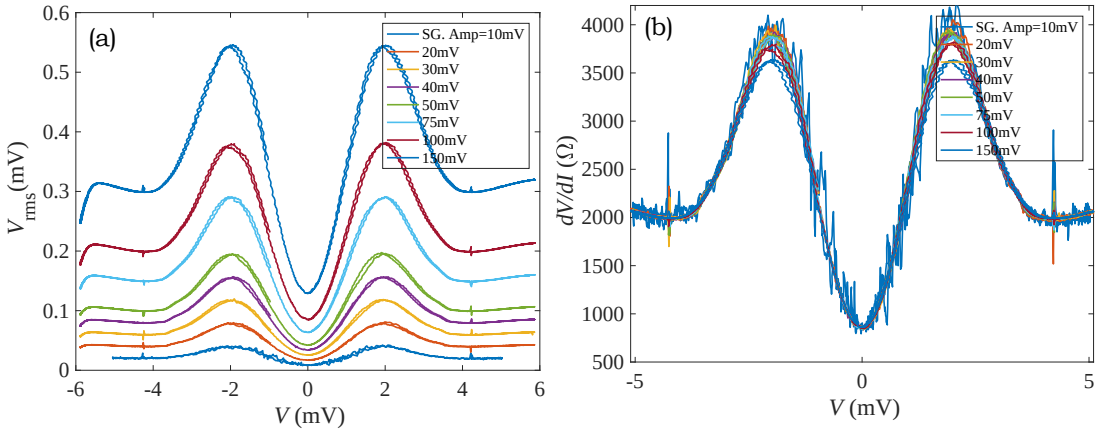

Figure 6.10: (a) Non-normalised , and (b) normalised differential resistance measurements of device 5A at $T \approx 20$ mK. The dV/dI measurements have been performed at various the signal generator amplitudes between 10 and 150 meV. The normalised dV/dI measurements show that the superconducting gap, $\Delta(T \approx 20$ mK), of the device is about 2 meV.

Device 2A

The $I(V)$ curves of device 2A where the bridge dimensions are: $W = 108$ nm, and $L = 78$ nm, were measured at different temperatures between 20 and 700 mK. Selected measurements shown in Fig. 6.11(a) which elucidates that increasing temperature up to 700 mK can slightly impact the $I(V)$ characteristic by a slight decrease in the critical current I_c. As the length of the weak link of device 2A is about eleven times of the reported coherence length, the sinusoidal current phase relationship given by Eq. 3.11 is far from matching the structure of the device. A structure with an arbitrary geometry has been described by Gor'kov, Eilenberger via what called quasiparticle theory discussed in Sec. 3.2.3.5. Thus, the Usadel equations may be numerically solved to provide an accurate current phase relationship for devices with $L \gg \xi_0$ such that given in Fig. 3.7.

A feature that can observed in the $I(V)$ curves of this device is highlighted in Fig. 6.11(b), where notable resistive steps in the transition region around I_c occur. As discussed in Sec. 2.5.1, such steps may be interpreted by propagating vortices and antivortices which are created on the edges of the sample, and overlap then at the center of the bridge where they annihilate, which finally results in phase slip lines (PSLs) with order parameter $|\psi|^2 \approx 0$. Such PSLs are discussed in some details in Sec. 2.5, using simulations on the basis of the time dependent Ginzburg Landau theory, shown in panels 4 and 7 of Fig. 2.7(c), and panel 4 of Fig. 2.8. Earlier experimental investigations that show such effect are discussed

in Sec. 2.5.2, where the steps shown in Fig. 2.9, have been attributed to PSLs described by Ginzburg Landau theory.
As all devices are made of the boron-doped nanocrystalline diamond (BNCD), the granularity associated with devices can have a significant impact on the $I(V)$ characteristics as it can lead to further phase slip events due to the instantaneous phase φ_{ij} of the wave functions ψ_{ij} tunnel through grain boundaries indicated by i and j. Such effect requires a further analysis in terms of the disordered superconductor films consisting of mesoscopic superconducting grains that can be considered as arrays of Josephson junctions which are briefly overviewed in Sec. 3.5.

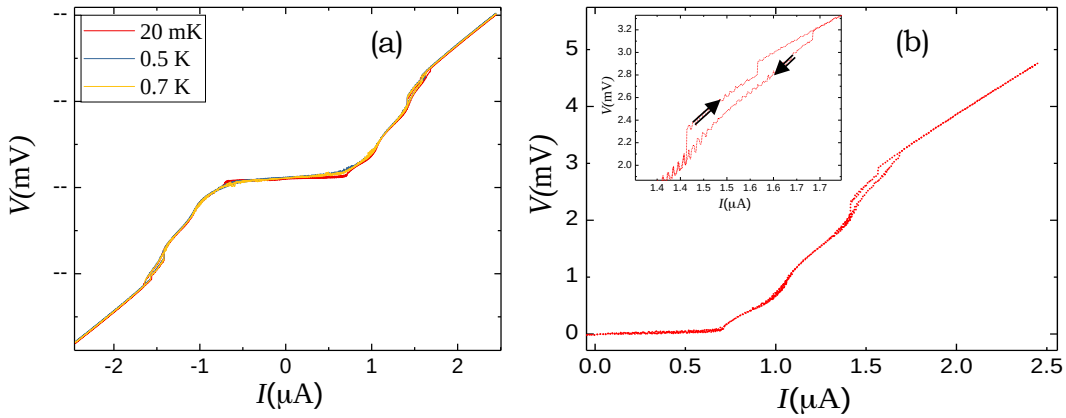

Figure 6.11: (a) Representative $I(V)$ characteristic of device 2A as measured at ultra-low temperature. (b) A close window for the resistive steps occur in the $I(V)$ curve in the transition region around I_c.

Following the same procedure used to measure normalised differential resistance (dV/dI) of device 5A, the differential resistance of device 2A was measured with reference frequency of 17 Hz, the amplitude of the output signal generator set between 10 and 500 mV, i.e., I_{ac} varies between 10 nA when $V_{rms} = 10$ mV and 500 nA.

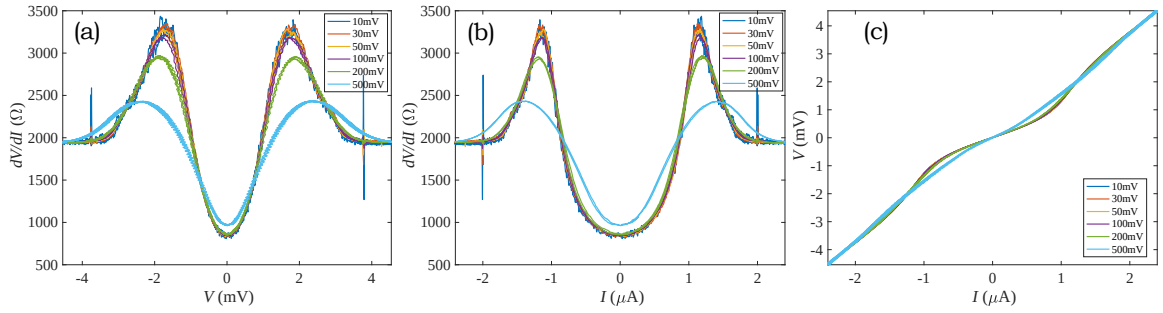

Figure 6.12: (a) The normalised differential resistance measurements of device 2A as plotted against the dc voltage of the device. (b) The corresponding differential resistance against the dc bias current, and (c) the corresponding $I(V)$ curves which are influenced by the ac current drive. The dV/dI measurements have been performed at various amplitude of the signal generator (in V_{rms} mode) between 10 and 500 meV, and show that the superconducting gap, $\Delta(T \approx 20$ mK) of the device, is about 1.8 meV.

Normalised dV/dI curves as measured against the dc voltage of the device are in shown in Fig. 6.12(a), and the corresponding curves obtained against the dc bias current are shown in Fig. 6.12(b). The corresponding $I(V)$ curves have been also extracted from the later two figures and plotted in Fig. 6.12(c), in which the influence of the ac current drive on the $I(V)$ curves is observed. As the peak of the dV/dI curve reflects the superconding gap Δ, the dV/dI curve shown in Fig. 6.12(a) gives $\Delta(T \approx 20$ mK$)= 1.8$ meV.

Device 1A

The $I(V)$ characteristics of device 1A, where the bridge dimensions are: $W = 105$ nm, and $L = 128$ nm, were measured at temperature between 20 and 700 mK. The selected measurements given in Fig. 6.13(a), show how the critical current I_c slightly decreases with increasing the temperature. Normalised dV/dI curves as measured against the dc voltage of the device are in shown in Fig. 6.13(c), and the corresponding curves obtained against the dc bias current, are shown in Fig. 6.13(d). The corresponding $I(V)$ curves have been also extracted from the later two figures and plotted in Fig. 6.13(e), where the influence of the ac current drive on the $I(V)$ curves can be observed. The peak of the dV/dI curve shown in Fig. 6.13(c) gives the superconding gap $\Delta(T \approx 20$ mK$)$ is about 1.9 meV.

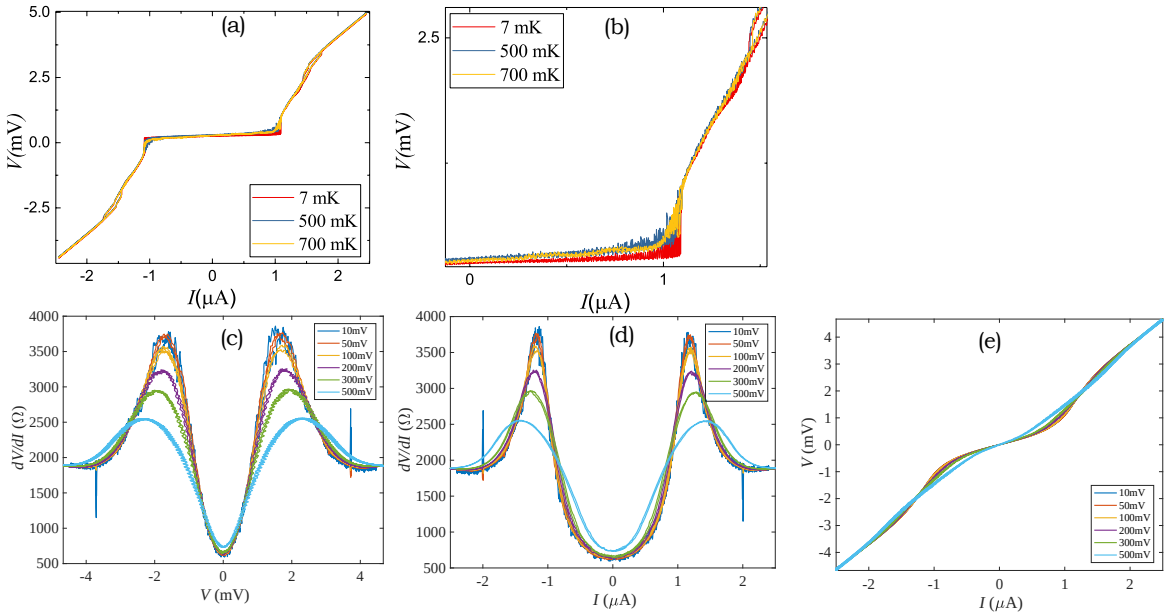

Figure 6.13: (a) Representative $I(V)$ characteristics of device 1A as measured at ultra-low temperature. (b) A close window for the $I(V)$ curve in the transition region around I_c. (c) The normalised differential resistance measurements of the device as plotted against the device voltage. (d) The corresponding differential resistance against the dc bias current, and (e) the corresponding $I(V)$ curves which influenced by ac current drive. The dV/dI measurements have been performed at various amplitude of the signal generator (in V_{rms} mode) between 10 and 500 meV, and show that the superconducting gap of the device is about 1.9 meV.

Comparison

In Fig. 6.14(a), the $I(V)$ curves measured for the three nanobridge devices at $T = 20$ mK are plotted together, and the critical current value of each device is plotted against it's geometry A/L in Fig. 6.14(b) in which A is the cross-sectional area of the device bridge, and L is it's length. The results given in Fig. 6.14(b), disagrees with Eq. 3.12 that describes the critical current of a typical Josephson junction where $I_c = \frac{e^*\hbar}{2m^*}|\Psi_0|^2\frac{A}{L}$. This disagreement is probably due the reasons demonstrated earlier, which are: (i) Eq. 3.12 is a spacial case that analytically obtained from Ginzburg Landau equation where L is comparable to ξ_0, such condition does not satisfy the geometry of all measured devices with $L \gg \xi_0$, (ii) the granularity of the device results in disorder effect, which may cause a further discrepancy with the typical Josephson junction behaviour, and (iii) vortices kinematics may influence the $I(V)$ curves as indicated in the resistive transition region around I_c in the $I(V)$ curve measured for device 2A.

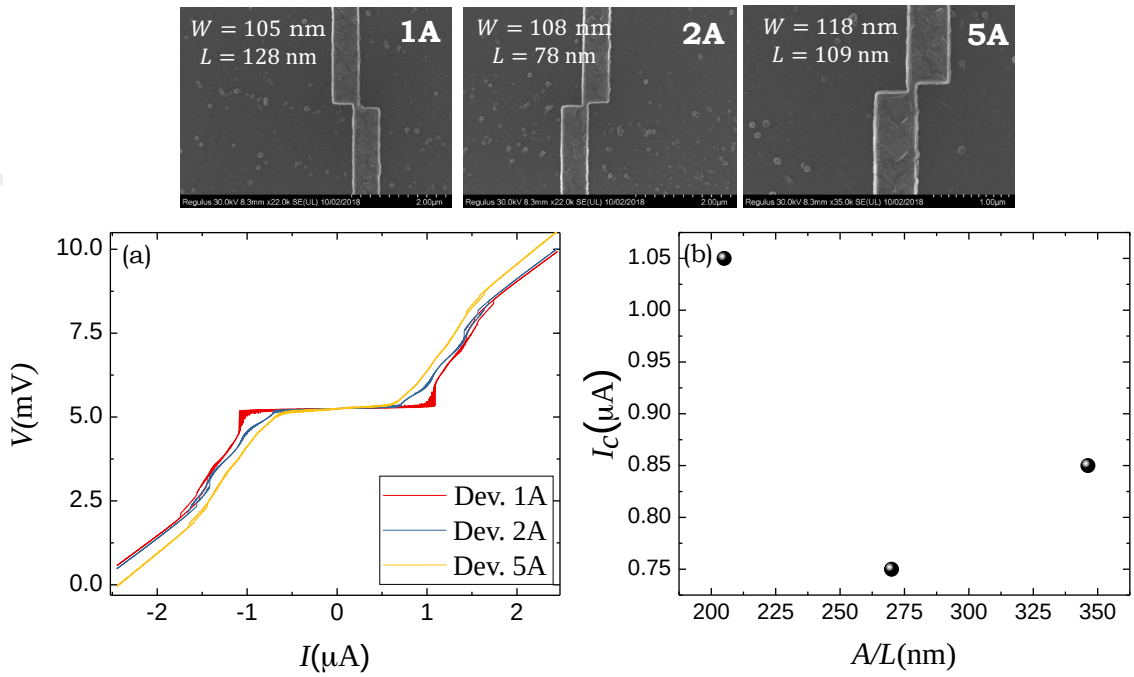

Figure 6.14: (a) Representative $I(V)$ characteristics of the three devices, 1A, 2A, and 5A, measured at ultra-low temperature. (b) The critical current I_c of each device against it's geometry A/L.

6.4 SIS Junctions measurements

The measurements presented in this section are those performed on the SIS Junctions, devices: 4A, 6A, and 8A shown in Fig. 6.1, where $I(V)$ characteristics and the differential resistance measurements (dV/dI) are reported.

Device 4A

As shown in Fig. 6.1, device 4A is with an insulator weak link with a vacuum gap of a 6 nm width. With such small value for the vacuum gap ($W < \xi_0$), the device is expected to behave as a typical SIS Josephson junction. Although such structure is extremely difficult to be fabricated, it has been accidentally performed.

A load of measurements have been performed for the device at about 20 mK, meanwhile, the device slowly died. In Fig. 6.15(a), only one of the $I(V)$ curves measured at temperature of about 20 mK is presented. As the vacuum gap of the device is short enough relative to the coherence length of diamond, where the sinusoidal current phase relationship given by Eq. 3.11, is perfect for such case, a fit to the RCSJ model is quite appropriate. In Fig. 6.15(b), the $I(V)$ curve is analysed in terms of the RCSJ model with the following parameters: $R = 5100\ \Omega$, $I_c = 1.72\ \mu$A, current noise $I_N = 0.05I_0$, and $C = 10$ pF. As the junction capacitance and/or the resistance are large, the screening parameter, $\beta_c = \frac{2\pi I_0 R^2 C}{\Phi_0} \gg 1$, which implies that the junction is underdamped. Thus, $I(V)$ curve shown in Fig. 6.15(a), exhibits a hysteresis loop.

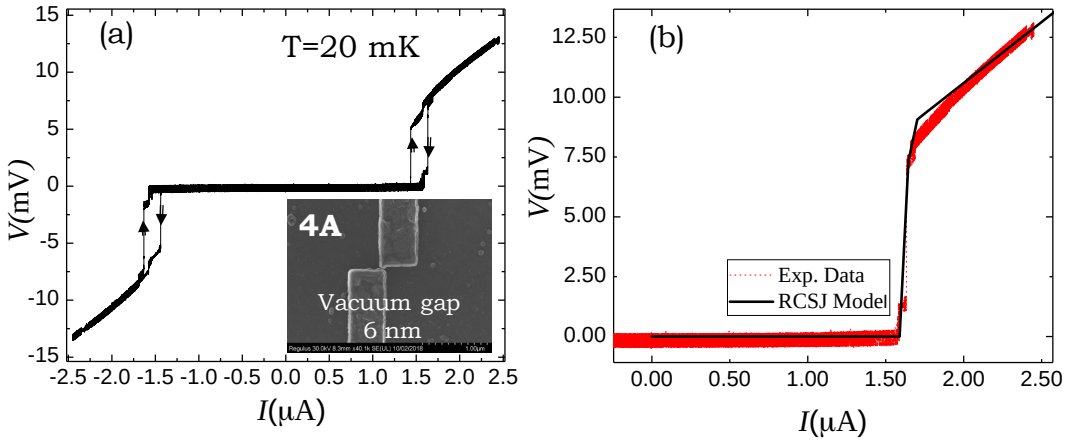

Figure 6.15: (a) An $I(V)$ curve of the device 4A with an insulator weak link of a 6 nm vacuum gap width. The measurement was performed at ultra-low temperature at about 20 mK. (b) The $I(V)$ curve as analysed in terms of the RCSJ model with fitting parameters: $R = 5100\ \Omega$, $I_c = 172\ \mu$A, current noise $I_N = 0.051I_0$, and $C = 10$ pF.

Device 6A

As shown in Fig. 6.16, device 6A with a vacuum gap of about 15 nm was investigated by measuring $I(V)$ characterises, and differential resistance at different amplitudes of ac current drive. In contrast to the previous behaviour exhibited for device 4A, device 6A shows a linear $I(V)$ characterises when the signal generator is turned off (dc measurements). However, when an ac current drive (with frequency of about 17 Hz) is applied, the $I(V)$ characterises becomes entirely nonlinear. Furthermore, the critical current depends strongly on the amplitude of the applied ac current. Such behaviour is not understood, and requires further investigations.

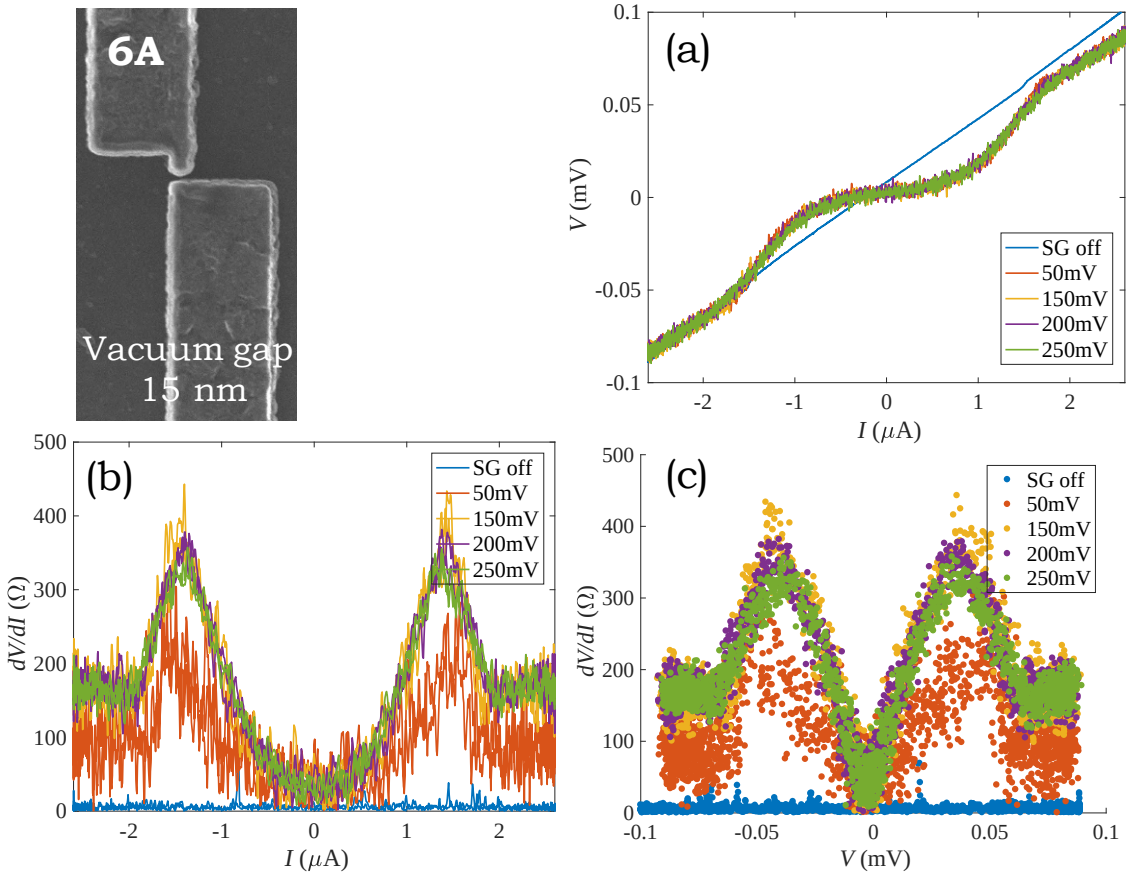

Figure 6.16: (a) $I(V)$ characteristics of device 6A of a 15 nm vacuum gap as measured at different ac-current amplitudes. When the signal generator is turned off (dc measurement), the measurements show a linear $I(V)$ curve, while the $I(V)$ characteristics become nonlinear when an ac current drive is applied. (b) and (c) The corresponding differential resistance measurements.

Device 8A

Interesting results were observed for device 8A with a 76 nm vacuum gap. Fig. 6.17 shows the temperature dependence of $I(V)$ characteristics, and differential resistance measurements performed using the experimental setups schematically illustrated in Figs. 6.5, and 6.6 respectively. As shown in the figure, the bias current for device 8A reaches 120 μA. As a thermal energy is generated when the bias current passes through the device, a high bias current causes a technical issue in keeping the temperature constant during the measurement. As demonstrated earlier in Sec. 6.2.3.1, this problem was solved using a PID controller where the feedback of the thermometer acquired by the AVS bridge is used to adjust the output of the second current source that feeds the heater. A result which examines the function of the PID controller codes, is shown in Fig. 6.17 (b), where the the PID controller was successfully used to keep the temperature constant at $T = 2$ K during the time period in which the bias current was increased from zero to 120 μA. Measurements for temperature dependence of $I(V)$ characterises were performed at $0.25 < T < 4.0$ K, and shown in Fig. 6.17(a). The corresponding unnormalised differential resistance measurements in terms of the dc voltage and dc current, were also performed using the experimental setup schematically illustrated in Fig. 6.6. The later measurements

are shown in Fig. 6.17 (c) and Fig. 6.17(d) respectively. The critical currents I_c were extracted from the $I(V)$ curves, or from corresponding differential resistance measured at different temperatures. The result of $I_c(T)$ is shown in Fig. 6.17(e) in which the critical temperature $Tc \approx 3.8$ K.

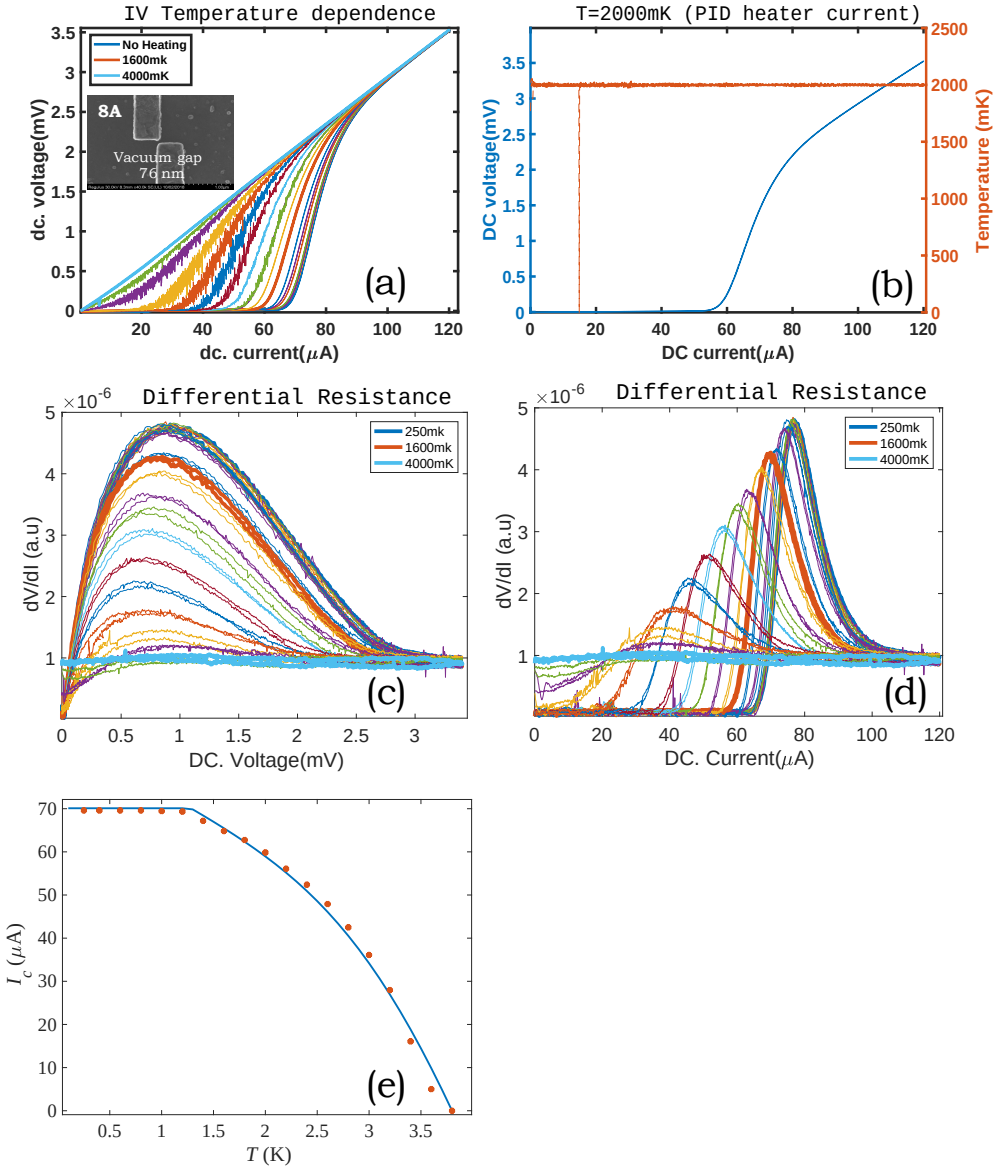

Figure 6.17: (a) $I(V)$ characteristics of device 6A of 76 nm vacuum gap as measured at different temperatures. (b) A selected measurement for $T - I$ curve (red line) which shows how temperature was successfully kept constant using the PID controller during the $I(V)$ curve measurement (blue line). (c) and (d) The corresponding differential resistance measurements in terms of the dc voltage and dc current respectively. (e) The temperature dependence of the critical current for the device (dots) as fitted in terms of Ambegaokar and Baratoff formula given by Eq. 3.48.

In Sec. 3.3.3, a study on the temperature dependence of the critical current for SIS junctions, was discussed in light of Ambegaokar and Baratoff formula [9, 10], where the $I(V)$ characteristics of SIS junctions, was described by the expression given in Eq. 3.47, and the critical current $I_c(T)$ is given by Ambegaokar and Baratoff formula [9] given by

Eq. 3.48. The experimental results of $I_c(T)$ were fitted according to this equation in which $\Delta_2(T) \approx \Delta_1(T) = \Delta(T)$, the gap $\Delta(T)$ is given by Eq. 2.67 where $\Delta(T) = A_1 1.764 k_B T_c$ when $T < 1.2$, and by Eq. 2.69 where $\Delta(T) = A_2 3.064 k_B T_c \sqrt{1 - T/T_c}$ when $T > 1.2$, where A_1 and A_2 are selected fitting parameters. The fit is plotted together with extracted critical currents in Fig. 6.17(e) in which the fitting parameters A_1 and A_2 are 2.086 and 1.47 respectively, and $G_n = 1/R_n$, with $R_n = 27\ \Omega$.

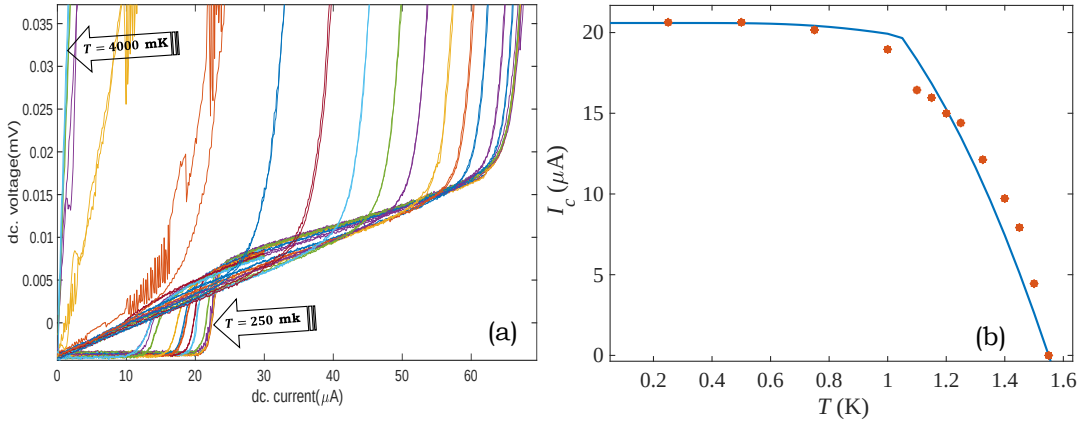

Figure 6.18: (a) A close view with a small window for the region around $I = 20$ A of the $I(V)$ curves of device 8A given in Fig. 6.17(a) in which another transtion (I_{c1}) occurs. (b) Temperature dependence of I_{c1} as obtained from the $I(V)$ curves.

Another interesting transition in the $I(V)$ curve was observed for this device at about $I = 20$ A and $T = 250$ K. This transition which indicated by I_{c1} was not observed in the $I(V)$ curves shown in Fig. 6.17(a) due to the large scale of the full $I(V)$ curve relative to the small window around I_{c1} in which such transition can be observed. The small window of the region around $I = 20$ A of the $I(V)$ curves given in Fig. 6.17(a) is shown in Fig. 6.18(a) in which I_{c1} transition is quite obvious. The figure shows a decrease in the transition current I_{c1} as the temperature increases up to $T = 1.6$ K at which such transition disappears. Temperature dependence of I_{c1} is obtained from the $I(V)$ curves, and plotted in Fig. 6.18(b). The I_{c1} transition may be described by Ambegaokar and Baratoff formula, from which the $I(V)$ curve can be obtained as that shown in Fig. 3.10(b), where two transitions in the $I(V)$ curve appear. The transition $I_{c1}(T)$ was fitted according to this equation Eq. 3.48. In which, where the gab $\Delta(T)$ for this transition is: $\Delta(T) = B_1 1.764 k_B T_c$ when $T < 1.0$, and by Eq. 2.69 where $\Delta(T) = B_2 3.064 k_B T_c \sqrt{1 - T/T_c}$ when $T > 1.0$, where fitting parameters B_1 and B_2 are 1.50, and 1.52 respectively. The fit is plotted together with extracted critical currents in Fig. 6.18(b), in which $G_n = 1/R_n$, with $R_n = 27\ \Omega$, and $T_{c1} = 1.55$ K.

6.5 Future work

So far, measurements for three nanobridge devices, and other three SIS junctions with vacuum gaps, have been performed. For a clearer picture about the properties of these devices discussed in terms of the theoretical background reviewed in the earlier chapters of this thesis, other temperature and magnetic field dependence measurements will be

performed on the devices shown in Fig. 6.19. The variety of these devices structures should allows testing the reproducibility of the earlier measurements which pave the way toward diamond SQUIDs, and finally allow implementing a micro or nano mechanical resonator in such SQUID loops. The future measurements will also examine the validity of theoretical interpretations of the devices behaviour discussed in Sec.5.3.2 and Sec. 5.3.3, as well as, will investigate features, such that shows resistive steps which occur around the transition region in the $I(V)$ curve of device 2A. Such feature can be interesting in terms of quantum phase slip junctions.

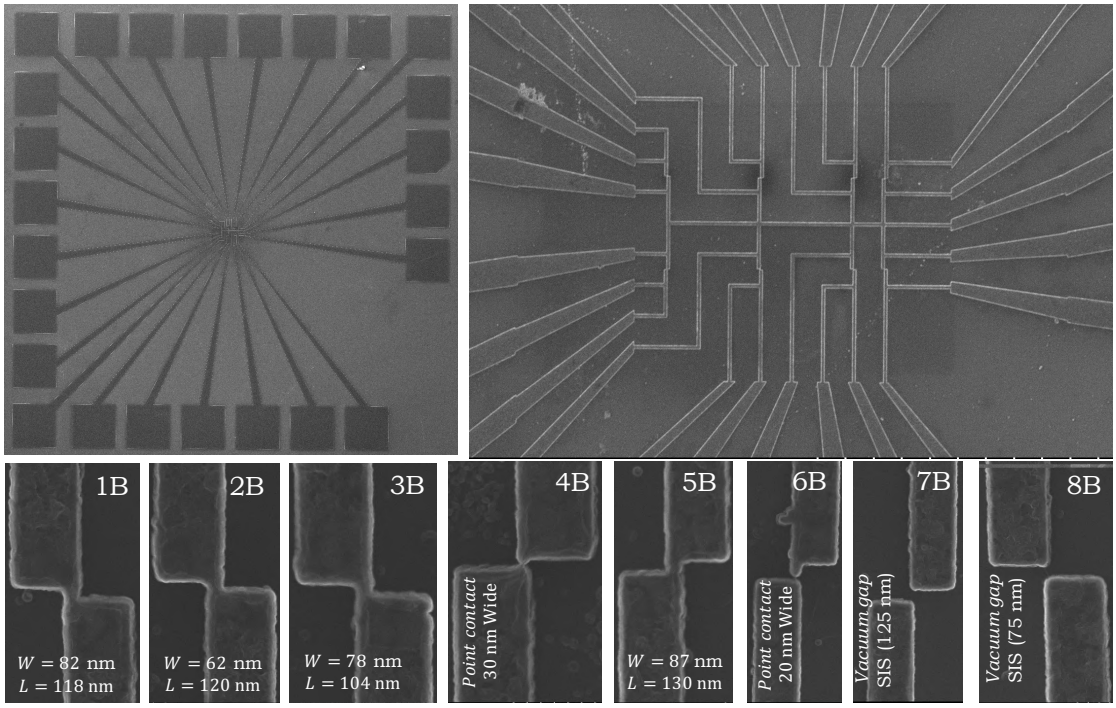

Figure 6.19: (top left) The chip in which devices with new structures have been integrated, and (top right) a closer view of the chip. (bottom) The new devices which are intended to be measured in the future.

6.6 Superconducting strips measurements

Other interesting superconducting devices made of boron doped nanocrystalline diamond (BNCD) can be developed on the basis of transport properties of superconducting strips. In general, such properties can be attributed to: (*i*) the formation of phase slip lines caused by kinematic vortices discussed in Sec. 2.5, (*ii*) LAMH theory & SBT model discussed in Sec. 2.4.1, and 2.4.2 respectively, and (*iii*) granular effect that can be modelled as an array of Josephson junctions such that briefly discussed in Sec. 3.5. This section is specified for experimental investigations of the superconducting strips with the structures given in table. 6.1. $I(V)$ characteristics, and $R(T)$ curves were measured for all these strips and discussed in terms of kinematic vortices, LAMH theory, and SBT model.
The strips were grown on a 100 silicon substrate with a 500 nm thick SiO_2 buffer layer. Nanodiamond particles of 5 nm diameter have been used as seeds in the MPCVD growth

process. Finally, the devices were prepared by standard top down optical photolithography processing and oxygen plasma etching through a metal mask.

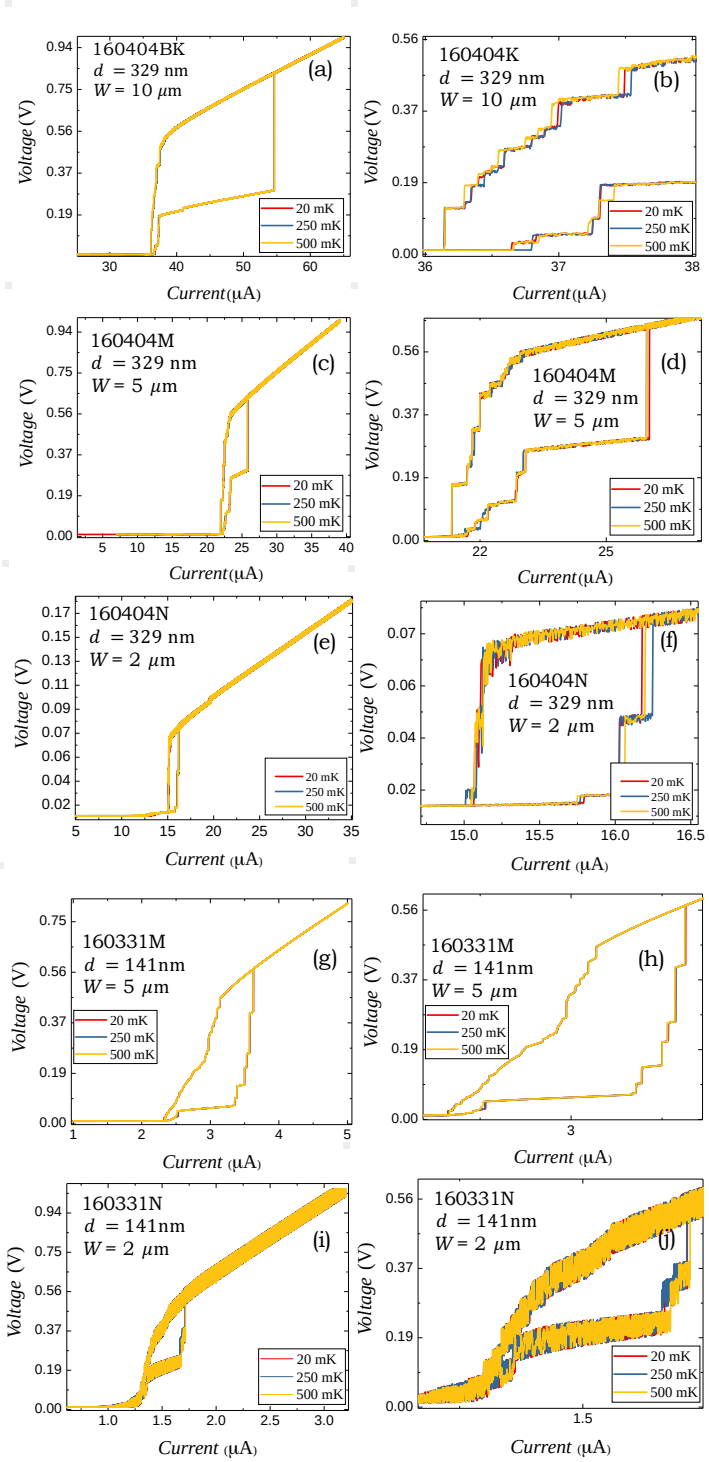

Figure 6.20: (a) $I(V)$ characteristic of superconducting strips with lengths, widths, and thickens given in the table. 6.1. (b), (d), (f), (h) and (j) are close views for (a), (c), (e), (g), and (i) around transition regions respectively.

The $I(V)$ curves shown in Fig. 6.20, were measured in the dilution fridge at ultra low temperatures between 20 and 500 mK. The transport properties show obvious hystereses

with finite discrete voltage steps in the transition regions around critical currents. An interpretation for these steps can be presented by phase slip lines entering the strips from the edges and overlapping in the middle of these strips. Such interpretation was supported by numerical simulations of the time-dependent Ginzburg Landau (TDGL) theory discussed in Sec. 2.5 and shown in Figs. 2.7 and 2.8. According to those calculations, an increase in the applied current results in a larger nucleation rate of vortex-antivortex pairs, and causes a finite transition in the $I(V)$ curves. A further increase causes a new transition in the $I(V)$ curve, which finally leads to the multiple discrete voltage steps in the resistive arm of the $I(V)$ curves such that previously measured for the strips given in table. 6.1. Previous experimental work, by which the $I(V)$ curves have been measured are shown in Fig. 2.9.

Sample name	Thickness(nm)	Width(μm)	Length(mm)
1160404BK	329	10	1
1160404BM	329	5	1
1160404BN	329	2	1
160331M	141	5	1
160331N	141	2	1

Table 6.1: The structures of the measured superconducting strips.

Fig. 6.21(a) presents the $I(V)$ properties of each stripe, with 10 and 5 or 2 μm width, 329 or 141 nm thickness, and 1 mm length. The change in the number successive resistive domains when the width and thickness changes, can be linked to the thermal effects which depends on the cross-sectional area of the stripe. Furthermore, this change can be quantitatively interpreted using the TDGL equations which describe the oscillations of the order parameter propagating in form of waves across the stripe which has been denoted by kinematic vortices. Thus, further calculations are still needed to fully map out the influence of the stripe geometry on the transport properties of the strips. Computationally, for a long stripe (1 mm length) such calculations can be challenging as the stripe must be divided into grids with size of the coherence length of the superconducting diamond which is about 10 nm. More details about numerical solution of TDGL equations have been demonstrated in Sec. 2.2.4.

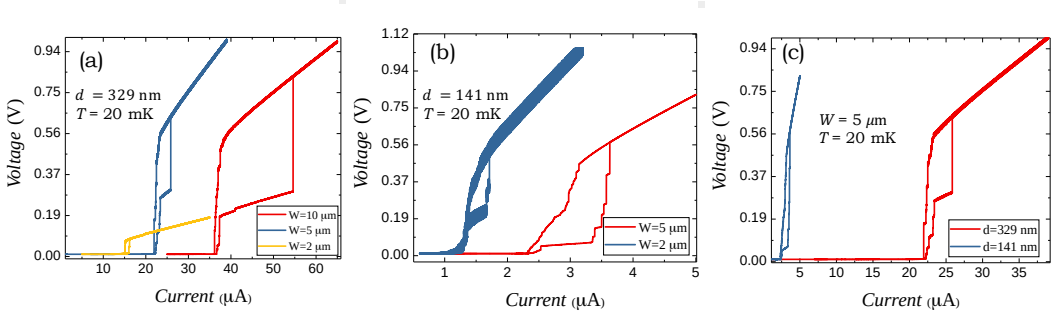

Figure 6.21: The dependence of $I(V)$ characteristics of strips of 1 mm length on their widths, and thickens.

Temperature dependence of the strips resistance, $R(T)$ curves, were measured, and the

results are shown in Fig. 6.22. For all strips, the $R(T)$ curves show spikes in the superconducting regions, where the temperature is below the critical temperature. The well observed spikes appear in the $R(T)$ curves measurements do not constantly occur at same point in the $R(T)$ curves [apart from the result obtained for the stripe (160404N) shown in Fig 6.22(f)].

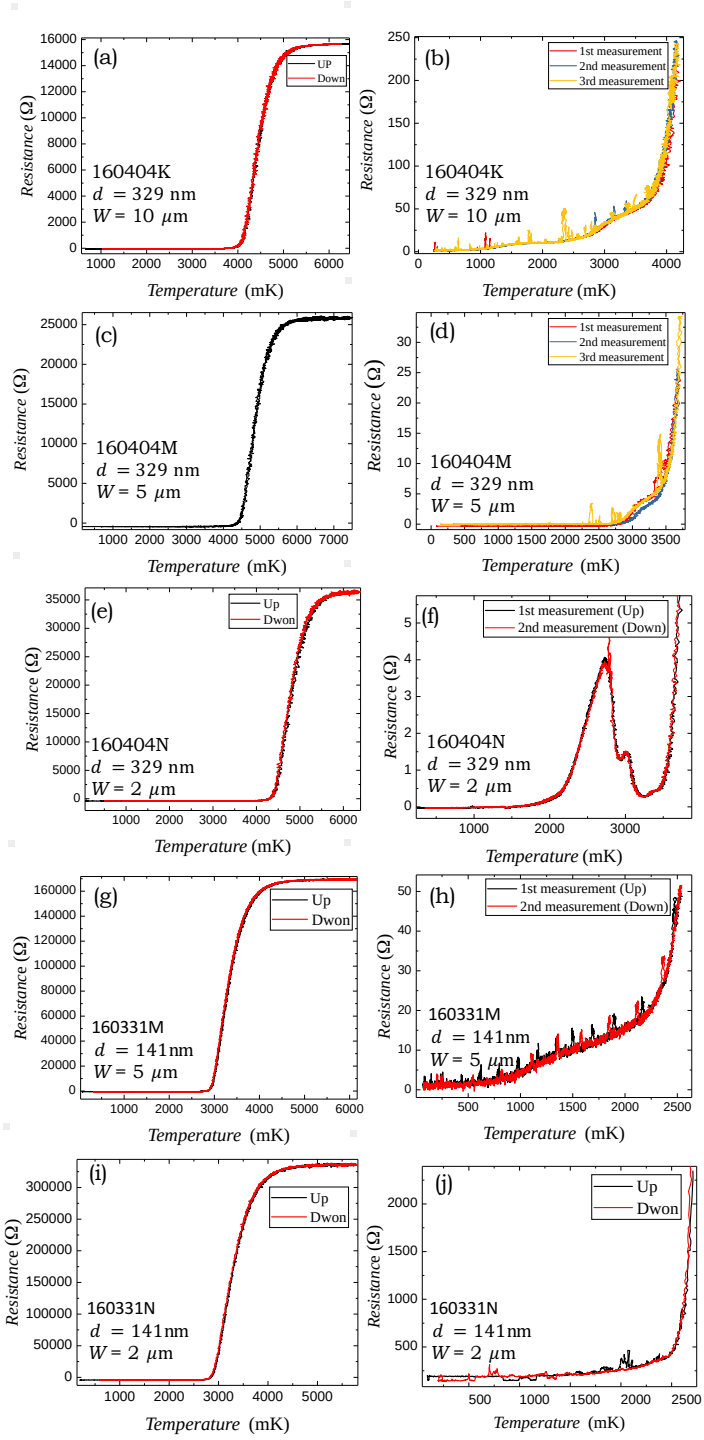

Figure 6.22: (a) $R(T)$ curves of superconducting strips with lengths, widths, and thickens given in the table. 6.1. (b), (d), (f), (h) and (j), are close views for (a), (c), (e), (g), and (i) for the regions in which $T < T_c$ respectively.

The instability of these spikes can be attributed to the rapid motion of vortices and antivortices which nucleate at the opposite outer boundaries and move toward the middle of the sample where they annihilate. Such rapid motion causes instantaneous hot spots in the strips where the order parameter ($|\psi|^2 \approx 0$) which finally appears as spikes occur in the $R(T)$ curves. In other words, the time evolution of the hot spots existence may explain the instability of the spikes as they shift their positions in the $R(T)$ curve by remeasuring it. Regarding to the peak occurs around 2.5 K of the $R(T)$ curve measured for the stripe (160404N), and shown in Fig. 6.22(f), that is stable by changing the bias voltage, may be explained by assuming that the speed of vortices and antivortices move across the stripe is relatively low compare to other strips. With such assumption the nucleation of vortices and antivortices in an equilibrium situation for longer period of time which leads in average to a stable spike in the $R(T)$ curve. However, calculations on the biases of the TDGL theory are required to confirm this assumption.

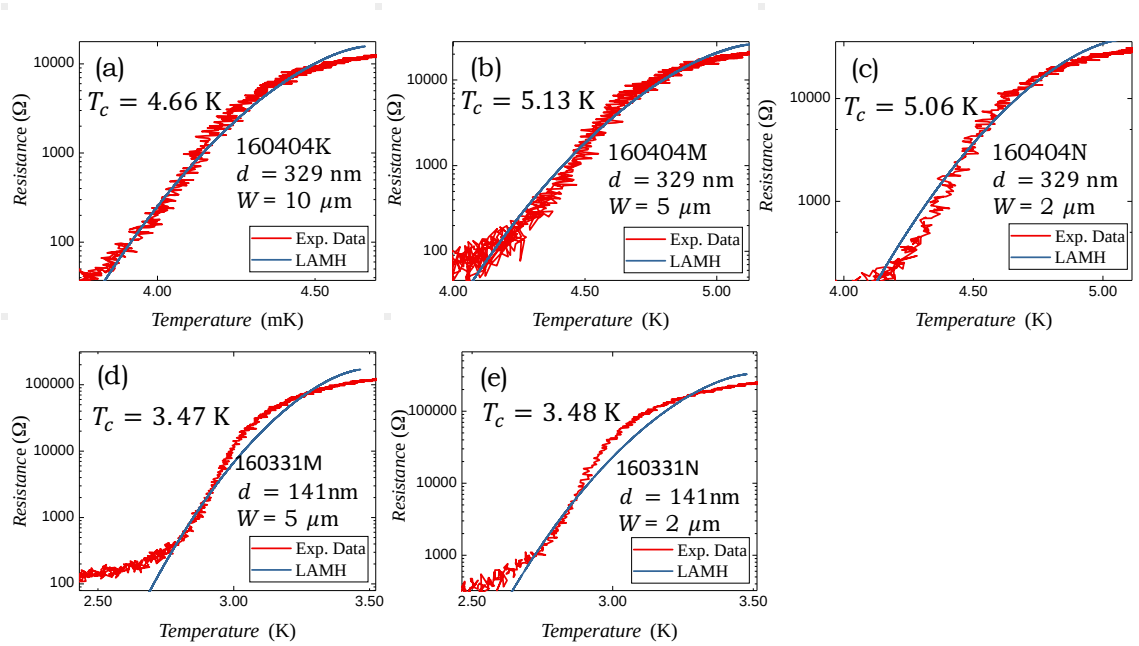

Figure 6.23: (a) The $R(T)$ curves in the vicinity of the transition regions, with $T < T_c$, and the performed fittings as obtained on the basis of thermally activated phase slips (TPS) extended from LAMH theory.

$R(T)$ curves can be analysed in terms of LAMH theory dissussed in Sec. 2.4.1, where the order parameter fluctuates to zero at certain points along long and thin superconducting wire. This allows the phase to slip by 2π, which results in resistive steps around transition regions of the $I(V)$ curves. Within this frame, the temperature dependence of the wire resistance is described by Eq. 2.79, which also has been modified to estimate the contribution of thermally activated phase slips (TPS) by Eqs. 2.80 and 2.81. These equations have been used to fit the $R(T)$ curves given in Fig. 6.22. The fittings have been performed in the vicinity of the transition regions, with $T < T_c$. The fitting lines are shown in Fig. 6.23, in which, an obvious discrepancy between the $R(T)$ measurements and these lines obtained in terms of LAMH theory can be observed. This can be an indication that LAMH theory is not sufficient to interpret the transport properties of the strips described in table. 6.1. In Fact, LAMH theory is more appropriate for a wire that is nearly a typical

1D system. As such system does not precisely apply on the measured strips, a further consideration is presented here using SBT model dissuaded in Sec. 2.4.2. SBT model was extended for wider superconducting wires, or quasi 1D systems, in which, a small and nonzero voltage is generated at the edges of the wire due to thermal fluctuations and/or quasiparticle diffusion. Thus, the phase increases until instantaneously slips by 2π. As consequence of phase-slip centres (PSCs) that considered as a source for dissipation and fluctuations. The extrapolation for slopes of the linear part following the resistive steps occur around the transition region in the $I(V)$ curve of the strips and described by Eq. 2.82, converge to a nonzero current I_s at zero voltage. For the measured strips described in table. 6.1, the extrapolation for slopes of the linear part following the resistive steps occur of the $I(V)$ curves, are obtained and shown in Fig. 6.24.

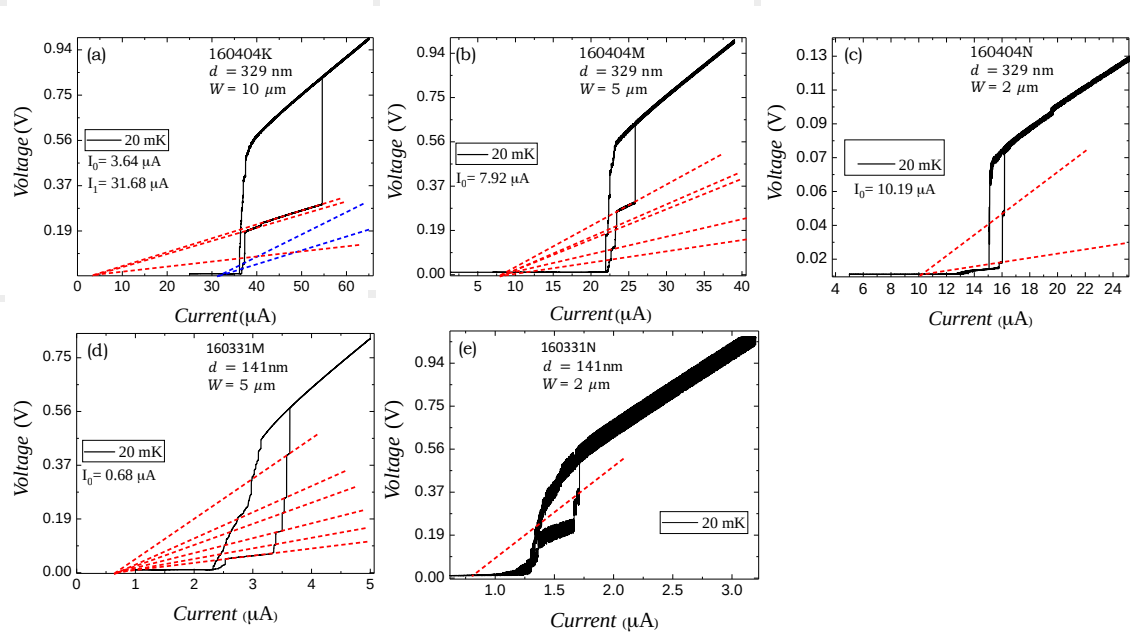

Figure 6.24: The extrapolation for slopes of the linear part extended from the resistive steps occur in the $I(V)$ curves of the measured strips. The thickness (d), and the width (W) of the strips are labelled in the legend.

The $I(V)$ curves show single intercept, with I_0 = 7.92, 10.19, 0.68, and 0.63 μA for the strips respectively labelled by (b), (c), (d), and (e) given in Fig. 6.24, and two intercepts I_0= 3.64, and I_1= 31.68 μA for the strip labelled by (a). As the strips (a), (b) and (c) are all have same thickness, the variation in the interception points that is observed for the strip (a), and the strips (b) and (c) on the other side, is probably because of the width of the strip (a) which is two times larger than the width of strip (b), and five times larger than the width of stripe (b). The impact of the width in this case can be due to the superconducting grains. As a granular system can be quantitatively considered as array of Josephson junctions, where phase slip events can be created as briefly discussed in Sec. 3.5. The phase slip events emerged due the superconducting grains may lead to resistive steps such that appear in the $I(V)$ curves measured for the strips described in table. 6.1. Overall, the resistive steps observed around transition regions of the $I(V)$ curves, could be due to a collective effect described by kinematic vortices, thermal fluctuations and/or quasiparticles diffusion (SBT model), and the granular effect of the superconducting di-

amond films from which the strips have been made. Computationally, for wide and long strips relative to the coherence lengths such these presented in this section, performing such comprehensive model that involves all these effects, is challenging.

Bibliography

[1] Heaney, Michael B. "Electrical conductivity and resistivity." The measurement, instrumentation and sensors handbook (2000): 1332-1345.

[2] Quantum and Design, Physical Property Measurement System AC Measurement System (ACMS) Option User's Manual. California, United States: Author, 4th ed., 2003.

[3] B. Cryogenics Ltd, BF-LD400 Cryogen-Free Dilution Refrigerator System–User Manual (2013)

[4] Instruments, Zurich. "Principles of lock-in detection and the state of the art." CH-8005 Zurich, Switzerland, Accessed (2016).

[5] Likharev, K. K. "Superconducting weak links." Reviews of Modern Physics **51**.1 (1979): 101.

[6] Kupriyanov, M. Yu, and V. F. Lukichev. "Proximity effect in electrodes and the steady-state properties of yosephson SNS structures." Fizika Nizkikh Temperatur **8**.10 (1982): 1045-1052.

[7] Watanabe, M., *et al.* "Stacked SNS Josephson junction of all boron doped diamond." Physica C: Superconductivity and its applications **470** (2010): S613-S615.

[8] Delin, K. A., and A. W. Kleinsasser. "Stationary properties of high-critical-temperature proximity effect Josephson junctions." Superconductor Science and Technology **9**.4 (1996): 227.

[9] Ambegaokar, Vinay, and Alexis Baratoff. "Tunneling between superconductors." Physical Review Letters **10**.11 (1963): 486.

[10] Seidel, Paul, ed. Applied superconductivity: handbook on devices and applications. John Wiley Sons, 2015.

7 Cantilevers Implemented in a dc. SQUID

Based on the superconducting quantum interference device (SQUID) equations described by the resistively- and capacitively-shunted junction model coupled to the equation of motion of a damped harmonic oscillator, simulations to quantitatively describe the interaction between a dc SQUID and an integrated doubly clamped cantilever were performed. To investigate an existing experimental configuration and the motion of the cantilever and the reaction of the SQUID as a function of the voltage-flux $V(\Phi)$ characteristics were explored. With these simulations the Lorentz force back-action interaction was clearly observed, and how a sharp transition state drives the system into a nonlinear-like regime, and modulates the cantilever displacement amplitude, simply by tuning the SQUID parameters have been demonstrated. The Simulations presented in this chapter were published in Journal of Applied Physics [1].

7.1 SQUID-suspended cantilever system: introduction and an earlier experiment

Theoretical and experimental studies [2, 3, 4, 5, 6, 7, 8] of linear and nonlinear micro and nanomechanical resonators are of great interest as they can be used for sensitive force and displacement measurements. The physical parameters of the resonators can also be tuned to observe the transition from the classical to quantum regimes with relative experimental ease, enabling observations of macroscopic quantum systems[9]. Significant experimental progress in the detection of resonators as they enter the quantum ground state has been achieved by capacitive coupling to superconducting flux qubits[10], and quantum state control of a mechanical drum resonator in a superconducting resonant circuit has been achieved by phonon-photon coupling [11, 12]. The state detection is an integral part of any coupled resonator system as the coupling mechanism is implicit in any experimental endeavour.

Previous experiments have used a dc SQUID to detect the motion of a suspended doubly clamped cantilever integrated directly into a SQUID loop [2, 13], and for a torsional SQUID cantilever [14]. A suspended doubly clamped cantilever integrated directly into a SQUID loop as experimentally demonstrated by Etaki *et al* [2], is shown in Fig. 7.1, where the cantilever displacement is out-of-plane, and the applied magnetic field, B, is in-plane. In this experiment, a stripline current shown in Fig. 7.1(a) is used to tune the flux through the loop which enables to obtain $V(\Phi)$ curves such that shown in Fig. 3.14(b). When a cantilever is embedded in a SQUID loop, the flux through the loop depends on the position of the fundamental out-of-plane mode of the cantilever as: $\Phi = \Phi_{\text{ext}} + aB\ell u$, where Φ_{ext}

is the applied flux when the cantilever is in its equilibrium position, a is a geometrical factor that depends on the mode shape, B is the applied magnetic field, ℓ is the length of the cantilever, and u is the cantilever displacement. To make the SQUID sensitive enough to detect an extremely small change in the magnetic flux caused by the motion of the cantilever, a working point with the steepest slope of $V(\Phi)$ is selected where the responsivity of the cantilever-SQUID system ($\frac{dV}{du}$) maximizes. The Etaki's experiment has been performed at $I_b = 2.0I_b$, and $\Phi_{ext} = 0.25\Phi_0$ as the difference between the minimum and maximum (the peak-to-peak voltage) of the SQUID $V(\Phi)$ is maximized, and the cantilever- SQUID system becomes more sensitive. The frequency of the fundamental mode of the cantilever as experimentally investigated by the room-temperature dynamic force microscopy [2] is $f_0 = 2$ MHz. This frequency is located by driving the cantilever with a piezo actuator and monitored by the detector. The resulting output voltage of the dc-SQUID shown in Fig. 7.1(b), exhibits the resonance frequency that reflects the fundamental mode confirmed by dynamic force microscopy.

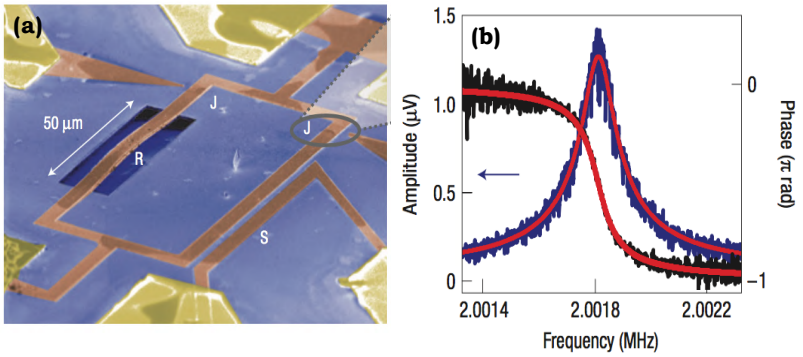

Figure 7.1: (a) The micromechanical cantilever embedded in the dc SQUID demonstrated by Etaki *et al* [2], where (R) is a doubly clamped cantilever, (S) is a stripline current used to change the flux bias through the loop, and (J) are a Nb–InAs weak links. (b) The cantilever response at $T = 20$ mK, and $B = 100$ mT. The amplitude and phase data are shown in blue and black respectively, and red lines are the Lorentzian fit of the amplitude and the phase response.

7.2 The back-action

Back-action is a feedback of the system variables from and to each others. In Fig. 7.2, a chart is used to demonstrate how the variables of the system, influence each others, and be influenced by the others. The interaction between these variables occurs in a sequential, loop and results in a shift in the cantilever frequency Δf and it's quality factor ΔQ. Considering a doubly clamped cantilever, it is obvious that as the cantilever oscillates the displacement changes, and the transduction technique will cause a back-action that influences the cantilever position [15]. The impact of back-action can be positive in terms of cooling [4] and squeezing the resonator motion [16, 17, 18], and coupling and synchronising multiple resonators [19, 20]. Depending on the specific transduction technique, back-action can be due to radiation pressure[21], electron tunnelling [22], or photothermal effects [23]. For the SQUID-based transduction scheme, the back-action has a simple inductive component caused by the Lorentz force due to the circulating current

[14, 13, 24]. Experimentally, the Lorentz back-action was shown to shift the mechanical cantilever resonant frequency and quality factor by Δf and ΔQ respectively.

To understand the effect of back-action on Δf and ΔQ, two transfer functions were obtained [13], which are coefficients for the average circulating current expanded in the terms of the cantilever displacement, u, and velocity, $\dot{u}$. In previous work, however, it was not possible to obtain the velocity-dependent transfer function in the frame of the SQUID equations coupled to the equation of motion of the doubly clamped cantilever. To simplify this issue, Poot *et al*[13] modulated the flux change in the SQUID loop caused by the cantilever oscillation. Subsequently, the total flux in the SQUID loop was assumed to be a function of the externally applied flux, Φ_{ext}, and the modulation of the flux due to the changing area of the loop, $\Phi \rightarrow \Phi_{\text{ext}} + \Phi_{\text{mod}} \cos(\omega_{\text{mod}} t)$. Such a modulation can describe the influence of the back-action on Δf and ΔQ of the cantilever when the SQUID displacement detector is tuned within limited regions of the $V(\Phi)$ curve [13].

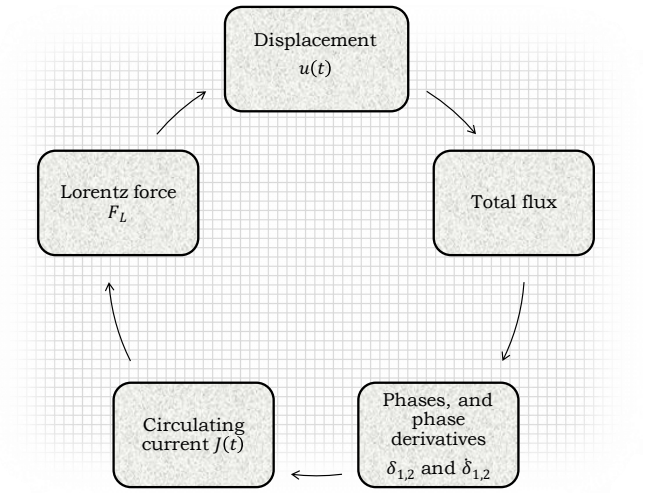

Figure 7.2: A chart that demonstrates the back-action effect, by which the of the SQUID-cantilever system variables influence each others, and be influence by the others..

However, a full description of the SQUID-cantilever interaction requires a comprehensive model to provide information not only about the influence of back-action in all regions of $V(\Phi)$, but also about the amplitude, width, line shape, and responsivity, $\frac{\mathrm{d}V}{\mathrm{d}u}$, which must be calculated by linking the cantilever displacement to the SQUID voltage. Thus, the need for quantitative treatments of the unscaled SQUID equations coupled explicitly to the equation of motion for the integrated beam becomes important. Though such treatments are complicated and challenging,[25] they can be performed numerically with improving computational capabilities. In this chapter, simulations for the interaction between a dc SQUID and an embedded micromechanical doubly clamped cantilever as experimentally demonstrated by Etaki *et al* [2] and shown schematically in Fig. 7.3(a) are presented. The SQUID-cantilever interaction is analysed in different regions of the $V(\Phi)$ curve, as shown in Fig. 7.3(b). Within this framework, some regions of the $V(\Phi)$ curve have been explored, where the SQUID-cantilever response is apparently strongly nonlinear. Furthermore, the back-action and the subsequent response of the SQUID is linked to the cantilever displacement. The effect of changing the SQUID operating point is discussed in depth, and it is demonstrated that the SQUID itself can be used to control the cantilever response by simple modification of the controllable SQUID parameters.

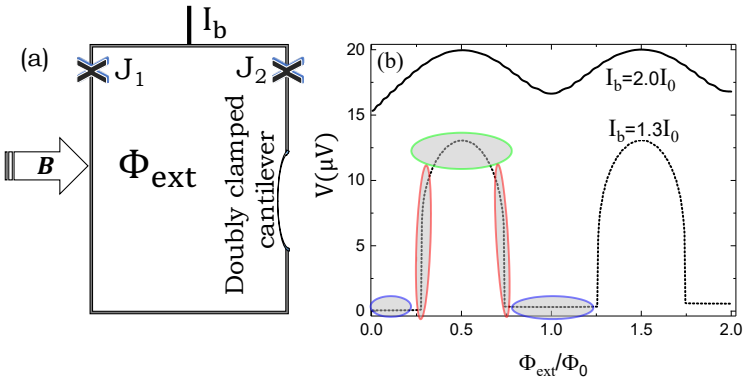

Figure 7.3: (a) Scheme for the dc SQUID displacement detector in which the two Josephson junctions are labelled by J_1 and J_2. The cantilever displacement is out-of-plane, and the applied magnetic field, B, is in-plane. (b) The voltage flux $V(\Phi)$ characteristics for a dc SQUID with $\beta_L = 0.115$ and $\beta_C = 1.61$. Four regimes are identified: (i) the simple oscillatory regime where the bias current, $I_b = 2.0I_0$. When $I_b = 1.3I_0$, other regimes are identified, those are: (ii) the rapidly changing regime (red), (iii) the zero voltage response regime (blue), and (iv) the intermediate regime (green).

7.3 The model

The model presented in this thesis is based on the experimental parameters of Etaki *et al* [2] to allow for experimental verification of the results. Thus, the equation of motion of a damped harmonic oscillator given in [13] is used to describe the displacement, $u(t)$, of the mechanical cantilever:

$$m\ddot{u} + \frac{m\omega_0}{Q_0}\dot{u} + m\omega_0^2 u = F_d(t) + F_L(t), \tag{7.1}$$

where m is the beam mass, $\omega_0 = 2\pi f_0$ is the intrinsic frequency, Q_0 is the quality factor, $F_d = F_0\cos(\omega_0 t)$ is the driving force, and $F_L(t)$ is the Lorentz force $F_L(t) = aB\ell(I_b/2+J)$. Here, B is the in-plane magnetic field, ℓ is the length of the cantilever, J is the circulating current, and $a = 0.91$ [2] is a geometrical factor that depends on the mode shape. Eq. (7.1) is coupled to the dc SQUID equations given by the resistively- and capacitively-shunted junction (RCSJ) model [26]:

$$\frac{\Phi_0}{2\pi}C\ddot{\delta_1} + \frac{\Phi_0}{2\pi}\frac{1}{R}\dot{\delta_1} + I_0\sin(\delta_1) = \frac{1}{2}I_b + J, \tag{7.2}$$

$$\frac{\Phi_0}{2\pi}C\ddot{\delta_2} + \frac{\Phi_0}{2\pi}\frac{1}{R}\dot{\delta_2} + I_0\sin(\delta_2) = \frac{1}{2}I_b - J, \tag{7.3}$$

$$\delta_1 - \delta_2 = 2\pi\cdot\Phi_{\mathrm{tot}}/\Phi_0, \tag{7.4}$$

where $\delta_{1,2}$ are the phase differences of the junctions, Φ_0 is the flux quantum, I_b is the bias current, I_0 is the critical current. The total flux, Φ_{tot}, has three contributions: (i) the external flux Φ_{ext}, (ii) the flux due to the circulating current, J, flowing through the inductance of the loop, L, and (iii) the change in flux through the loop due to the

cantilever displacement, $aB\ell u$. Therefore, $\Phi_{\text{tot}} = \Phi_{\text{ext}} + LJ + aB\ell u(t)$, and Eqs. (7.1 - 7.3) are coupled via the circulating current as $J = \frac{1}{L}(\frac{\delta_1 - \delta_2}{2\pi}\Phi_0 - \Phi_{\text{ext}} - aB\ell u)$.

These coupled differential equations are numerically solved without averaging the SQUID voltage and circulating currents, or scaling the time. Therefore, the time span $T_{\max}$ must be large enough to be suitable for the cantilever, while the time step $\mathrm{d}t$ must be small enough to resolve the impact of the fast changes dominated by the relatively high SQUID characteristic frequency $\omega_c = \frac{2\pi RI_0}{\Phi_0}$. Although this can be computationally expensive for cantilevers with very low frequencies relative to ω_c, the experimental results of Etaki *et al* [2] allow their experiment to be modelled within a relatively small time window.

Here, a system for identical experimental conditions demonstrated by Etaki *et al* [2] with $f_0 \simeq 2$ MHz is solved. To calculate the time dependent voltage, $V = \Phi_0\frac{\dot{\delta_1} + \dot{\delta_2}}{2\pi}$, the Runge-Kutta method (RK4) was used to numerically integrate the equations presented above. The SQUID response was then obtained in the frequency domain by evaluating the Fourier transform of the SQUID voltage and the cantilever displacement. The calculations were performed for $I_0 = 0.7\ \mu$A, $R = 29.5\ \Omega$, $B = 111$ mT, $C = 0.91$ pF, and $L = 170$ pH. These values give a McCumber-Stewart parameter $\beta_C = \frac{2\pi I_0 R^2 C}{\Phi_0} = 1.61$ and a screening parameter $\beta_L = \frac{2I_0 L}{\Phi_0} = 0.115$. The cantilever has a length $\ell = 50\ \mu$m, a mass $m = 6 \times 10^{-13}$ kg, and was assumed to have a resonant frequency $f_0 = 2.0018$ MHz and a quality factor $Q_0 = 25000$, giving a cantilever lifetime of $\tau_0 = \frac{Q_0}{\pi f_0} \simeq 4$ ms. The piezo drive which controls F_d is used only to locate the eigenmodes and is turned off during measurement [14]. Thus, at $t = 0$, the initial velocity $v_0 = \frac{\mathrm{d}u}{\mathrm{d}t}\Big|_{u=u_0} = 0$, where u_0 is the initial displacement amplitude. Here, $u_0 = 20$ pm.

The time span chosen for these calculations was $T_{\max} = 25$ ms, i.e. more than six times the lifetime of the cantilever, and the optimised time step chosen was $\mathrm{d}t = 0.0125$ ns. This value of $\mathrm{d}t$ allows resolution of the forces which are dominated by the SQUID frequency $f_c = \frac{RI_0}{\Phi_0} \simeq 10$ GHz. The calculations were repeated at different values of normalised flux in the range $0.90\Phi_0 \leq \Phi_{\text{ext}} \leq 0.05\Phi_0$, and bias currents in the range $2.0I_0 \leq I_{\text{b}} \leq 1.10I_0$. In the frequency domain, the selected frequency steps $\mathrm{d}f = 12.5$ Hz. The units of the response which were calculated directly from a Fourier transform are V·s for the unnormalised SQUID voltage and $\mathrm{m} \cdot \mathrm{s}$ for the unnormalised cantilever displacement. To convert the units of the voltage-response from V·s to V, the response was multiplied by $\frac{1}{\tau}$, where τ is the lifetime of the cantilever, which is related to the full width at half maximum (FWHM) as $\frac{1}{\pi\tau} = f_{\text{FWHM}}$. A similar procedure was used to convert the units of the displacement-response from m·s to m. With the β_L and β_C values presented earlier, the $V(\Phi)$ characteristics of an overdamped dc SQUID are shown in Fig. 7.3(b) to demonstrate the possible operating points of a SQUID displacement detector. The $V(\Phi)$ curves are calculated using the time-scaled SQUID equations described by the RCSJ model. In Fig. 7.3(b), four different regimes in the SQUID $V(\Phi)$ response are defined: (*i*) the simple oscillatory regime where the bias current, $I_b = 2.0I_0$. The other regimes are (*ii*) the rapidly changing regime (red), (*iii*) the zero voltage response regime (blue), and (*iv*) the intermediate regime (green). The analysis covers the interaction between a dc SQUID and an integrated cantilever when the system is tuned to operating points within these defined regimes, and the resulting effect on the cantilever-SQUID dynamics.

7.4 Results

7.4.1 The simple oscillatory regime

As experimentally demonstrated [2], the voltage responses exhibit Lorentzian distributions and for $\Phi_{ext} = 0.25\Phi_0$, i.e. the highest SQUID sensitivity for $I_b = 2.0I_0$ shown in Fig. 7.3(b), there was no relative experimental shift in Δf of the cantilever.

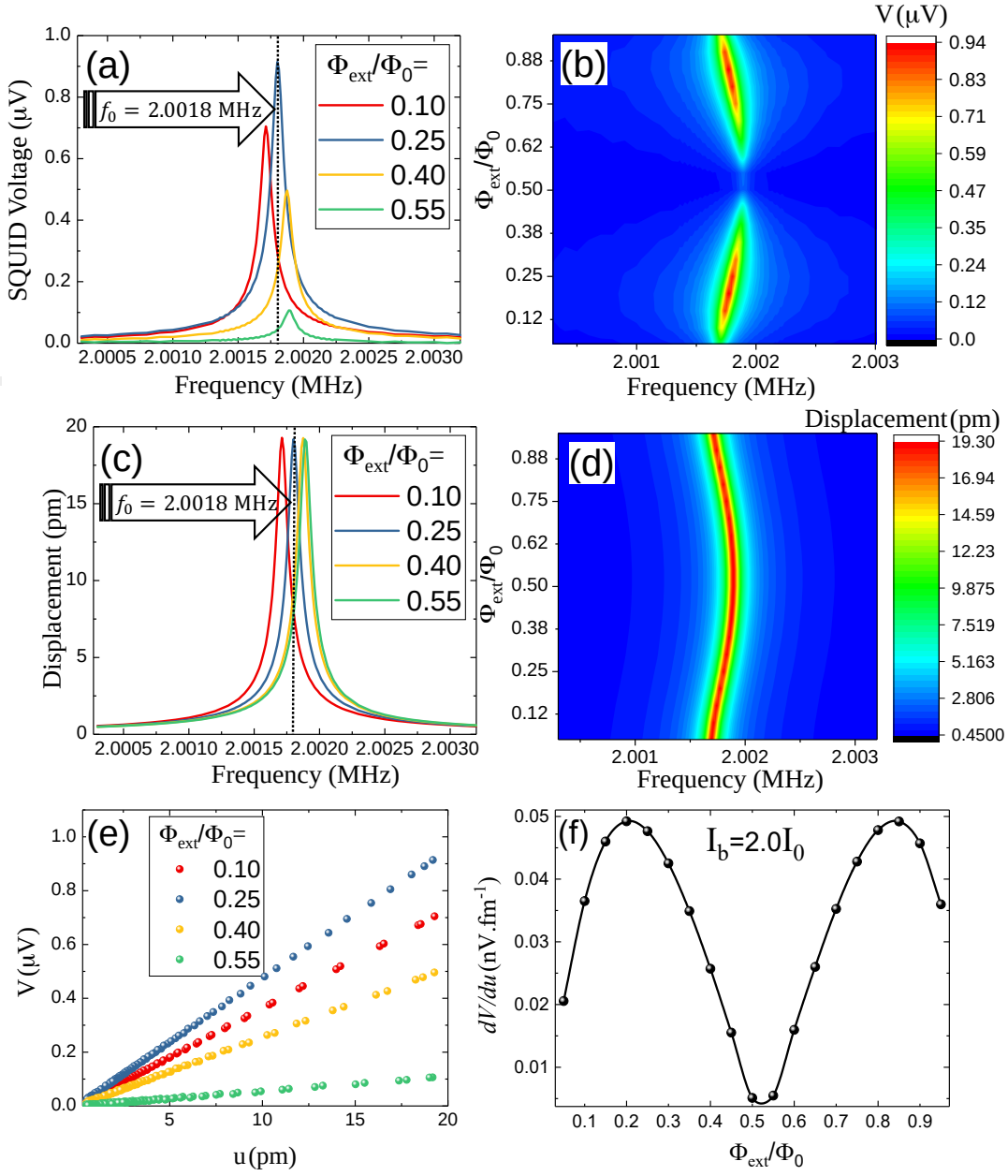

Figure 7.4: Line shapes for (a) SQUID voltage (V) and (c) cantilever displacement (u) calculated as a function of Φ_{ext} for $I_b = 2.0I_0$. (b) and (d) density plots for SQUID voltages and cantilever displacement respectively. (e) The linear displacement-voltage trace as extracted by linking (b) and (d) via the frequency. (f) The responsivity ($\frac{dV}{du}$) as calculated from the slopes of the displacement-voltage lines.

Changing the operating point of the SQUID by changing Φ_{ext} within the simple oscillatory region shown in Fig. 7.3(b) affects Δf, and the operating point clearly affects the sensitivity to the SQUID voltage as clearly shown in Fig. 7.4(a) and (b). Moreover the subsequent cantilever displacement is also affected [Fig. 7.4(c) and (d)]. These results clearly demonstrate the influence of the Lorentz back-action on the resonator from the SQUID displacement detector, and the expected magnitude of change in the experimental variables. The cantilever displacement and SQUID voltage are explicitly linked in the frequency domain, i.e., the displacement $u(f)$ is parametrically linked to the voltage $V(f)$. The subsequent analysis was performed at $I_b = 2.0I_0$ and $0.05\Phi_0 \leq \Phi_{\text{ext}} \leq 0.95\Phi_0$, and the displacement-voltage trace is plotted in Fig. 7.4(e). The traces show a linear dependence of voltage on displacement, which allows determination of the cantilever position in a responsivity specified by the slope of the displacement-voltage lines. Consequently, the responsivity ($\frac{\mathrm{d}V}{\mathrm{d}u}$) was calculated at $I_b = 2.0I_0$ for different Φ_{ext} values, with the result shown in Fig. 7.4(f). The figure shows a sinusoidal behaviour for $\frac{\mathrm{d}V}{\mathrm{d}u}$ which varies from 4.7×10^{-2} nV $\cdot$ fm^{-1} at $\Phi_{\text{ext}} = 0.25\Phi_0$ to 0.5×10^{-2} nV $\cdot$ fm^{-1} at $\Phi_{\text{ext}} = 0.50\Phi_0$. Importantly, Fig. 7.4 shows an appropriate representation of the experimental results by Etaki *et al* [2], thereby demonstrating a good computational model.

7.4.2 The intermediate regime

Further calculations were performed through the $V(\Phi)$ curve identified in Fig. 7.3(b) to examine the SQUID-cantilever coupling and explore the system response as the back-action is modified. Fig. 7.5(a)-(f) shows Δf, the FWHM, and the SQUID voltage as the bias current and Φ_{ext} are tuned. The largest frequency shift corresponds to the smallest gradient ($\frac{\mathrm{d}V}{\mathrm{d}\Phi}$) of the working point. This can clearly be understood by Eq. 7.1, where the frequency of the cantilever is controlled by the displacement coefficient. As the cantilever frequency is shifted by changing Φ_{ext} and I_b, a modification in this coefficient emerges due to the circulating current dependence on u. Such a dependence was previously analysed by expanding the circulating current in terms of the displacement, u [13]. In this way, the new displacement coefficient, which arises from the back-action of the SQUID current on the cantilever, modifies the frequency and causes a slight or significant shift depending on Φ_{ext} and I_b.

The Lorentz back-action also affects the cantilever quality factor; FWHMs of simulated line shapes are extracted and presented as a function of Φ_{ext} for various values of I_b in Fig. 7.5(c) and (d). The variation of the FWHM can be interpreted in an identical way to that of Δf, where the only difference being that FWHM $= \frac{\omega_0}{2\pi Q_0}$ is given in terms of velocity coefficient in Eq. 7.1. Thus, the FWHM is modified if J is assumed to have a dependence on the velocity in addition to the displacement which modifies the frequency [13]. The corresponding peak voltage, V_{max}, dependence on Φ_{ext} and I_b is shown in Fig. 7.5(e) and (f). The behaviour of V_{max} as a function of Φ_{ext} is consistent with $\mathrm{d}V/\mathrm{d}\Phi_{\text{ext}}$ of the SQUID $V(\Phi_{\text{ext}})$ curve shown in Fig. 7.3(b).

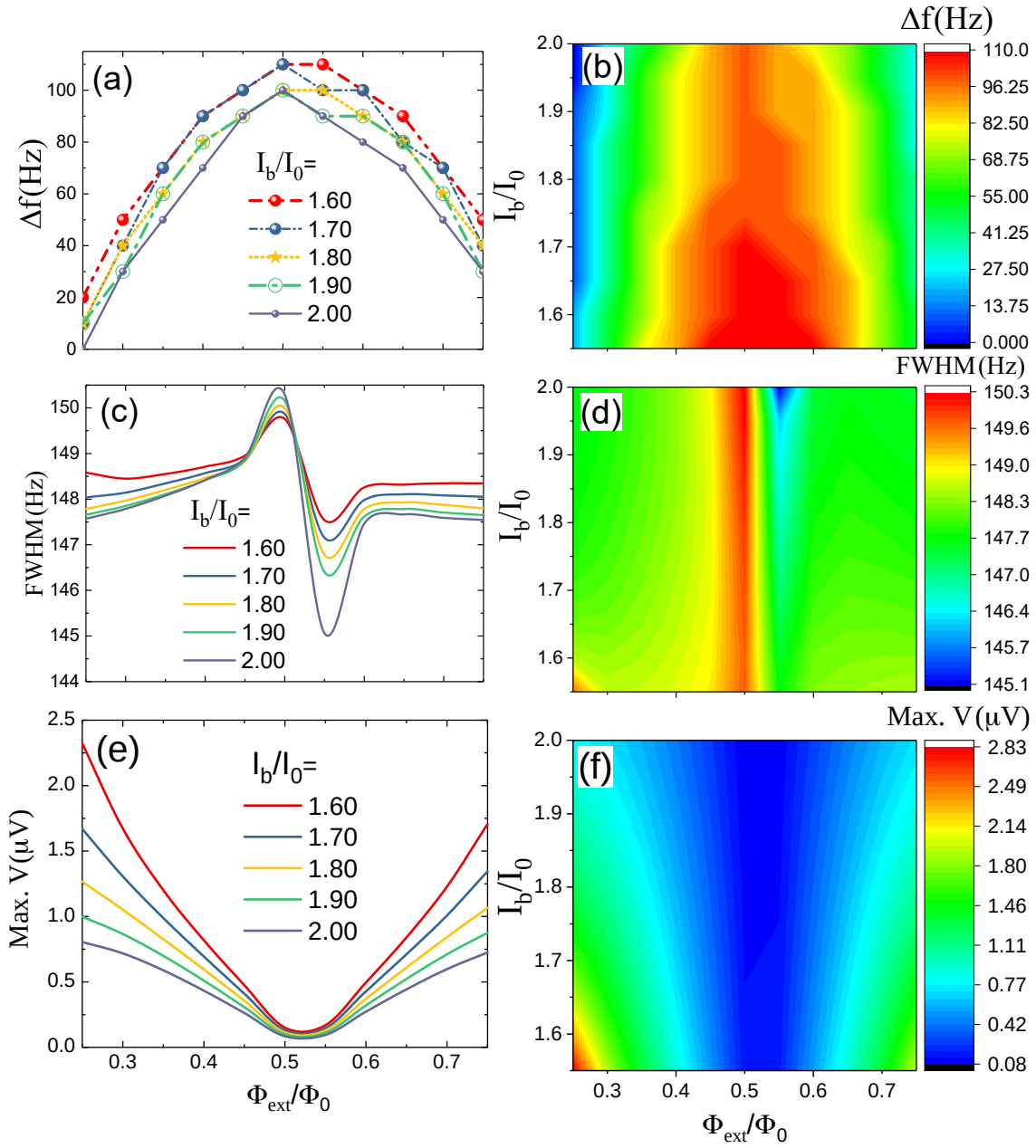

Figure 7.5: Calculations for the range $0.75\Phi_0 \leq \Phi_{\text{ext}} \leq 0.25\Phi_0$ and $2.0\text{I}_0 \leq I_{\text{b}} \leq 1.55\text{I}_0$ for (a) the frequency shift, Δf, (c) FWHM and (e) the maximum SQUID voltage, V_{max}. The corresponding density plots are shown in (b), (d), and (f) respectively.

7.4.3 The rapidly changing regime

Now a different regime from Fig. 7.3(b) is discussed, where the largest effect of back-action on the cantilever is observed, and the SQUID response is apparently nonlinear. To examine the effect of back-action on the cantilever motion, a point in such region was selected as shown in the inset of Fig. 7.6(a). Subsequently, at $\Phi_{\text{ext}} = 0.30\Phi_0$ and $I_b = 1.20I_0$, the unnormalised cantilever displacement and corresponding unnormalised SQUID voltage response for various displacement amplitudes u_0, are obtained and plotted in Fig. 7.6(a) and Fig. 7.6(b). When $u_0 = 20$ pm, the cantilever appears to have a

nonlinear behaviour as demonstrated by the modified line shape of the cantilever and the SQUID response. Specifically, as the displacement is reduced from $u_0 = 20$ pm to $u_0 = 10$ pm to $u_0 = 5$pm, the change in the flux through the loop $aB\ell u_0$ is 0.05, 0.025 and $0.0125\Phi_0$ respectively. This drives the cantilever to experience regions of different flux responsivity, the closest regions to the point $(0.30\Phi_0, 1.20I_0)$ are: (i) the intermediate region, and (ii) the zero voltage response region [see Fig. 7.3(b)].

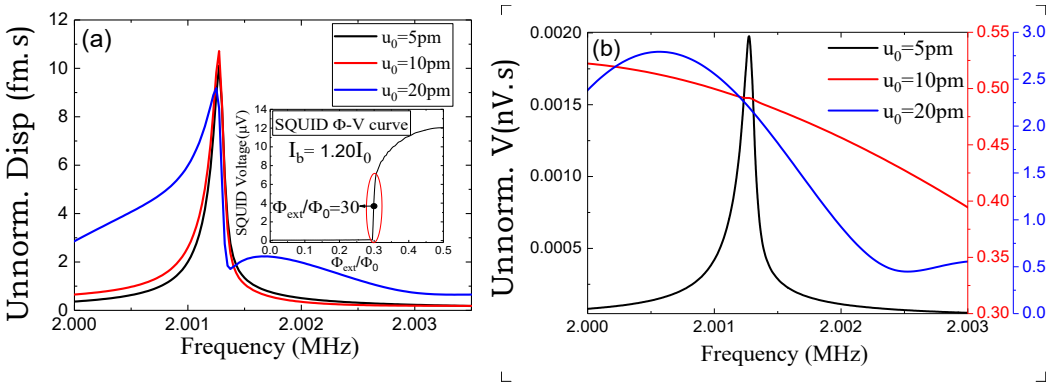

Figure 7.6: (a) Unnormalised displacement, and (b) corresponding unnormalised SQUID voltage when the SQUID displacement detector is tuned ($\Phi_{\text{ext}} = 0.30\Phi_0$ and $I_b = 1.20I_0$) to the working point shown in the inset of (a). The initial cantilever amplitudes are $u_0 = 20$ pm (blue), $u_0 = 10$ pm (red), and $u_0 = 5$ pm (black), which correspond to a change of flux in the SQUID loop of $0.05\Phi_0$, $0.025\Phi_0$, and $0.0125\Phi_0$ respectively. The colour coding is identical for both graphs.

Since the Lorentz force interacts with these two regions via the circulating current J, i.e., $F_L(t) = aB\ell(I_b/2 + J)$, two alternate and successive Lorentz forces of different driving modes emerge due to the back-action interaction. As a consequence of these irregular Lorentz forces, a temporary non-equilibrium state emerges, which causes a nonlinear like behaviour such as that shown in Fig. 7.6. Higher u_0, or more specifically higher $aB\ell u_0$, drives the cantilever to be influenced by a changing $V(\Phi)$ region where the responsivity $(\frac{\mathrm{d}V}{\mathrm{d}\Phi})$ becomes more significant. Thus, the variation in the unnormalised SQUID response becomes larger as can be clearly seen in Fig. 7.6(b). It should be noted, however, that as the cantilever returns to its dynamical equilibrium position, the response becomes more Lorentzian as expected.

The effect of the SQUID-cantilever interaction on the cantilever motion can be more clearly observed by comparing the time evolution of the cantilever displacement for two different bias and flux values. The time dependent displacement for $\Phi_{\text{ext}} = 0.25\Phi_0$ and $I_b = 2.0I_0$ is plotted in Fig. 7.7(a), and for $\Phi_{\text{ext}} = 0.30\Phi_0$ and $I_b = 1.20I_0$ in Fig. 7.7(b). Clearly if the SQUID operating point is in the rapidly changing regime [Fig. 7.7(b)], there is a sharp transition state as the cantilever returns to its equilibrium position. Naively, if the SQUID bias is switched when the cantilever motion is large, there is an instantaneous damping which can be used to modify the motion of the cantilever. Normal state positions, u_{N}, for specific lines around $\Phi_{\text{ext}} = 0.30\Phi_0$ and $I_b = 1.20I_0$ are shown in Fig. 7.7(c). These positions are extracted when the cantilever enters the normal state that accounts for the Lorentzian profile in the frequency domain, and when the amplitude starts decaying exponentially at time $t = t_{\text{N}}$, as shown in Fig. 7.7(b). A more

comprehensive analysis is presented in the density plot shown in Fig. 7.7(d). The plot given in Fig. 7.7(c) exhibits details for one of the yellow-blue islands in the density plot. The islands correspond to the intermediate regimes in the $V(\Phi)$ curves. Its anticipated that such effect could be employed to precisely and rapidly control the amplitude of the cantilever displacement below its initial amplitude which can be set by a piezo drive used to locate the eigenmodes of the cantilever. In other words, putting the system in such regions enables modulating the cantilever amplitude after isolating the system from the external actuator.

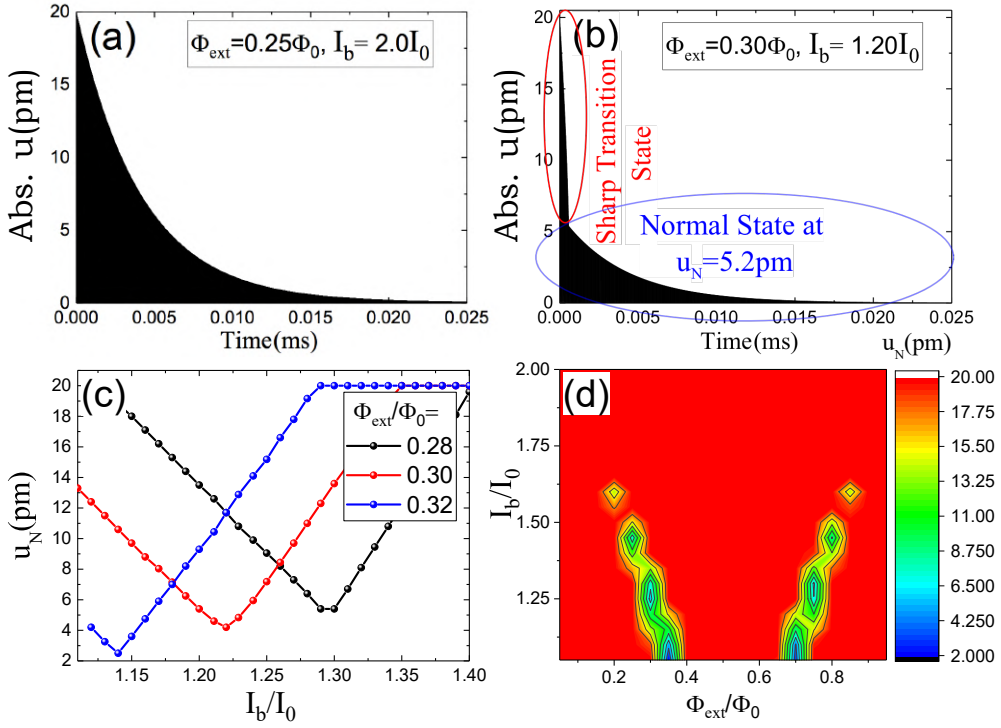

Figure 7.7: (a) Snapshot for the time array of cantilever displacements at (a) $\Phi_{\text{ext}} = 0.25\Phi_0$ and $I_b = 2.0I_0$ (a point in the simple oscillatory regime) versus (b) a point $\Phi_{\text{ext}} = 0.30\Phi_0$ and $I_b = 1.20I_0$ in the rapidly changing regime in which a sharp transition state emerges until the cantilever enters the normal state at $u = u_{\text{N}}$. (c) Calculations for the normal state positions of specific lines around $\Phi_{\text{ext}} = 0.30\Phi_0$ and $I_b = 1.20I_0$, and (d) the yellow-blue islands in the density plot indicate a shift in the normal state positions that starts emerging at $t = t_{\text{N}}$ and $u = u_{\text{N}}$. The opaque regions in (a) and (b) show the fast oscillations, which are unresolved due to time window plotted.

7.5 Future research

In conclusion, I have shown how the tuning of the SQUID device affects the back-action between the SQUID and the doubly clamped cantilever. Specifically, I have quantified the line shapes expected from the SQUID response and the corresponding cantilever displacement. The effect can be quantitatively analysed via the shift in the cantilever frequency, the line width, intensity, and shift in the position of the normal state. Direct

solutions for the unscaled dc SQUID equations coupled to the equations of motion of an integrated cantilever allow determination of voltage-displacement traces of a displacement detector. For a SQUID displacement detector tuned to a working point in the rapidly changing region, a sharp transition state emerges and a nonlinear-like response due to the emergence of such state is observed. This state could be used to employ the system as a self modulator for the displacement amplitude of the cantilever.

Finally it should be noted that the effect of thermal fluctuations were not investigated in the current work, and the system studied here is for SQUID devices with a typical Josephson junction behaviour, i.e, a sinusoidal current phase relationship (CPR). In general, the thermal noise can be estimated using the Langevin equation [27, 28, 29], where the noise $\eta(t)$ is given by a correlation function as $\langle \eta(t)\eta(t')\rangle = \frac{2K_BT}{R}\delta(t-t')$. However, the simulations performed in this paper are suitable for devices: (i) with junctions having dimensions (length L and/or width W) shorter than the coherence length (ξ) of the superconducting film, and (ii) measured in a dilution fridge below 50 mK, where the influence of the thermal noise is generally small. Future work can be extended to modify the differential equations given by RCSJ by adding a stochastic current term to estimate the effect of the thermal noise for higher temperatures devices and to implement CPRs such as that analytically described in [30], or those obtained [31, 29, 32] by numerically solving Ginzburg Landau equations for nanobridges with dimensions greater than ξ of the film.

Bibliography

[1] Salman, Majdi, *et al.* "Quantitative analysis of the interaction between a dc SQUID and an integrated micromechanical doubly clamped cantilever." JAP **125**.22 (2019): 224503.

[2] Etaki, S., *et al.* "Motion detection of a micromechanical resonator embedded in a dc SQUID." Nature Physics **4**.10 (2008): 785-788.

[3] Blencowe, M. P., and E. Buks. "Quantum analysis of a linear dc SQUID mechanical displacement detector." Physical Review B **76**.1 (2007): 014511.

[4] Naik, A., *et al.* "Cooling a nanomechanical resonator with quantum back-action." Nature **443**.7108 (2006): 193-196.

[5] Kirton, Peter George, and A. D. Armour. "Nonlinear dynamics of a driven nanomechanical single-electron transistor." Physical Review B **87**.15 (2013): 155407.

[6] Cohen, Guy Z., and Massimiliano Di Ventra. "Reading, writing, and squeezing the entangled states of two nanomechanical resonators coupled to a SQUID." Physical Review B **87**.1 (2013): 014513.

[7] Ella, Lior, *et al.* "Tunable strong nonlinearity of a micromechanical beam embedded in a dc-superconducting quantum interference device." Journal of Applied Physics **117**.1 (2015): 014309.

[8] Pugnetti, Stefano, *et al.* "Dynamics of a SQUID ratchet coupled to a nanomechanical resonator." Physical Review B **79**.17 (2009): 174516.

[9] Schwab, Keith C., and Michael L. Roukes. "Putting mechanics into quantum mechanics." Physics Today **58**.7 (2005): 36-42.

[10] O'Connell, Aaron D., *et al.* "Quantum ground state and single-phonon control of a mechanical resonator." Nature **464**.7289 (2010): 697-703.

[11] Teufel, John D., *et al.* "Circuit cavity electromechanics in the strong-coupling regime." Nature **471**.7337 (2011): 204-208.

[12] Rocheleau, T., *et al.* "Preparation and detection of a mechanical resonator near the ground state of motion." Nature **463**.7277 (2010): 72-75.

[13] Poot, M., *et al.* "Tunable backaction of a dc squid on an integrated micromechanical resonator." Physical review letters **105**.20 (2010): 207203.

[14] Etaki, Samir, *et al.* "Self-sustained oscillations of a torsional SQUID resonator induced by Lorentz-force back-action." Nature communications **4**.1 (2013): 1-5.

[15] Caves, Carlton M., *et al.* "On the measurement of a weak classical force coupled to a quantum-mechanical oscillator. I. Issues of principle." Reviews of Modern Physics

52.2 (1980): 341.

[16] Almog, Ronen, *et al.* "Noise squeezing in a nanomechanical duffing resonator." Physical review letters **98**.7 (2007): 078103.

[17] Zhang, Jing, Yu-xi Liu, and Franco Nori. "Cooling and squeezing the fluctuations of a nanomechanical beam by indirect quantum feedback control." Physical Review A **79**.5 (2009): 052102.

[18] Jähne, K., *et al.* "Cavity-assisted squeezing of a mechanical oscillator." Physical Review A **79**.6 (2009): 063819.

[19] Filatrella, Giovanni, Niels Falsig Pedersen, and Kurt Wiesenfeld. "High-Q cavity-induced synchronization in oscillator arrays." Physical Review E **61**.3 (2000): 2513.

[20] Cross, M. C., *et al.* "Synchronization by nonlinear frequency pulling." Physical review letters **93**.22 (2004): 224101.

[21] Kippenberg, Tobias J., and Kerry J. Vahala. "Cavity opto-mechanics." Optics express 15.25 (2007): 17172-17205.

[22] Steele, Gary A., *et al.* "Strong coupling between single-electron tunneling and nanomechanical motion." Science **325**.5944 (2009): 1103-1107.

[23] Jourdan, Guillaume, Fabio Comin, and Joël Chevrier. "Mechanical mode dependence of bolometric backaction in an atomic force microscopy microlever." Physical review letters **101**.13 (2008): 133904.

[24] Shevchuk, Olga, Rosario Fazio, and Ya M. Blanter. "Multistability of a Josephson parametric amplifier coupled to a mechanical resonator." Physical Review B **90**.20 (2014): 205411.

[25] The supplementary Information: S. Etaki, F. Konschelle, Ya. M. Blanter, H. Yamaguchi, and H. S. J. van der Zant, Nat. Commun. **4** 1803 (2013).

[26] Clarke, J. und AI Braginski (Ed.), "The SQUID Handbook: Vol. I Fundamentals and Technology of SQUIDs and SQUID Systems." (2004).

[27] J. Clarke and A. I. Braginski. The SQUID Handbook Vol. 1 (Wiley VCH, GmbH and Co. KGaA, Weinheim, 2004).

[28] The supplementary information: P. Solinas, S. Gasparinetti, D. Golubev, F. Giazotto. Sci. Rep. **5**, 12260 (2015).

[29] Granata, Carmine, and Antonio Vettoliere. "Nano superconducting quantum interference device: A powerful tool for nanoscale investigations." Physics Reports 614 (2016): 1-69.

[30] Golubov, Alexandre Avraamovitch, M. Yu Kupriyanov, and E. Il'Ichev. "The current-phase relation in Josephson junctions." Reviews of modern physics **76**.2 (2004): 411.

[31] Hasselbach, K., D. Mailly, and J. R. Kirtley. "Micro-superconducting quantum interference device characteristics." Journal of applied physics **91**.7 (2002): 4432-4437.

[32] Granata, C., *et al.* "Noise theory of dc nano-SQUIDs based on Dayem nanobridges." Physical Review B **84**.22 (2011): 224516.

8 Conclusions

The work conducted for this thesis is part of a larger project which mainly involves several goals: (*i*) fabricating and characterising junction devices made of diamond superconducting, (*ii*) fabricating and characterising diamond SQUIDs, (*iii*) implementing a micro or nano-electro-mechanical cantilevers in the fabricated SQUID loops, which allows the investigation macroscopic quantum states, (*iv*) modelling the system and interpreting the observed effects occur in it's component in terms of the fundamental and recent theories of superconductivity, and (*v*) solving the technical problems that influence the quality of the measurements. In the course of this work, a number of issues associated with these goals have been solved.

Technically, the prototype of the RF filters developed and fabricated which can successfully attenuate RF noise to a level of -110 dB in high frequency regions, and between -60 dB and -110 dB in low frequency regions below 500 MHz. Consequently, the filters will significantly allow the attenuation of the noise associated with SQUIDs and qubits. A comparison between the filters fabricated within course of this thesis, and the filters previously fabricated, suggests that the filters, developed here, are quite competitive. Furthermore, CBT measurements have clearly shown that these filters are quite appropriate to accompany simultaneous measurements that take place in an ultra low temperature measurements system, where the temperatures down to few mK.

$I(V)$ characteristics and the differential resistance measurements have been performed for SIS junctions and nanobridges devices made of BDD. The measurements show different features, and have been discussed in terms of fundamental theories of superconductivity presented in this thesis. $I(V)$ curves of a nanobridge device (5A) with bridge dimensions of $L = 118$ nm, and $W = 109$ nm, have been measured at different temperatures, from which critical currents $I_c(T)$ have been extracted. Fitting of the extracted $I_c(T)$ shows agreement with an exponential like function where, $I_c(T) \propto \exp(-L\sqrt{T})$. Such behaviour was attributed to the proximity effect described by Likharev's theory of SNS weak-link junctions. Magnetic field of $I(V)$ curve have been also measured for device 5 at $T = 1.85$ K. As results, Fraunhofer pattern was not observed in measured $I_c(B)$ behaviour. Reasons for such discrepancy has mainly assigned to RF noise, and to the coherence length of the superconducting diamond films, which is too short relative to the length and the width of the weak link of the device.

Measurements for $I(V)$ curves performed at temperatures between 10 and 700 mK for another device (2A) with $W = 108$ nm, and $L = 78$ nm, show an interesting feature, where notable resistive steps in the transition region of the $I(V)$ curves around I_c have been observed. These steps have been attributed to: (*i*) vortex kinematics where vortices and antivortices created on the edges of the device, which propagate and overlap at the center of the bridge, where they annihilate, which finally results in phase slip lines (PSLs). And (*ii*) the granular superconducting properties of the film from which the device was made, where a further phase slip events, at which the order parameter $|\psi_{ij}|^2$ vanishes

instantaneously due to the interaction between the phases φ_{ij} of the wave functions ψ_{ij} that tunnel through grain boundaries indicated by i and j. Here, superconducting grains can be considered as arrays of Josephson junctions, which results in steps of the $I(V)$ characteristics.

Measurements for $I(V)$ characteristics of another nanobridge device (1A) with $W = 105$ nm, and $L = 128$ nm, were performed, and compared with other two devices. This comparison, where the critical currents extracted at $T = 7$ mK for the three measured devices, shows a significant disagreement with quantitative description given for critical current of a typical Josephson junction where $I_c = \frac{e^*\hbar}{2m^*}|\Psi_0|^2\frac{A}{L}$. Such discrepancy is due to several factors: the length and width of the bridges, the granularity effect, and phase slip events that may take place in such devices due to their structures.
$I(V)$ characteristics measured for a typical SIS junction with 6 nm width, was fitted using the RSCJ model, and the fit shows good agreement with model. Other measurements for $I(V)$ characteristics of an SIS junction with a 15 nm gap have been performed. The $I(V)$ characteristics show a nonlinear behaviour when, an ac current drive is applied, and show a linear behaviour for dc measurements. Such behaviour is still not understood. Results observed for a SIS junction with a 76 nm vacuum gap, where measurements for the temperature dependence of the $I(V)$ characteristics, and differential resistance have been performed between 250 mK and 4 K. The extracted critical currents, $I_c(T)$, have been discussed in terms of Ambegaokar and Baratoff formula and BCS theory, where a fit for $I_c(T)$ was performed, and shows a good a agreement with this formula. In the $I(V)$ curves measured for this junction, another transition have been observed in the superconducting region, indicated by I_{c1}. In contrast to the $I_c(T)$, the transition $I_{c1}(T)$ shows a discrepancy with the Ambegaokar and Baratoff formula. As the gap width of the this junction is quite large relative to coherent length of the superconducting diamond films, the origin of the measured $I(V)$ curves require further work for better understanding.
Measurements for $I(V)$ and $R(T)$ curves of superconducting strips of different strictures have been performed. In these measurements, resistive steps have been observed around transition regions of the $I(V)$ curves. In addition to that, corresponding spikes in the $R(T)$ curves have been observed. The observed resistive steps in the $I(V)$ curves, and corresponding spikes, have been attributed to a collective effect described by kinematic vortices, thermal fluctuations and/or quasiparticles diffusion (SBT model), and the granularity of the superconducting diamond films from which the strips have been made.
Simulations to quantitatively describe the interaction between a dc SQUID and an integrated doubly clamped cantilever were performed, by which an existing experimental configuration was selected to explore and the motion of the cantilever. The unscaled dc SQUID equations coupled to the equations of motion of an integrated cantilever, have been solved, and of voltage-displacement traces of a displacement detector were determined. Furthermore, the effect back-action between the SQUID and the doubly clamped cantilever have been analysed via the shift in the cantilever frequency, the line width, intensity, and shift in the position of the normal state. The simulations show how a sharp transition state drives the system into a nonlinear-like regime, and modulates the cantilever displacement amplitude, by tuning the bias current I_b, and the external flux Φ_{ext}, which set the system in different regions of $V(\Phi)$ curve.
Finally, further experimental and theoretical work are still required to achieve the final goal of the long term project. At first, numerical calculations of time dependent Ginzburg

Landau equation (TDGL) equation need to be solved for a case that considers the granularity of the superconducting films from which the devices are fabricated. Here, the boundary conditions to be applied between the grain boundaries, though such treatment can be computationally challenging, an approximation may be made to simplify the problem. The granularity can be analysed also in terms of array of Josephson junctions that can quantitatively describe the resistive steps observed in the measurements achieved for one of the nanobridge devices, and all superconducting strips. Second, more SIS junctions, nanobridge devices are required to be measured to provide a clearer picture about the experimental results reported in this thesis. Such work will allow the development and fabrication of sensitive superconducting diamond SQUIDs that enable to detect the motion of an integrated cantilever of high frequencies at which the SQUID-cantilever system enters the quantum state.